# Hydrological and Climate Change Assessment for Hydropower development in the Tamakoshi River Basin, Nepal

March 2017

**Authors**
W. Terink
W.W. Immerzeel
A.F. Lutz
P. Droogers
S. Khanal
S. Nepal
A.B. Shrestha

**Client**
Statkraft

**FutureWater Report 164**

**FutureWater**
Costerweg 1V
6702 AA Wageningen
The Netherlands

+31 (0)317 460050

info@futurewater.nl

www.futurewater.nl

# Executive summary

Energy is one of the major drivers of changes in the HKH region. The region has a high hydropower potential due to abundance of water in conjunction with verticality of landscape. However, the climate, cryosphere and hydrology of the Hindu Kush Himalaya (HKH) region have been changing in the past and will continue to change in the future, posing a risk to hydropower development in the future. It has become imperative for hydropower developers to have a good understanding about the changes in the hydrological cycle and its uncertainty and how the changes might affect the hydropower production in the region. Also, changing probabilities and magnitudes of extreme events can put additional risk on hydropower infrastructures. For Statkraft, being a leading company in hydropower internationally, an understanding of future changes to the hydrological cycle and its uncertainty is crucial for effective business planning. Additionally, changing probabilities and magnitudes of extreme events can put additional risk on infrastructure, and trigger natural hazards such as e.g. floods and landslides. To match the growing demand of electricity in Nepal and the region, Statkraft is interested to develop hydropower facilities in the Tamakoshi River Basin in Nepal.

Therefore, the objective of this study is to improve the understanding of the expected impacts of climate change on water availability in the context of potential hydropower development in the Tamakoshi River Basin. The approach followed in this study to achieve this objective can be summarized in:

- Selection and bias-correction of reference climate data set, representing the baseline climate (1981-2010);
- Selection and statistical downscaling of 4 RCP4.5 and 4 RCP8.5 GCMs, representing an ensemble of future climates (2016-2075);
- Calibration of a spatially distributed hydrological model to match the observed glacier mass balance and river discharge;
- Forcing the hydrological model with the baseline and future climate data to obtain time-series of daily discharge for the hydropower plant locations Khimti and Tamakoshi-III;
- Analyses of changes in precipitation, temperature, glacier melt, and river discharge between the future and baseline period;
- Using the simulated time-series of river discharge as input in the Water Evaluation And Planning (WEAP) model to assess the hydropower generation potential for the current and future climate for the plants Tamakoshi-III and Khimti. Scenario analysis, using different design criteria for reservoir storage capacity and maximum turbine flow, provided the hydropotential for the future under different design criteria.

Based on the results of this study it can be concluded that we can expect an overall increase in basin average precipitation and temperature, and a gradual decrease in glacier melt. Since the change in flow due to the increase in precipitation is larger than the decrease in glacier melt, and the contribution of glacier melt to the total river discharge in this basin is minor, an increase in river discharge is projected for the future.

For Tamakoshi-III we may expect average annual discharges varying between 125-225 $m^3/s$ in the future (currently 130 $m^3/s$ on average), which is mainly contributed by the increase in rainfall, especially during the monsoon season. The current monthly average discharge at Tamakoshi-III peaks at 400 $m^3/s$ during August, whilst this may increase towards 450-500 $m^3/s$ for 2016-2045, and 450-550 $m^3/s$ for 2046-2075. Extreme analyses showed that the maximum annual discharge with a return period of once every 10 years for the baseline climate is approx. 650 $m^3/s$ for Tamakoshi-III. With the same probability (1/10 year), this extreme discharge



increases to 1000-1100 $m^3/s$ for 2016-2045, and 1200-1300 $m^3/s$ for 2046-2075. The current maximum annual discharge with 100-year return period is approx. 700 $m^3/s$. As a result of climate change, this maximum annual discharge with 100-year return period may increase towards 1400 $m^3/s$ for 2016-2045, and to 1600 $m^3/s$ for 2046-2045.

For Khimti the average river discharge is approx. 23 $m^3/s$ for the baseline climate, and this may increase towards 30-35 $m^3/s$ in the future. This is only contributed by rainfall, since no glaciers are to be found upstream of Khimti. Monthly discharge at Khimti peaks during August with an average monthly discharge of 67 $m^3/s$ for the baseline climate. This likely increases towards 65-85 $m^3/s$ during 2016-2045, and 70-95 $m^3/s$ during 2046-2075. Extreme analyses showed that the maximum annual discharge with a return period of once every 10 years for the baseline climate is approx. 110 $m^3/s$ for Khimti. With the same probability (1/10 year), this extreme discharge increases to 150-160 $m^3/s$ for 2016-2045, and 170-190 $m^3/s$ for 2046-2075. The current maximum annual discharge with 100-year return period is approx. 130 $m^3/s$. The maximum annual discharge with 100-year return period may increase towards 190-200 $m^3/s$ for 2016-2045, and to 240-330 $m^3/s$ for 2046-2075.

As a result of the expected increase in river discharge, higher hydropower production can be expected in the future. Under current design criteria, the total energy production from both plants is expected to increase from 2700-2800 GWh/y to 2750-3050 GWh/y on average. For Tamakoshi-III only, an increase is expected from 2350-2400 GWh/y to 2370-2600 GWh/y. The increase for Khimti is from 370-400 GWh/y to 390-430 GWh/y. While the increase in discharge is a positive development for hydropower generation, the increase in total flow and extremes may have a negative impact on floods, the vulnerability of infrastructure, erosion, and the sedimentation of reservoirs. Two types of scenarios were evaluated: (i) different reservoir capacities for Tamakoshi-III, and (ii) different maximal turbine flows for Tamakoshi-III and Khimti. With an increase in reservoir capacity of 2 to 5 times, hydropower generation will increase by about 5% to 22% for Tamakoshi-III. Likewise, reducing the storage capacity by 50% would reduce hydropower projection by about 8%. For the different maximum turbine flow scenarios, it can be concluded that for Tamakoshi-III the maximum turbine flow design capacity is well-planned, as an increase will have only a minor impact on hydropower generation. However, for Khimti there seems to be a real potential to re-evaluate the maximum flow design capacity; doubling the capacity will generate about 55% more hydropower. These projected potential hydropower productions are associated with certain uncertainties. Obviously, the most important uncertainty is the projected flows in the rivers at the potential hydropower plant locations. This is handled by considering a broad range of climate projections. Another important source of uncertainty is the actual configuration of the plant itself with factors as maximum turbine flow and generating efficiencies. Finally, operations and maintenance of the actual plant once constructed are as usual an important uncertainty factor in terms of hydropower production.

# Table of contents

# Tables



# Figures





# 1 Introduction

The climate, cryosphere and hydrology of the Hindu Kush Himalaya (HKH) region have been changing in the past and will continue to change in the future [*Immerzeel et al.*, 2010; *Lutz and Immerzeel*, 2013; *Lutz et al.*, 2016a]. Warming of the climate system is unequivocal; the atmosphere and ocean have warmed, the amounts of snow and ice have diminished, sea level has risen as a result of the increase in concentrations of greenhouse gases. The Himalayan region has the third largest stores of ice and snow in the world, after Antarctica and the Arctic and might be exceptionally vulnerable due to a warming climate. There is a good agreement among Global Climate Models (GCM) on future temperature trends in the region, but projections of future precipitation patterns differ widely and detailed impact studies are largely lacking. Consequently, the demand for increased knowledge about future climate change is still high. A main focus has been given to temperature increases and changes to the hydrological cycle with the tendency that wetter regions mainly will become wetter and drier regions will become drier. Recent scientific knowledge supported by observed weather events show that extremes related to hydrological changes can be substantial though and the geographical and time-wise resolution of predicted changes is still low in many areas.

Energy is one of the major drivers of changes in the HKH region. The region has a high hydropower potential due to abundance of water in conjunction with verticality of landscape [*Shrestha et al.*, 2016]. However, the changing climate and hydrological regime might pose risk to hydropower development in the future. It has become imperative for hydropower developers to have a good understanding about the changes in the hydrological cycle and its uncertainty and how the changes might affect the hydropower production in the region. Also, changing probabilities and magnitudes of extreme events can put additional risk on hydropower infrastructures.

**Figure 1: The Tamakoshi river (source: http://www.nepalenergyforum.com).**

For Statkraft[1], as the largest generator of renewable energy in Europe, and a leading company in hydropower internationally, an understanding of future changes to the hydrological cycle and its uncertainty is crucial for effective business planning. Investment decisions regarding the business strategy for the next 50 years depend on reliable predictions of climate change impacts on streamflow and thereby hydropower development over that period. In addition, changing probabilities and magnitudes of extreme events can put additional risk on infrastructure (dams and hydropower plants) or on other crucial infrastructure (roads and transmission lines). Statkraft's intention to develop hydropower in the region makes it necessary

[1] http://www.statkraft.com/

to assess short, medium and long-term impacts, risks and opportunities resulting from climate change, to ensure sustainable development of renewable energy in general and hydropower development for all stakeholders. To match the growing demand of electricity in Nepal [*NEA*, 2015] and the region, Statkraft is interested to develop hydropower facilities in the Tamakoshi River Basin in Nepal. For this reason, Statkraft is interested in the impact of climate change on the potential of hydropower development in the Tamakoshi River Basin, particularly focusing on changes in seasonal variations and extreme events.

The overall objective of this study is therefore to improve the understanding of the expected impacts of climate change on water availability in the context of potential hydropower development in the Tamakoshi River Basin. Specifically, this study aims to:

- Understand current baseline hydrological regime of the Tamakoshi River Basin;
- Develop detailed projections for the 21st century, including factors relevant for hydropower development;
- Understand the future hydrology and its potential impact on hydropower potential;
- Evaluate the potential for hydropower under a changing climate using different dam and reservoir design criteria.

For this study it was decided to evaluate the impact of climate change on the hydropower development for the Tamakoshi-III and Khimti hydropower plants only. The methodology, as applied in this study, can therefore be repeated to evaluate the hydropower potential for other hydropower plants in this basin, or region.

The methodology applied in this study to evaluate the hydropower potential under a changing climate is subsequently described in this report. Chapter 2 provides an overview of the topography and orography of the Tamakoshi River Basin, whereas ongoing hydropower initiatives are described in Chapter 3. Trends in snow cover for the current climate are described in Chapter 4. The methodology followed in this study are described in Chapter 5. The selection of a baseline reference climate dataset, and bias-correction thereof is described in Chapter 6. The hydropower potential for the future climate is compared with respect to this baseline climate. The next chapter provides the reader with some background information on General Circulation Models (GCMs), Representative Concentration Pathways (RCPs), the selection of eight GCMs to be used as ensemble to assess the future climate, and the statistical downscaling thereof. Chapter 8 introduces the Spatial Processes in HYdrology (SPHY) model [*Terink et al.*, 2015], explains the improved glacier module, and describes the model calibration for the glaciers' mass balance and river discharge. In Chapter 9 the impact of climate change is described, with a specific focus on changes in precipitation and temperature patterns, glacier melt, and the impact of those changes on the river discharge. The impact on the river discharge is analyzed annually and monthly for the entire river basin, as well as for Tamakoshi-III and Khimiti separately. Changes in extreme river discharge are assessed as well. The impacts of climate change on the potential for hydropower for Tamakoshi-III and Khimti are described in Chapter 10. The hydropower potential has been evaluated for the baseline climate, and for the future climate using different dam and reservoir design criteria. Conclusions and recommendations are described in Chapter 11.



# 2 Tamakoshi River Basin overview

The Tamakoshi River Basin (2,926 km$^2$) is located on the southern slopes of the Hindu Kush Himalayan region (Figure 2). The elevation in this basin ranges from more than 800 MASL in the southern valleys to approx. 7,000 MASL northern part. Geographically this basin is situated between 27°37'42''N to 28°19'23''N latitudes and 86°0'9''E to 86°34'12''E longitudes.

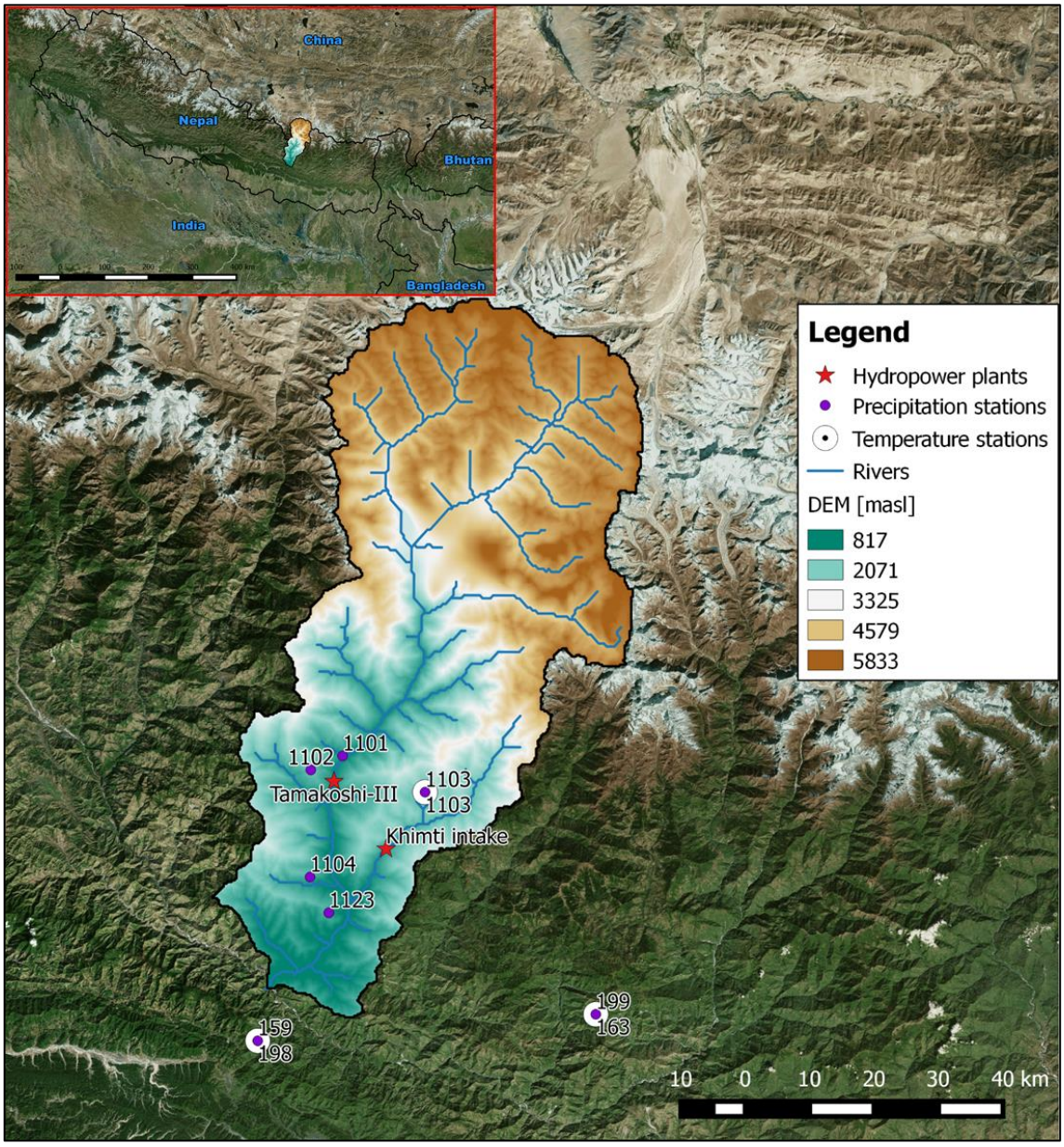


**Figure 2: Tamakoshi River Basin with location of Statkraft hydropower plants, precipitation- and temperature stations.**

Tamakoshi River Basin is a tributary of the Koshi River Basin, which is the most eastern catchment of the Ganges River Basin. The basin originates from the high-altitude areas of China and Nepal. Approximately 51% (1,498 km$^2$) of this basin is located in China, and the remaining part in Nepal Himalaya. On average 20% of the area is covered with snow [*Khadka et al.*, 2014]. According to *Pfeffer et al.*, [2014], 276 individual glaciers are present in the

Tamakoshi River Basin, totaling an area of 329 km$^2$. This corresponds with approx. 11% of the total basin area. The largest glacier is located in the north of the basin, and has a total surface area of 42 km$^2$ [*Pfeffer et al.*, 2014]. The Tamakoshi River Basin is a tributary of the Koshi River Basin, which merges into the Ganges [*Khadka et al.*, 2014]. According to *Bajracharya et al.* [2014], the glacierized area in the Nepalese part of the Tamakoshi River Basin was 120 km$^2$ in 1980, which decreased to 102 km$^2$ in 1990 (-15%), 94 km$^2$ in 2000 (-22%) and 84 km$^2$ in 2010 (-30%). At the same time, the number of glaciers has increased by nearly 10%. This change in glacier dynamics might affect hydrological regime of the Tamakoshi River Basin.

Climatologically the basin is heavily influenced by the summer monsoon, which runs from June through September. The average basin temperature is 28 °C in summer compared to 7°C during winter [*Khadka et al.*, 2014]. Annually the basin average precipitation equals 1900 mm with 80% falling during the monsoon season. The wettest months are July and August, with average annual precipitation sums of 500 and 460 mm, respectively [*Khadka et al.*, 2014].

Figure 2 provides an overview of the Tamakoshi River Basin, including its elevation range, the location of precipitation and temperature stations, and Statkraft Hydropower Plant locations for which the potential has to be evaluated.

# 3 Ongoing Hydropower Initiatives

## 3.1 Hydropower potential and outlook

Because of the steep topography and strong dominance of monsoon, the Tamakoshi River Basin has a high potential for hydropower development. A number of studies have attempted to estimate the total hydropower potential of the Tamakoshi River Basin using a combination of GIS analyses and models based on hydrological observation data. *Jha* [2011] estimated the total hydropower potential of the Tamakoshi River Basin to be 2,088 MW at 40% flow exceedance and 80% efficiency (17,000 MW for whole Koshi River basin). The total installed capacity of hydropower in Nepal is only 887 MW through 59 hydropower projects as of 1 February 2017 [*DOED*, 2016], which have installed capacities ranging from 1 to 144 MW. Out of this, 9% (75.52 MW) is contributed by the Tamakoshi River Basin alone.

The energy demand in Nepal as a whole for 2014-2015 during peak hours was 1,286 MW [*NEA*, 2015]. Electricity demands have increased with approx. 7% each year in Nepal [*NEA*, 2015], mainly for rural electrification, industries and domestic use. The domestic consumer has the largest demand, with a 9% increase (in the range of 3 to 13%) between 2006 and 2015. According to the Nepal Electricity Authority (NEA), the forecasted demand for 2033 is around 5,785 MW (Figure 3) [*NEA*, 2015].

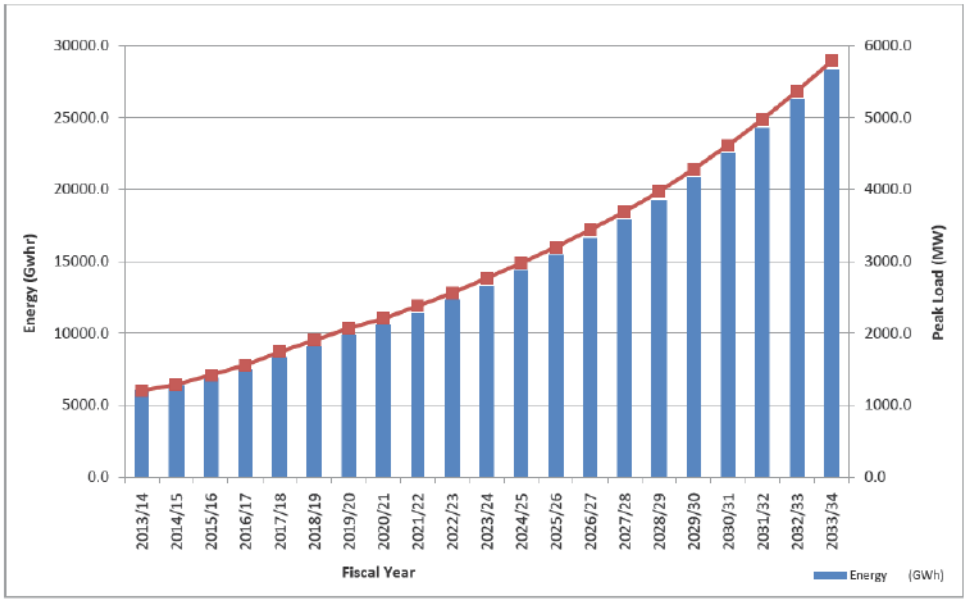


**Figure 3: Load forecast of electricity demand until 2033/34 [NEA, 2015].**

## 3.2 Hydropower development

The Department of Electricity Development (DOED), the Ministry of Energy is the nodal agency to develop and promote electricity sector in Nepal. As shown in Figure 4, the following key steps are involved in the electricity generation in Nepal. First, a survey license is applied to DOED by hydropower developers. Once the survey license of a hydropower project is issued, the developers prepare a feasibility report after the completion of the survey and submit to DOED. Then, the developers submit an application for the generation license within the validity of the license. After the evaluation of the applications, the generation license is issued for construction

and the developers then can start the construction of the projects. While under construction, a transmission license can be applied to DOED; whereas distribution license is applied and issued only after the completion of the project and testing of the generation is carried out.

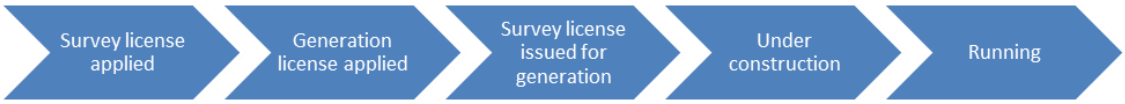


**Figure 4: Flow chart of Hydropower development process in Nepal [DOED, 2016].**

According to *WECS* [2011], the Government of Nepal considers three strategic levels hydropower development:

1. Large scale storage projects primarily intended for exporting energy (>100 MW[1]);
2. Medium-scale projects to meet national energy demands (1-100 MW);
3. Small-scale projects catering to the local communities (<1 MW).

From the first category, the potential energy production was estimated to be around 22,200 MW, through four storage projects; Chisapani-Karnali (10,800 MW), the Pancheswor (6480 MW), the Budhi Gandaki (600 MW) and the Sapta Koshi High Dam (3600 MW). The Tamakoshi River Basin has the potential to fulfil the requirement of all three levels. Currently, four hydropower projects are running which are producing 76 MW of electricity to the national grid (Table 1 and Figure 5). Similarly, 9 hydropower projects with a total capacity of 595 MW are under construction. These projects range from 5 MW (Ghatte Khola Hydropower) to 456 MW (Upper Tama Koshi). The latter - which is scheduled to be completed by 2018 - would be the largest hydropower (also under construction) in Nepal so far. This will be a run-of-the-river type of hydropower plant with a design discharge of 66 $m^3/s$, and a maximum gross head of 822 m [*Shrestha et al.*, 2016]. Additionally, there are 15 hydropower projections with a total installed capacity of 1,156 MW which are in different stages of license application (Table 1). Altogether, these 29 hydropower projects are able to produce 1,826 MW of hydropower to the national grid from the Tamakoshi River Basin.

[1] Category ranges according to the Water Resources Policy (in draft)

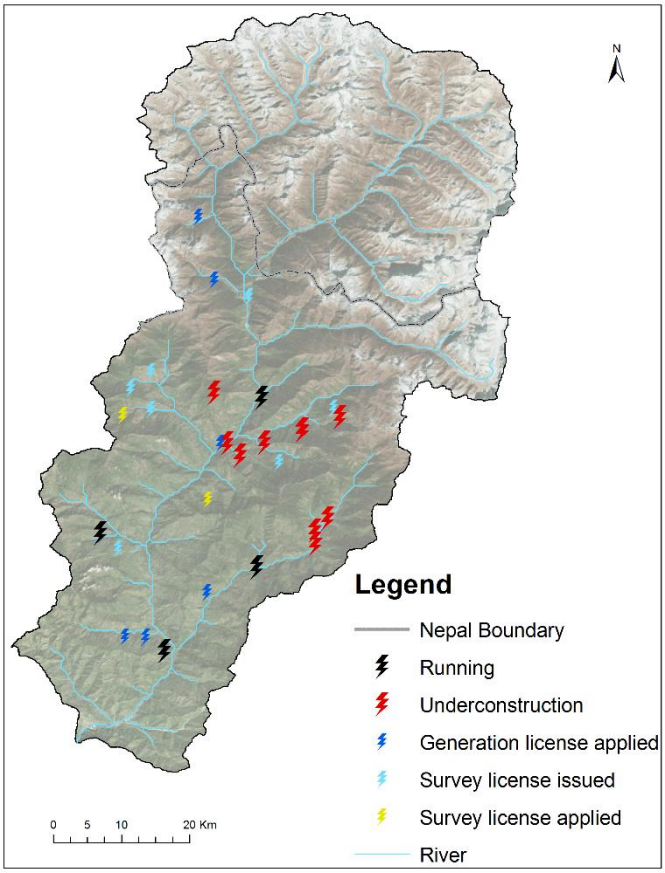


**Figure 5: Hydropower initiatives in the Tamakoshi River Basin [DOED, 2016].**

**Table 1: Status of different stages of hydropower in the Tamakoshi River Basin [DOED, 2016].**

| Project | Type | Capacity (MW) | Status | Gross Head (m) | Design flow (m3/s) | Catchment area (Km2) |
|---|---|---|---|---|---|---|
| Sipring Khola | Run-of-the-river | 9.6 | Running | 443.7 | 2.61 | |
| Charnawati Khola | Run-of-the-river | 3.52 | Running | 199 | 2.19 | |
| Jiri Khola | Run-of-the-river | 2.4 | Running | | | |
| Khimti 1 | Run-of-the-river | 60 | Running | 660 | 10.75 | 358 |
| Upper Tamakoshi | Peaking Run-of-the-river | 456 | Under construction | 822 | 66 | 1745 |
| Khani Khola 1 | Run-of-the-river | 40 | Under construction | 963 | 5.1 | 76 |
| Lower Khare | Run-of-the-river | 11 | Under construction | 136.7 | 10.1 | 180 |
| Khani Khola(Dolakha) | Run-of-the-river | 30 | Under construction | | | |
| Khare Hydropower Project | Run-of-the-river | 24.1 | Under construction | 343.85 | 8.43 | |

| | | | | | | |
|---|---|---|---|---|---|---|
| Suri Khola | Run-of-the-river | 7 | Generation license issued, yet to start construction | 282 | 2.75 | 36.4 |
| Ghatte Khola | Run-of-the-river | 5 | Under construction | 329.76 | 1.78 | 30 |
| Upper Khimti | Run-of-the-river | 12 | Under construction | 300.23 | 5.16 | 73 |
| Upper Khimti 2 | Run-of-the-river | 7 | Under construction | 145 | 6.45 | 73 |
| Chake Khola | Run-of-the-river | 2.83 | Under construction | 558.89 | 0.633 | 12.5 |
| Jum Khola | Run-of-the-river | 62 | Survey license issued | | | |
| Upper sagu | Run-of-the-river | 4.74 | Survey license issued | | | |
| Pegu Khola | Run-of-the-river | 4.35 | Survey license issued | | | |
| Sagu Khola | Run-of-the-river | 5 | Survey license issued | | | |
| Lower Khani Khola | Run-of-the-river | 9 | Survey license issued | | | |
| Upper Suri Khola | Run-of-the-river | 7 | Survey license issued | | | |
| Lower Charnawati | Run-of-the-river | 6.4 | Survey license issued | 203 | 4 | |
| Upper lapche | Peaking Run-of-the-river | 99 | Generation license applied | | | |
| lapche khola | Peaking Run-of-the-river | 160 | Generation license applied | | | |
| Khimti II | Run-of-the-river | 48.8 | Generation license applied | 355 | 16.11 | 317.94 |
| Tamakoshi-3 TA-3 | Storage | 650 | Generation license applied | 333 | 220 | 2927 |
| Sano milti khola | Run-of-the-river | 3 | Generation license applied | | | |
| Tamakoshi-V | Run-of-the-river | 87 | Generation license applied | 160.93 | 66 | 2153 |
| Jhyakhu khola | Run-of-the-river | 5 | Survey license applied | | | |
| Sangu khola | Run-of-the-river | 5 | Survey license applied | | | |



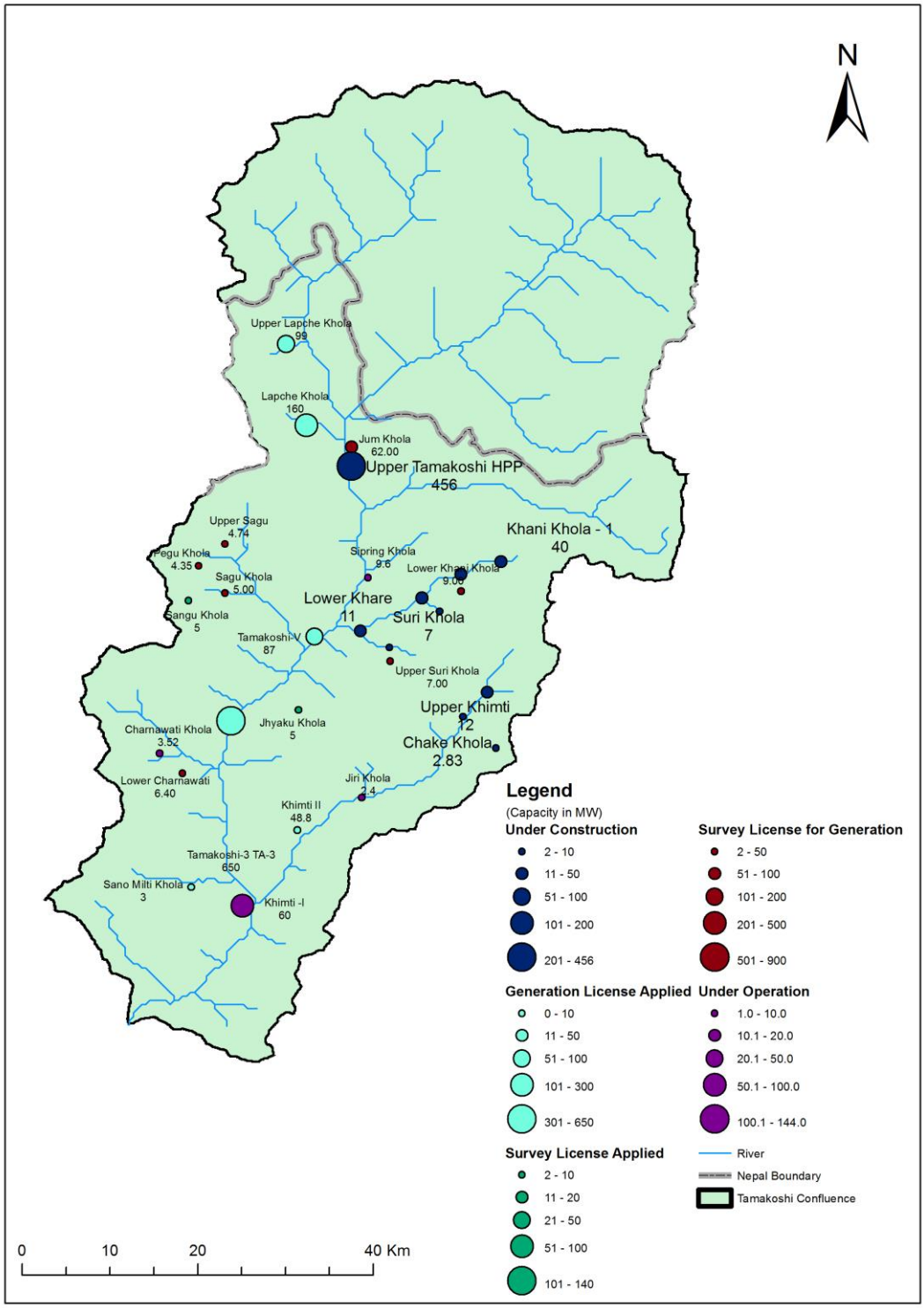


**Figure 6: Locations of potential hydropower projects with respect to their capacity.**

# 4 Snow cover trends

The Moderate Resolution Imaging Spectroradiometer (MODIS) sensor with a spatial resolution of 500 m was used for snow cover analysis. The 8-day composites of maximum snow cover from Terra (MOD10A2) and Aqua (MYD10A2) were used to derive them from daily snow cover products. The MODIS snow cover product for the Hindu Kush Himalayan region contains errors arising from cloud pixels. To remove these errors, the Terra and Aqua images were combined and temporal and spatial filters were applied, which has been explained in *Gurung et al.* [2011].

MODIS snow cover data from 2002-2014 were used to analyze the snow cover trend in the Tamakoshi River Basin. Figure 7 (top) shows the average monthly snow cover variability in the Tamakoshi River Basin from 2002-2014. Maximum snow cover is reached in February during the winter season because of winter precipitation and low temperature. Similarly, minimum snow cover is during the summer season when the temperature is high. The data indicates higher snow cover variability during spring, autumn and winter season than summer. Normally, temperatures start increasing from March and snow cover decrease due to accelerated melt associated with high temp. Figure 7 (bottom) shows the annual variability in different elevation zones which suggested maximum snow cover in between 5000-6000 MASL, followed by 4000-5000 m.

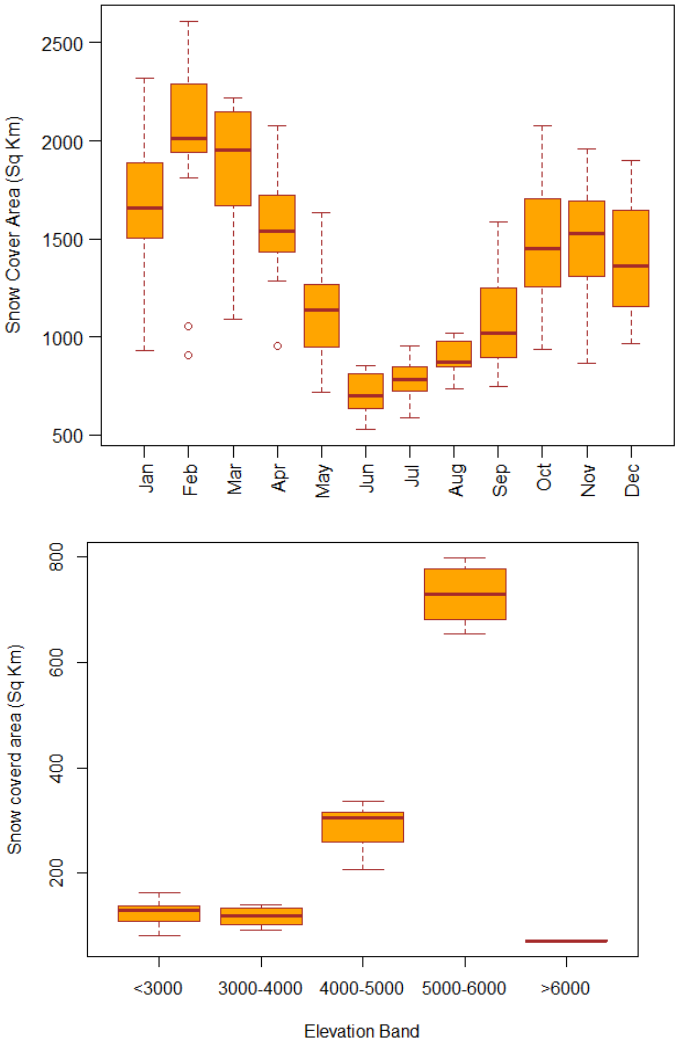


**Figure 7: Snow cover variability in the Tamakoshi River Basin from 2002-2014. Top: monthly variability. Right: annual variability in different elevation zones.**

Figure 8 shows the annual variability in different elevation zones. Most of the variation in annual snow cover is found below 6000 meter. All elevation zones show decreasing snow cover trends, except below 3000 meter (0.015 $km^2$/month), but the trend seems very low in magnitude in both directions. The maximum negative trend was observed between 4000-5000 MASL., with a value of -0.21 $km^2$/month, followed by -0.12 $km^2$/month for elevations ranging between 3000-4000 m.

*Khadka et al.* [2014] estimated a negative trend in snow cover during spring and winter, while a small positive trend is seen during autumn for the observed period (2000-2009). Similarly as suggested by *Maskey et al.* [2011], in Nepal, a negative trend in winter snow cover between 3000-5000 MASL and positive trend in autumn snow cover above 4000 MASL has been observed. The most evident trend in snow cover is visible during summer season, with snow cover decreasing for all elevation bands (Figure 10).

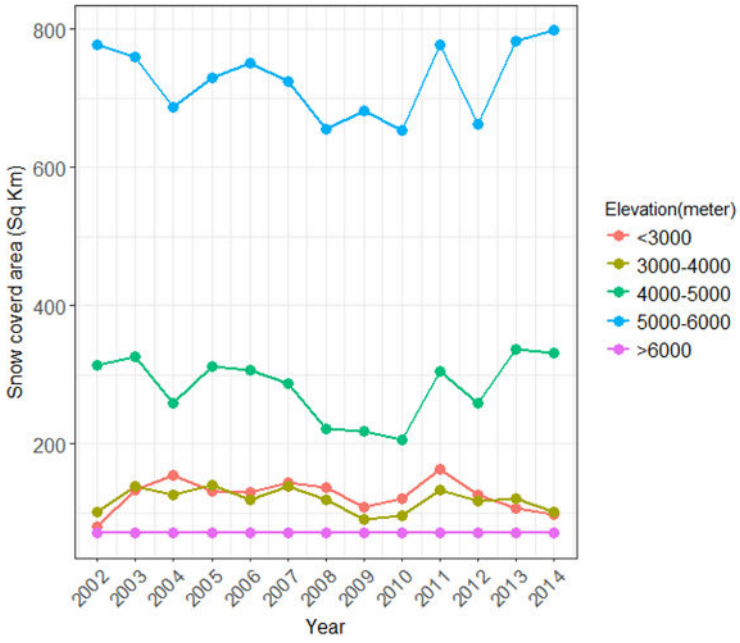


**Figure 8: Annual snow cover variability in different elevation zone.**

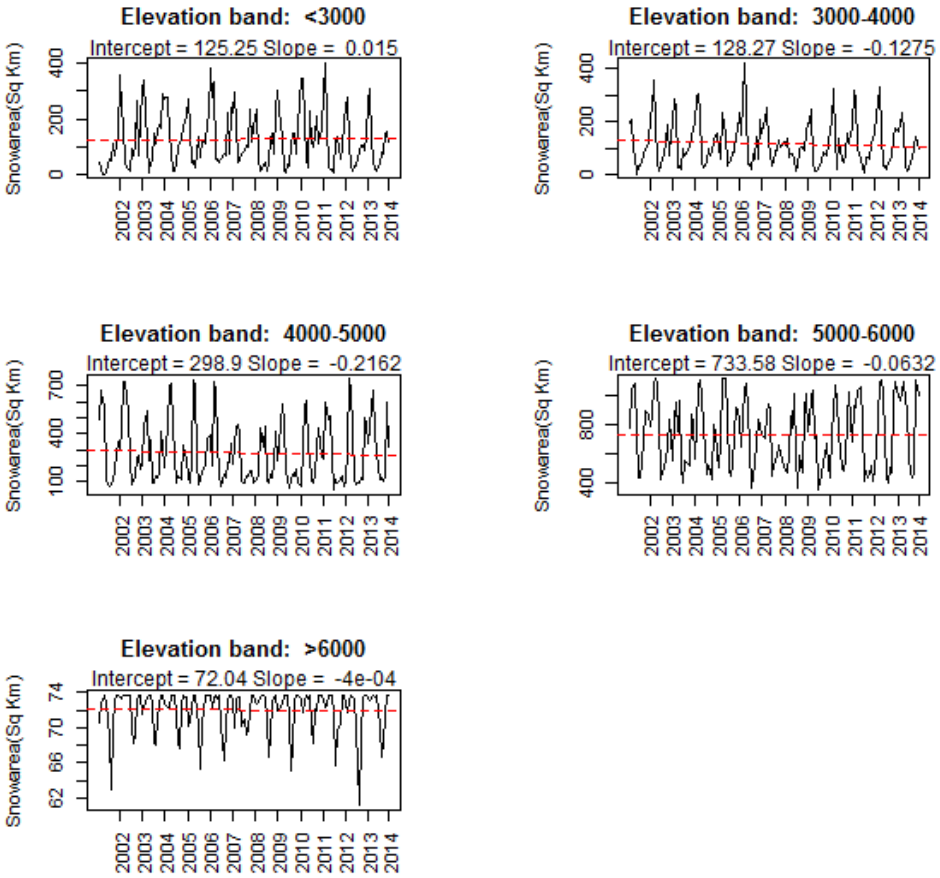


**Figure 9: snow cover trend analysis on a monthly basis for different elevation bands.**

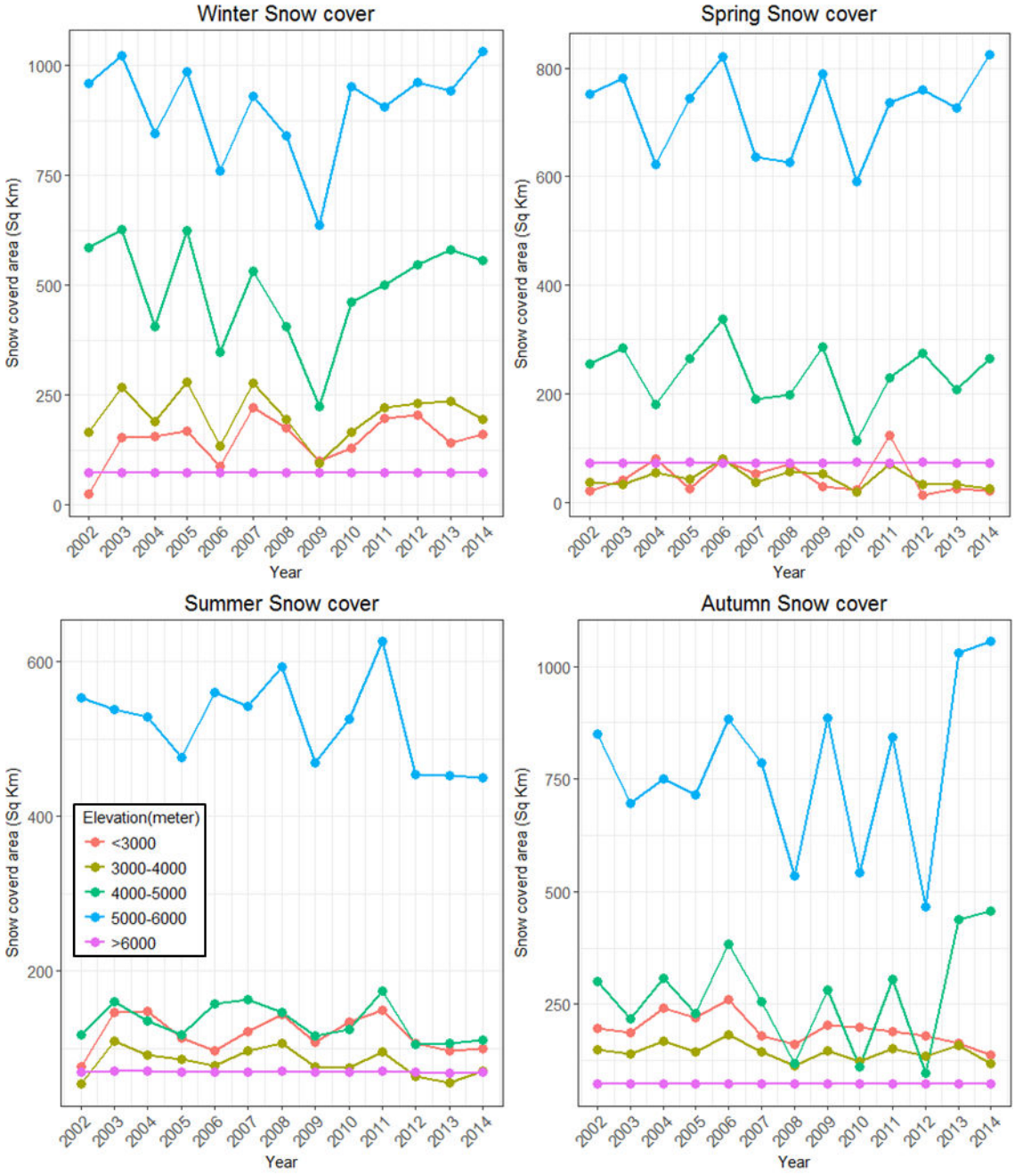


**Figure 10: Annual seasonal snow cover trends for different elevation bands.**

# 5 Methodology

The previous Chapters provided background information on the topography and orography of the Tamakoshi River Basin, ongoing hydropower initiatives, and a trend analyses on snow cover within this river basin. The overall objective of this study is to improve the understanding of the expected impacts of climate change on water availability in the context of potential hydropower development in the Tamakoshi River Basin. To achieve this objective, we need to:

1. Understand the current baseline hydrological regime of the Tamakoshi River Basin;
2. Develop detailed projections for the 21st century, including factors relevant for hydropower development;
3. Understand the future hydrology and its potential impact on hydropower potential;
4. Evaluate the potential for hydropower under a changing climate using different dam and reservoir design criteria.

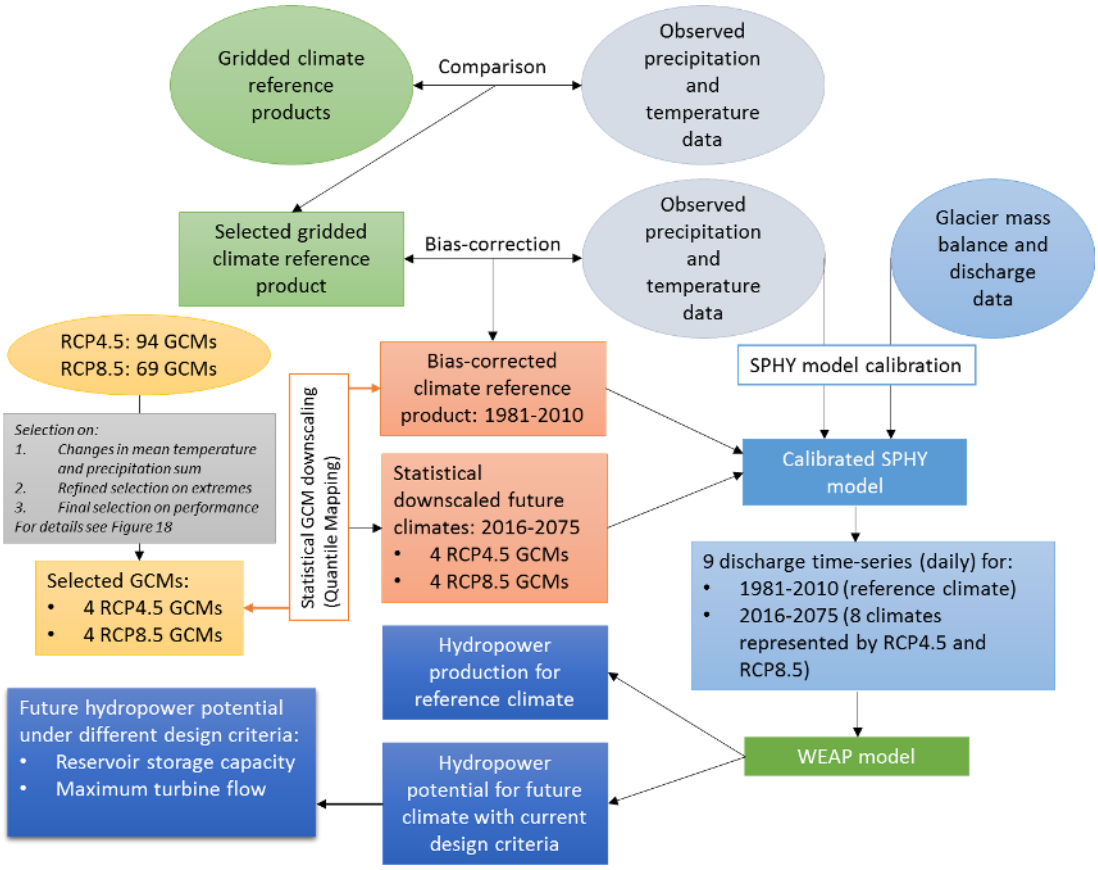


**Figure 11: Schematic overview of methodology followed in this study.**

These four steps are schematized in more detail in Figure 11. The first step is to understand the baseline (reference) climate, for which we should select an appropriate gridded climate reference product. This selection (Section 6.1) is based on a comparison between three gridded products and observed station data for precipitation and temperature. The remaining bias in temperature and precipitation between the selected gridded climate reference product and observed data was bias-corrected according to *Terink et al.* [2010] (Section 6.2). This bias-correction resulted in a bias-corrected climate reference product for the period 1981-2010, which serves as the baseline climate.



For step 2 and 3 we need to select a range of possible future climates that capture the most relevant climate indices (means, extremes, performance) for hydropower development. This procedure follows the envelope approach [*Lutz et al.*, 2016b; *Wilcke and Bärring*, 2016] and is described in detail in Section 7.2. The results of this step are 8 selected General Circulation Models (GCMs), of which 4 are represented by RCP4.5 and 4 by RCP8.5. These GCMs provide precipitation and temperature data for the period 1981-2075 on a coarse model grid resolution (~100 $km^2$ to ~250 $km^2$). This is too coarse for hydrological applications, and therefore these GCMs were statistically downscaled to the SPHY model resolution (250 m). Statistical downscaling was done using Quantile Mapping [*Immerzeel et al.*, 2013], and comparing the statistics of the bias-corrected reference climate product (1981-2010) with those of the 8 GCMs for the period 1981-2010. This step is described in more detail in Section 7.3. The 8 resulting downscaled GCMs represent the range of detailed climate projections for the 21$^{st}$ century (2016-2075), and are compared with the bias-corrected climate reference product to assess the change in precipitation and temperature.

To understand the baseline hydrological regime (step 1) we have calibrated the Spatial Processes in HYdrology (SPHY) model [*Terink et al.*, 2015] to match the observed glacier mass balance and discharge for the period 2001-2009 (see Section 8.4). The calibrated SPHY model was subsequently forced with the bias-corrected reference climate product to construct a 30-year time-series of daily discharge for the period 1981-2010 for the locations Tamakoshi-III and Khimti intake. For the future hydrological regimes (step 3), the calibrated SPHY model was forced with the 8 statistically downscaled GCMs, resulting in 8 time-series of daily discharge for the period 2016-2075 for the locations Tamakoshi-III and Khimti intake. For the hydrological impact assessment (Section 9), the future period was split into two periods of 30 years; 2016-2045, and 2046-2075.

To evaluate the potential for hydropower under a changing climate (step 4), the resulting time-series of daily discharge for the reference climate and 8 future climates were used as input in the Water Evaluation And Planning (WEAP) model [*Sieber and Yates*, 2015]. Using current reservoir and turbine flow design criteria, the hydropower generation potential for the baseline and future climate was assessed for the plants Tamakoshi-III and Khimti. The potential for hydropower generation for the future was further analyzed by using different design criteria of reservoir storage capacity for Tamakoshi-III, and maximum turbine flow for both Tamakoshi-III and Khimti. This step is described in more detail in Section 10.

# 6 Reference climate products

For the downscaling of General Circulation Model (GCM) data, a high-resolution historical climate dataset is required to establish correction functions that can be applied to the GCM future data. These correction functions are required for mainly two reasons:

1. GCMs generally have coarse spatial resolutions (~100 km or more), and therefore climate forcing of these GCMs cannot be used directly as input to spatially distributed hydrological models, which require more detailed spatial resolutions (e.g. 250 m in the current study);
2. GCMs contain biases if compared with gridded observation products for a reference climate ([*van Beek and Bierkens*, 2008; *Terink et al.*, 2010; *Khadka et al.*, 2014]). In other words, the statistics represented by the GCM often do not match the statistics represented by the gridded reference climate product. Since the gridded reference climate product is based on observational data, it is required to statistically downscale the GCM forcing's to match the statistics with those of the gridded reference climate product.

Before the selected GCMs (Section 7.2) can be downscaled, a reference climate product needs to be selected. In this chapter, three different gridded reference products (Table 2) are compared, and their quality is assessed by comparison with station data of precipitation and mean air temperature. The Watch Forcing ERA-Interim (WFDEI) dataset has been used for the HI-AWARE project [*Lutz and Immerzeel*, 2015], for which air temperature field were bias-corrected using station data from the upstream basins, and precipitation fields have been corrected for the common underestimate of high-altitude precipitation, by using glacier mass balance data as a proxy to reconstruct precipitation amounts, as described by *Immerzeel et al.* [2015a]. This dataset has been referred to as HI-AWARE in the remainder of this study.

**Table 2: Gridded climate products for comparison with station data.**

| Product | Spatial resolution | Period covered | Reference |
|---|---|---|---|
| **High Asia Reanalysis (HAR)** | 10x10 km | Oct 2000- Sept 2010 | [*Maussion et al.*, 2014] |
| **Corrected WFDEI (HI-AWARE)** | 5x5 km | 1981-2010 | [*Lutz and Immerzeel*, 2015] |
| **ERA-Interim (ERA)** | 75 x 75 km | 1979-2015 | [*Dee et al.*, 2011] |

The product with the best correspondence with station data is eventually selected to serve as i) baseline climate (1981-2010), and ii) dataset to downscale the GCMs (Section 7.3).

## 6.1 Selection of reference climate product

### *6.1.1 Precipitation*

6 precipitation stations are available in the river basin (Figure 2), which are managed by the Department of Hydrology and Meteorology (DHM[1]), Nepal. For comparison with the gridded climate products, a homogeneous and complete time-series of precipitation records was extracted for the period 2000-2009. For each of the three gridded climate products, a time-series of precipitation was extracted for the grid-cells that match the locations of the

[1] http://dhm.gov.np/



precipitation stations. These time-series were aggregated to monthly averages for the period 2000-2009, and are shown in Figure 12.

Based on the comparison shown in Figure 12 we conclude that the HI-AWARE precipitation dataset is the best candidate to be used for precipitation in the remainder of this study. The High Asia Reanalysis dataset [*Maussion et al.*, 2014] shows substantial differences with respect to the observed precipitation data, especially during the most relevant season (monsoon) and for station ID 1103. ERA and HI-AWARE are generally in line with each other, but overall HI-AWARE precipitation shows better alignment with the observed precipitation data, especially for the station IDs 1123, 159, and 163.

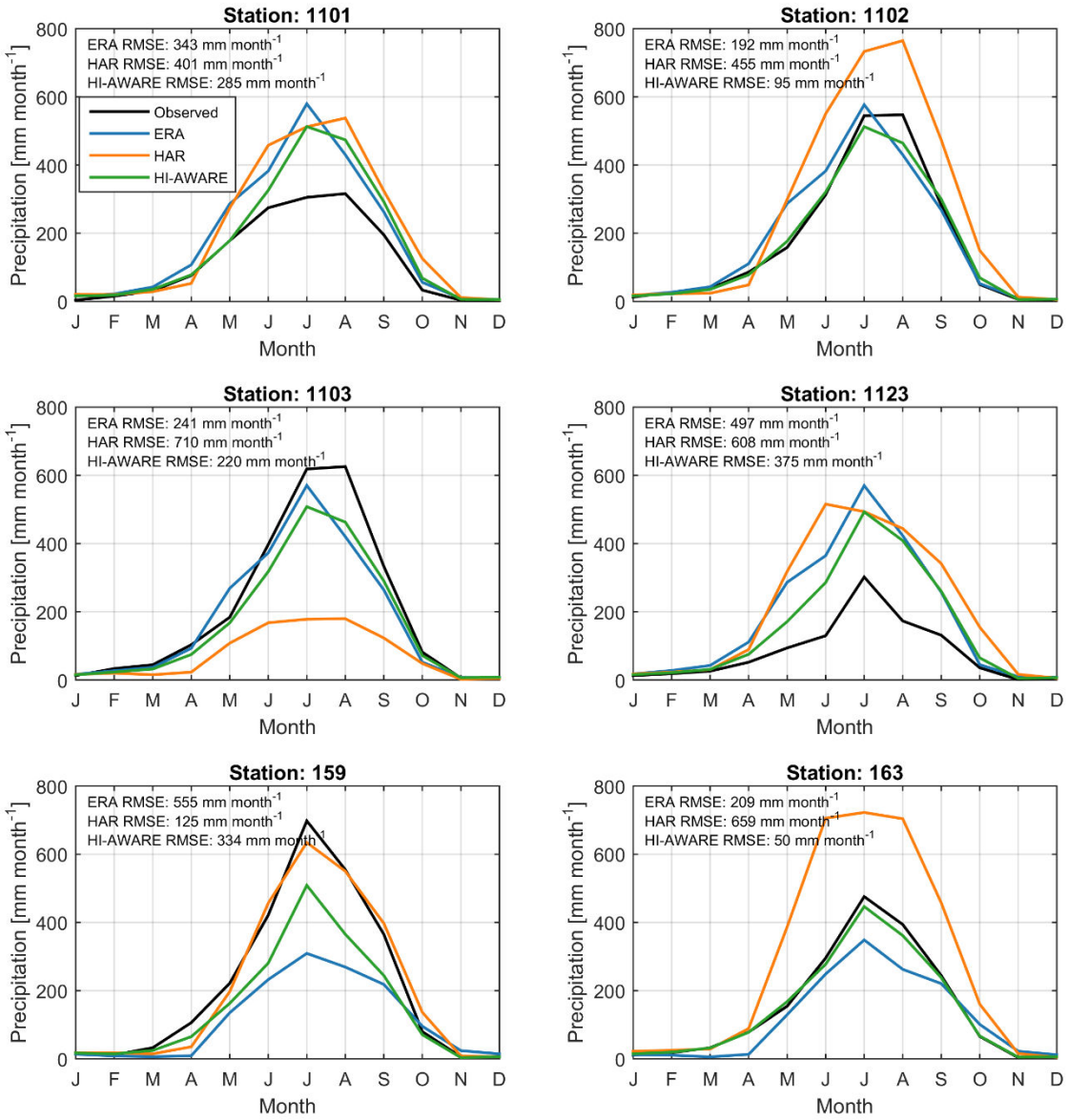


**Figure 12: Comparison of gridded precipitation of reference climate products with observed precipitation records for 6 stations in the Tamakoshi River Basin. Results are averaged to monthly precipitation sums for the period 2000-2009.**

Although HI-AWARE is selected as the best candidate for the remainder of this study, there are still substantial differences between the monthly precipitation sums of HI-AWARE and those of

the observed precipitation. Therefore, it was decided to apply an additional bias-correction to the HI-AWARE precipitation data. This is described in detail in Section 6.2.

### *6.1.2 Temperature*

Temperature data is available for three locations (Figure 2). It is clear that these stations are located in the lower elevation areas of the Tamakoshi River Basin. Since high-elevation temperature stations are not available, temperature estimations for those higher elevation areas may be less accurate. Similar as for precipitation, temperature time-series were extracted for the period 2000-2009 for the three gridded reference climate products and grid-cells that match the locations of the temperature stations. Temperature data for each of these gridded climate products were subsequently aggregated to monthly averages for the period 2000-2009, and are shown in Figure 13 along with the observed temperature data.

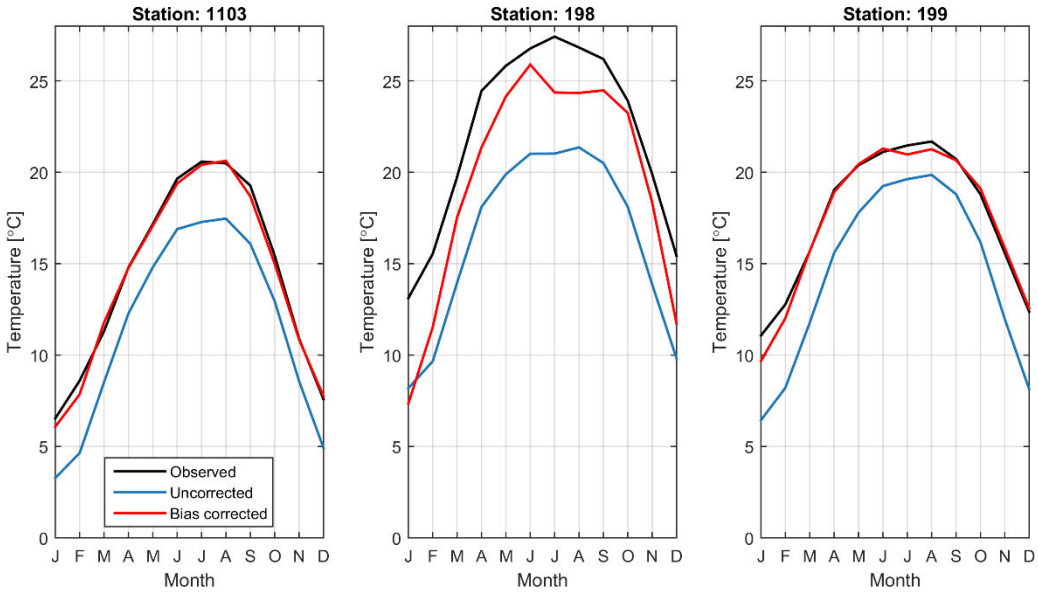


**Figure 13: Comparison of gridded temperature of reference climate products with observed temperature records for 3 stations in the Tamakoshi River Basin. Results are averaged to monthly temperature values for the period 2000-2009. Bias-corrected HI-AWARE temperature is shown as well (Section 6.2).**

Except for station ID 1103, HI-AWARE shows the best comparison with the observed temperature data. Since precipitation and temperature are generally correlated [*Terink et al.*, 2010] (when it rains it is generally colder and vice versa), it is preferred to select the same gridded reference climate dataset for temperature as for precipitation. Since HI-AWARE was selected for precipitation, and it also shows the best comparison results for temperature, the HI-AWARE reference climate dataset was selected for temperature as well.

From Figure 13 it is clear that there is a substantial offset between the gridded HI-AWARE temperature and the observed temperature data. For all stations the HI-AWARE temperature underestimates the observed temperature, which will lead to substantial errors in the calculation of glacier- and snow melt if not corrected for. Therefore, temperature has also been corrected for a bias, which is described in detail in 6.2. The red line in Figure 13 already shows the bias-corrected HI-AWARE temperature, which compares very well with the observed temperature.



## 6.2 Bias-correction of precipitation and temperature

Based on the comparison with observed records for precipitation and temperature (Section 6.1) it was decided to use HI-AWARE as gridded reference climate product in the remainder of this study. It was also concluded that an additional bias-correction is needed for both precipitation and temperature to correct for the offsets that are present, especially during the monsoon season. Bias-corrections were performed according to *Terink et al.* [2010] and *Leander and Buishand* [2007], and is explained in detail in the two sections below.

### *6.2.1 Precipitation*

*Terink et al.* [2010] determined precipitation correction factors for each block of 5 days in the year, resulting in 73 correction factors for parameter *a* and *b*. They corrected precipitation to match the Coefficient of Variation (CV) and mean with those of the observations according to:

$$P^* = a\,P^b$$

with *P** the corrected precipitation, *P* the uncorrected precipitation, *b* the correction parameter for the CV, and *a* the correction parameter for the mean. Unfortunately, only 6 precipitation stations are available, and they are located in the lower elevation areas. Precipitation dynamics in the higher elevation zones can be rather complex, and because i) the *b* parameter is very sensitive to these dynamics, and ii) no stations are located in these areas, we decided to correct for the mean precipitation only; thus we focused on the determination of parameter *a*. This parameter was determined for the 73 5-day blocks for each of the 6 locations, and were subsequently interpolated to the model domain grid cells using nearest-neighbor interpolation.

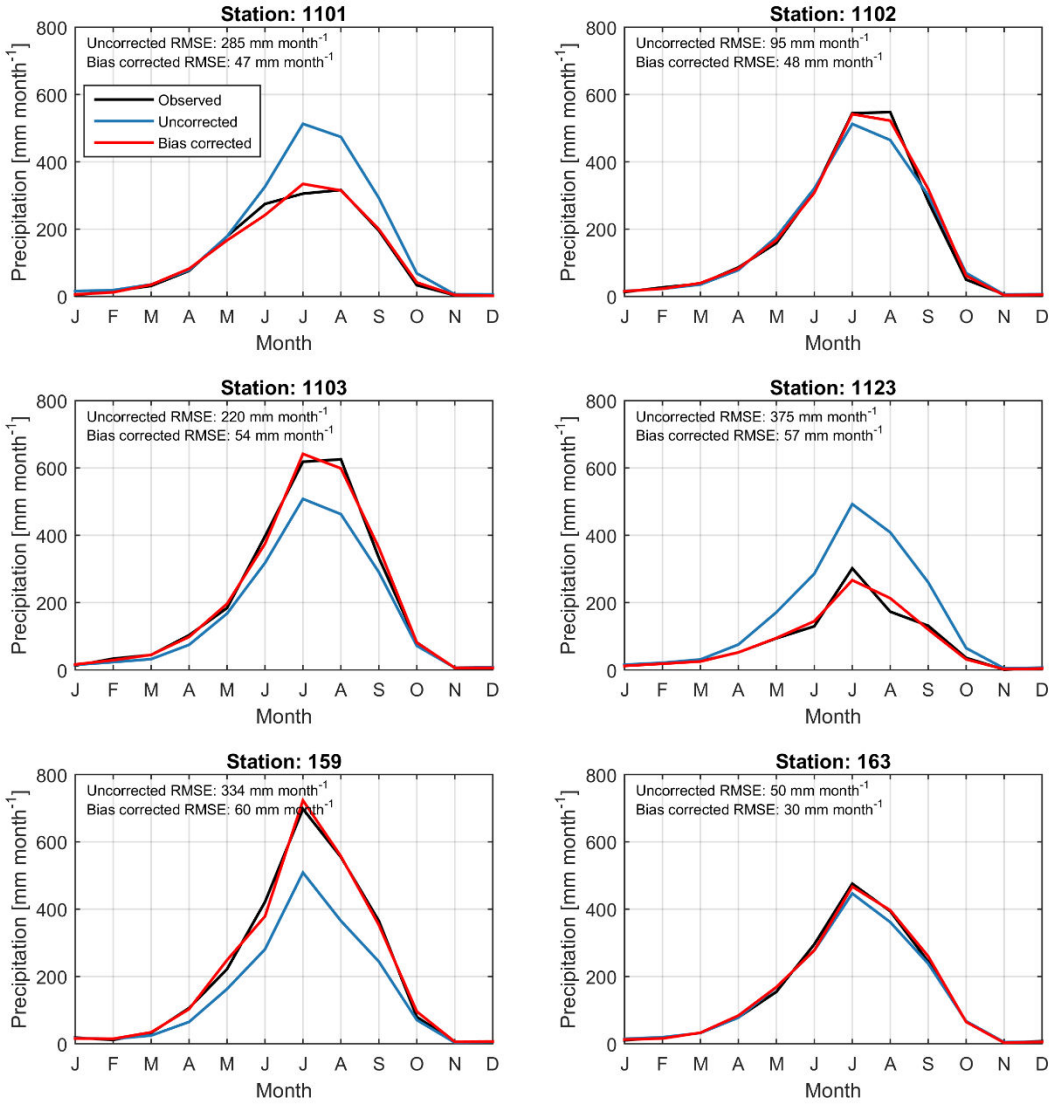


**Figure 14: Comparison of observed, uncorrected, and corrected monthly average precipitation for the period 2000-2009.**

Details regarding this bias-correction method can be found in *Terink et al.* [2010], and we only focus on the results here. Figure 14 shows the monthly average observed, uncorrected HI-AWARE, and corrected HI-AWARE precipitation. It is clear that the bias-corrected HI-AWARE precipitation data shows a substantial improvement with respect to the uncorrected HI-AWARE precipitation, especially during the monsoon season.

### *6.2.2 Temperature*

*Terink et al.* [2010] corrected temperature for the mean and variance according to:

$$T^* = \overline{T}_{obs} + \frac{\sigma(T_{obs})}{\sigma(T_{unc})}(T_{unc} - \overline{T}_{obs}) + (\overline{T}_{obs} - \overline{T}_{unc})$$

with $T^*$ the corrected temperature, $\overline{T}_{obs}$ the average observed temperature of a 5-day block, including the 5 days of all considered years, $\sigma(T_{obs})$ the standard deviation of the observed temperature of that same 5-day block, $\sigma(T_{unc})$ the standard deviation of the uncorrected HI-AWARE temperature for that block, $T_{unc}$ the uncorrected HI-AWARE temperature for the day to correct, and $\overline{T}_{unc}$ the average uncorrected temperature of that 5-day block. More details



regarding this bias-correction method can be found in *Terink et al.* [2010]. The correction parameters were determined for each of the three temperature stations, and were subsequently interpolated to the model grid domain using nearest-neighbor interpolation.

Figure 13 shows the average monthly observed, uncorrected and bias-corrected temperature for the 3 station locations. It can be concluded that the correction performs very well. Daily values of bias-corrected temperature also show better comparison with the observations, as is shown in the scatter-plots of Figure 15. Since temperature is also corrected for the variance it is interesting to compare the histograms of the observed, uncorrected, and corrected temperature with each other (Figure 16). It is clear that the statistics and shape of the bias-corrected temperature histograms are the best match with the histograms of the observed temperature.

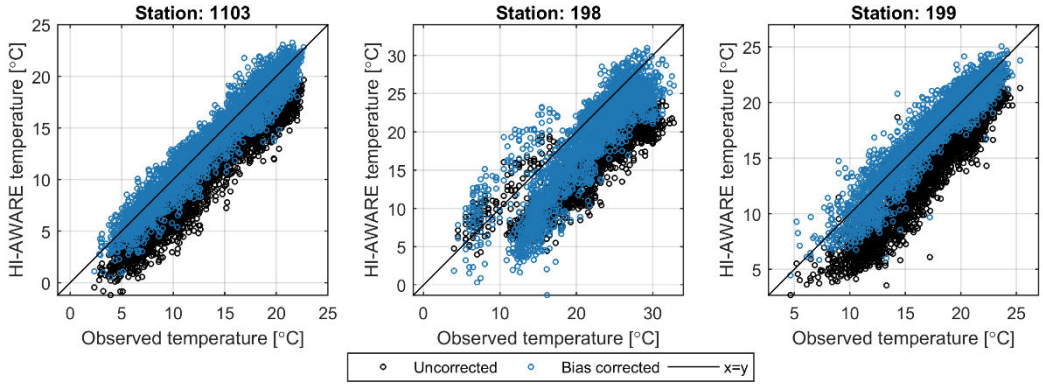


**Figure 15: Scatter-plots of observed daily temperature vs. uncorrected and bias-corrected daily temperature for the three station locations for the period 2000-2009.**

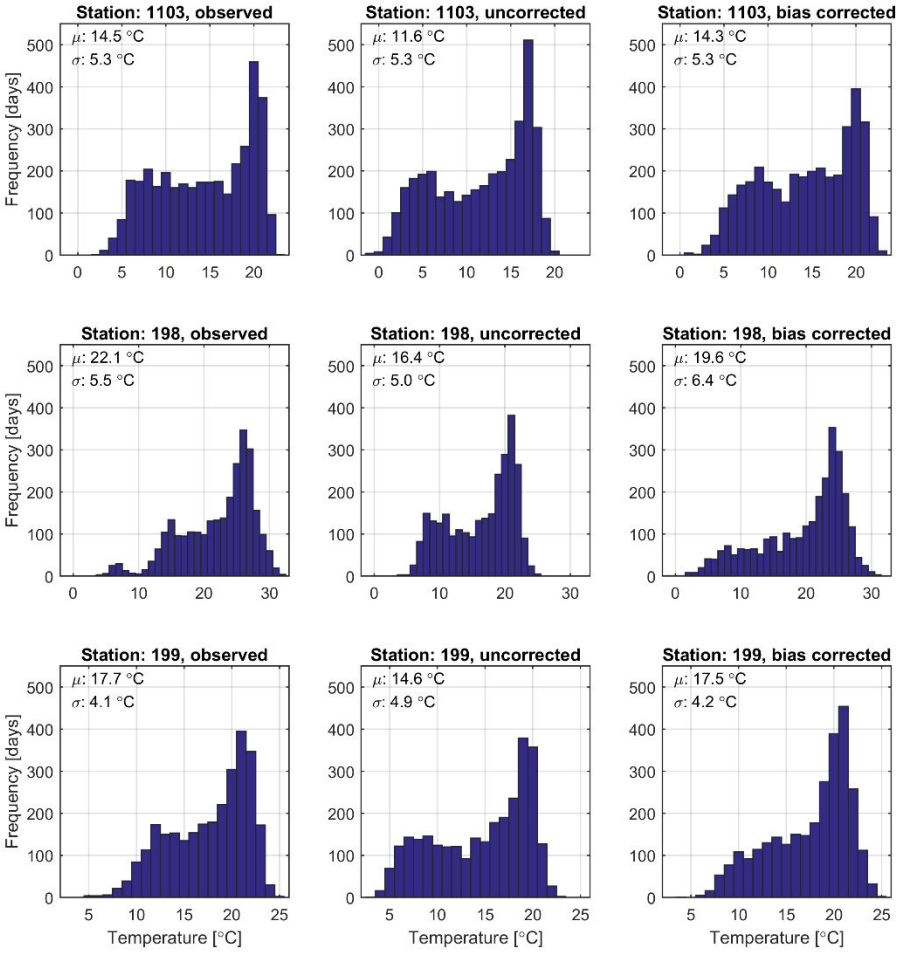


**Figure 16: Histograms (bin width 1°C) of observed, uncorrected, and bias-corrected daily temperature for the period 2000-2009.**

# 7 Climate Change Scenarios

## 7.1 Background information

### *7.1.1 Representative concentration pathways*

Since the release of Intergovernmental Panel on Climate Change's fifth Assessment Report, four representative concentration pathways (RCPs) have been defined as a basis for long-term and near-term climate modeling experiments in the climate modeling community [*van Vuuren et al.*, 2011]. The four RCPs together span the range of radiative forcing values for the year 2100 as found in literature, from 2.6 to 8.5 $Wm^{-2}$ (Table 3, Figure 17). Climate modelers use the time series of future radiative forcing from the four RCPs for their climate modeling experiments to produce climate scenarios. The development of the RCPs allowed climate modelers to proceed with experiments in parallel to the development of emission and socio-economic scenarios [*Moss et al.*, 2010]. The four selected RCPs were considered to be representative of the literature, and included one mitigation scenario (RCP2.6), two medium stabilization scenarios (RCP4.5/RCP6) and one very high baseline emission scenario (RCP8.5) [*van Vuuren et al.*, 2011].

Since the four RCPs are considered to be representative of radiative forcing that can be expected by 2100, each of them should theoretically be considered with equal probability to be included in climate change impact studies. However, in climate change impact studies there is usually a trade-off in how many RCPs and how many climate models can be included within the available time and resources, whilst at the same time having the ability of producing robust and reliable results.

**Table 3: Description and visualization of the four representative concentration pathways (RCPs) [*van Vuuren et al.*, 2011].**

| RCP | Description |
|---|---|
| **RCP8.5** | Rising radiative forcing pathway leading to 8.5 $Wm^2$ (~1370 ppm $CO_2$eq) by 2100 |
| **RCP6** | Stabilization without overshoot pathway to 6 $Wm^2$ (~850 ppm $CO_2$eq) at stabilization after 2100 |
| **RCP4.5** | Stabilization without overshoot pathway to 4.5 $Wm^2$ (~650 ppm $CO_2$eq) at stabilization after 2100 |
| **RCP2.6** | Peak in radiative forcing at ~3 $Wm^2$ (~490 ppm $CO_2$eq) before 2100 and then decline (the selected pathway declines to 2.6 Wm2 by 2100 |

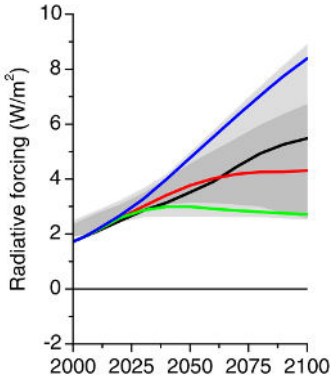


**Figure 17: RCPs. blue: RCP8.5, black: RCP6, red: RCP4.5, green: RCP2.6 [van Vuuren et al., 2011].**

### *7.1.2 Types of climate models*

Climate is modeled at different spatial scales. General Circulation Models (GCMs) are used to simulate global climate and operate at spatial resolutions ranging from ~100 $km^2$ to ~250 $km^2$. Regional Climate Models (RCMs) can be used to simulate regional climate at a typical resolution of ~10-50 km. Climate change information is usually required at a higher spatial

resolution since applications like hydrological models, forced by the data from GCMs or RCMs, operate at higher resolutions, down to several meters. The hydrological model used in this project operates at 250x250 m spatial resolution. This requires additional downscaling.

The current state-of-the-art GCMs are organized in the fifth Coupled Model Inter-comparison Project (CMIP5) archive [*Taylor et al.*, 2012], which was used as a basis by the IPCC for the generation of its fifth Assessment Report.

### *7.1.3 Downscaling*

Because of the discrepancy in spatial resolution, different downscaling techniques can be applied to overcome differences in resolution when climate models are used to force other models such as hydrological models. Downscaling techniques can be divided in two groups: dynamical downscaling and empirical-statistical downscaling [*Wilby and Wigley*, 1997].

#### 7.1.3.1 Dynamical downscaling

Dynamical downscaling is the nesting of climate models of different spatial resolutions. A GCM, operating at spatial resolutions ranging from ~100 km$^2$ to ~250 km$^2$ usually provides the boundary conditions for a RCM that has a nested domain within the GCM domain, and operates at a resolution of ~10-50 km$^2$. Higher resolutions can be reached when a finer resolution RCM or a high-resolution numerical weather prediction model (which needs to be non-hydrostatic in mountainous areas) is nested within the RCM domain. The RCM then in turn provides the boundary conditions for the finer resolution RCM. On finer scales, Large Eddy Simulation (LES) models can be deployed, which can include atmospheric turbulence in the simulations. Because of the high spatial resolution of RCMs, computational resources are a limiting factor for the temporal and spatial coverage of the simulation [*Fowler et al.*, 2007].

#### 7.1.3.2 Empirical-statistical downscaling

In most climate types, but especially in climate types with large spatial variation, such as the climate in mountainous regions, the GCM or RCM resolution is generally not sufficient to satisfactory simulate the climate, because climatic variables vary strongly over short distances due to orographic effects. Many processes such as local circulation patterns leading to hydrological extreme events cannot be resolved by GCMs [Christensen and Christensen, 2002]. Besides a gap in resolution, GCMs and RCMs exhibit biases with respect to observed climate data. To try to overcome these two problems, additional empirical-statistical downscaling and error correction techniques are required to account for the scale differences between GCMs or RCMs and hydrological models, and to correct for systematic biases between GCMs or RCMs and local-scale observations (Figure 18). Empirical-statistical methods are based on statistical relationships between large-scale predictors (climate model data) and local-scale observations [Wilby and Wigley, 1997; Fowler et al., 2007; Maraun et al., 2010]. Advantages of statistical downscaling methods include the possibility to provide point-scale climatic variables derived from GCM scale climate model output, the ability to directly incorporate observed data and the computational efficiency compared to dynamical downscaling. Important disadvantages on the other hand, include the requirement of a sufficiently long and reliable observed historical data series for calibration and the assumption that the statistical relationship between the large-scale data and the local-scale data stays constant in the future [Wilby and Wigley, 1997; Fowler et al., 2007].

*Maraun et al.* [2010] categorize statistical downscaling methods into ‘perfect prognosis (PP)’, which include regression models and weather typing schemes, ‘model output statistics (MOS)’,



and ‘weather generators (WG)’. Here the categorization by *Maraun et al.* [2010] is followed to summarize the different approaches for statistical downscaling.

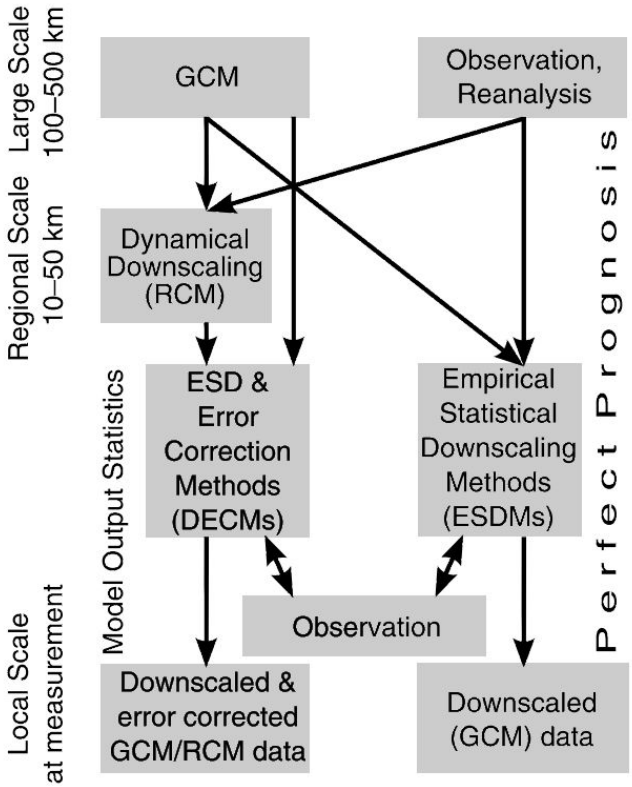


**Figure 18: Scheme of different statistical downscaling approaches. Traditional empirical-statistical downscaling (right pathway) calibrates the statistical transfer function between large-scale observation/reanalysis data and local-scale observations. Empirical-statistical downscaling and error correction methods (DECMs) (left pathway) are calibrated on RCM or GCM data and local observations, account for downscaling as well as model errors. Adapted from Themeßl et al. [2011a].**

Perfect Prognosis statistical downscaling approaches (or traditional empirical-statistical downscaling methods [*Themeßl et al.*, 2011b]) establish links between observed large-scale predictors and observed local-scale predictands. Often, the large-scale observations are replaced by data from reanalysis products. As predictors, variables with high predictive power to predict the variable of interest should be used. These can include various predictors representing the atmospheric circulation, humidity and temperature [*Maraun et al.*, 2010]. Different statistical models can be used to represent the statistical relationships between the large-scale observations and the local-scale observations. These include regression models, which can be linear models, more complex generalized linear models, generalized additive models, vector generalized linear models, or non-linear regression models [*Maraun et al.*, 2010]. Weather type based downscaling is based on the relation of different weather classes to local climate. Climate change can then be estimated by evaluating the change in frequency of the weather classes in the climate model [*Fowler et al.*, 2007].

In Model Output Statistics (MOS) approaches, the statistical relationship between predictors and predicted values is established by using simulated predictor values instead of observed values [*Maraun et al.*, 2010]. MOS combines a downscaling and an error correction step [*Themeßl et al.*, 2011a]. The predictors can be simulated time series or properties of the distributions of climatic variables. The predicted values can be local-scale time series or local-

scale distributions of the variable of interest. MOS is mostly used for RCM downscaling, while MOS application for GCM downscaling is still limited [*Eden et al.*, 2012; *Eden and Widmann*, 2014]. Multiple post-processing methods, termed empirical-statistical downscaling and error correction methods (DECMs, Figure 18), are based on the MOS approach [*Themeßl et al.*, 2011a]. The most basic MOS approach is the simple delta change or perturbation method [*Prudhomme et al.*, 2002; *Kay et al.*, 2008], which downscales climate models to local scale using change factors. Differences between a future and control GCM run are superimposed on a local-scale baseline observation dataset. Because of the simplicity of this method, a large number of climate models can be downscaled, facilitating the possibility to use a large ensemble of possible future climates in climate change impact studies [*Wilby and Wigley*, 1997]. The major shortcoming of this method is the fact that only changes in the mean, minima and maxima of climatic variables are considered [*Fowler et al.*, 2007], making this less suitable to assess changes in the distribution's tails, i.e. the extreme weather events. Another method with a slightly different concept is the scaling method or direct approach [*Widmann and Bretherton*, 2003; *Lenderink et al.*, 2007]. In this approach the future precipitation is determined as the simulated future precipitation scaled to the ratio of the mean observed and mean control run precipitation.

The Advanced Delta Change (ADC) approach [*van Pelt et al.*, 2012], built on work by *Leander and Buishand* [2007], has the advantage over the classical delta change method that not only changes in the mean are considered, but also the changes in extremes, thus making a non-linear transformation of climate signals derived from climate models. Besides, changes in multi-day precipitation events are also modeled. The approach has been successfully applied in the Rhine basin in Europe [*Terink et al.*, 2010; *van Pelt et al.*, 2012]. To test the usefulness of the initial non-linear bias-correction approach developed by *Leander and Buishand* [2007] in complex, orographically influenced climate systems, it was used to bias-correct RCM temperature and precipitation for the upper Rhone basin in Switzerland [*Bordoy and Burlando*, 2013]. The authors concluded that the method is able to dramatically reduce the RCM errors for both air temperature and precipitation and that the method could be used successfully for correcting future projections. However, they also observed that an undesired effect of the technique developed by *Leander and Buishand* [2007] was that it generated extreme precipitation values which considerably exceeded the range of the observations.

Quantile mapping [*Boe et al.*, 2007; *Deque*, 2007; *Themeßl et al.*, 2011b] is based on the principle of comparing distributions of a climatic variable in a dataset of historical observations and climate model control run and defining an error function to correct for biases for each quantile in the distribution. This error function is applied to a future climate model run to correct future climate data. The approach can be based on empirical or fitted probability distributions [*Piani et al.*, 2010; *Themeßl et al.*, 2011a]. New extremes can be simulated by linear extrapolation of the error function outside the range of the distribution in the calibration period [*Themeßl et al.*, 2011a].

## 7.2 Selection of climate models

Due to their coarse spatial resolution, outputs from General Circulation Models (GCMs) are usually directly downscaled to higher resolution using empirical-statistical downscaling methods, or used as boundary conditions for Regional Climate Models (RCMs), with their outputs being downscaled to higher resolution subsequently. The downscaled outputs are then used to assess future climatic changes and to drive other sector-specific models for climate change impact studies.



The number of GCMs available for climate change projections is increasing rapidly. For example, the CMIP3 archive [*Meehl et al.*, 2007], which was used for the 4th IPCC Assessment Report [*IPCC*, 2007] contains outputs from 25 different GCMs, whereas the CMIP5 archive [*Taylor et al.*, 2012], which was used for the 5th IPCC Assessment Report [*IPCC*, 2013], contains outputs from 61 different GCMs. These GCMs often have multiple ensemble members resulting in an even larger number of available model runs.

Despite improvements in the CMIP5 models compared to CMIP3 in terms of process representation [e.g. *Blázquez and Nuñez*, 2013; *Sperber et al.*, 2013], uncertainty about the future climate remains large [e.g. *Knutti and Sedláček*, 2012], and locally even increases with the larger number of models available [e.g. *Joetzjer et al.*, 2013; *Lutz et al.*, 2013]. Considering the large number of available climate models and constraints in the available computational and human resources, detailed climate change impact studies cannot include all projections. In practice, rather one climate model or a small ensemble of climate models is selected for the assessment. Despite the importance of using an ensemble that is representative for the region of interest and shows the full uncertainty range, the selection of models to be included in the ensemble is not straightforward, and can be based on multiple criteria.

The uncertainty originating from the spread in climate models' projections is considered to be a large source of uncertainty in climate change impact studies, e.g.: this uncertainty is often larger than model parameter uncertainties, uncertainty stemming from natural variability and structural uncertainties in hydrological models [*Minville et al.*, 2008; *Finger et al.*, 2012]. Therefore, the selection of climate models is a crucial step when conducting a climate change impact study.

Often climate models are selected based on their skill to simulate the present and near-past climate [e.g. *Biemans et al.*, 2013; *Pierce et al.*, 2009]. Another approach is the so-called envelope approach, where an ensemble of models covering a wide range of projections for one or more climatological variables of interest is selected from the pool of available models. This approach aims at covering all possible futures as projected by the entire pool of climate models. Some approaches consider only the changes in mean air temperature and total annual precipitation [e.g. *Immerzeel et al.*, 2013; *Sorg et al.*, 2014; *Warszawski et al.*, 2014], whereas other approaches consider more climatological variables using cluster analysis algorithms [e.g. *Cannon*, 2014; *Houle et al.*, 2012]. Other methodologies combine the past-performance approach and the envelope approach [*Lutz et al.*, 2016b; *Wilcke and Bärring*, 2016].

For this study we apply the advanced envelope-based selection approach described by [*Lutz et al.*, 2016b] to select a representative ensemble of GCMs. This approach follows three steps (Figure 19):

1. Initial selection based on changes in mean air temperature and annual precipitation sum;
2. Refined selection based on projected changes in four indices for climatic extremes;
3. Final selection based on model skill in simulating the annual cycle of air temperature and precipitation.

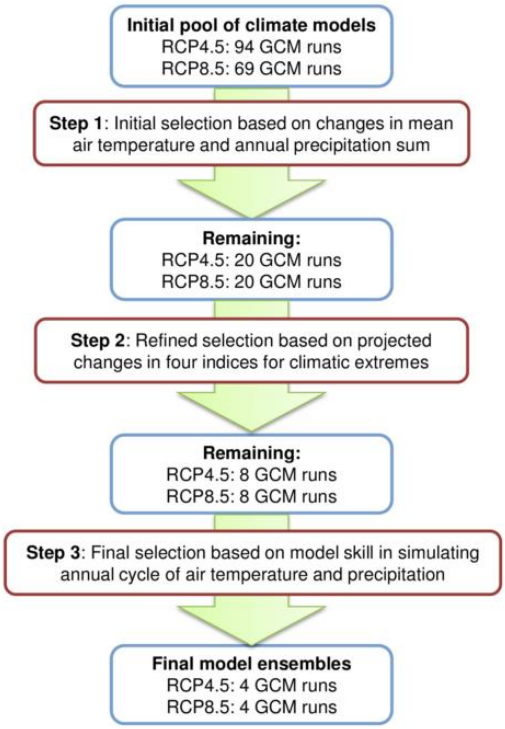


**Figure 19: Climate model selection procedure [Lutz et al., 2016b].**

### *7.2.1 Selection of representative concentration pathways*

We select two ensembles containing four GCM runs from the CMIP5 database: one ensemble for the medium stabilization scenario RCP4.5 and one ensemble for the very high radiative forcing scenario RCP8.5. We did not include the mitigation scenario leading to a very low radiative forcing level (RCP2.6). It is unlikely that this RCP can be met, since it requires an immediate drastic decline of emissions followed by ongoing carbon sequestration in the second half of the 21$^{st}$ century, whereas the future emissions expected to come from existing capital are large [*Arora et al.*, 2011; *Rosenberg et al.*, 2015]. As we aim to present robust, realistic projections in our study we choose not to include RCP2.6 in the climate model ensemble. By selecting RCP4.5 and RCP8.5 we cover the entire range of radiative forcing resulting from RCP4.5, RCP6 and RCP8.5.

### *7.2.2 Step 1: Initial selection based on changes in mean air temperature and annual precipitation sum*

The initial selection is based on the range of projections of changes in mean air temperature (ΔT) and annual precipitation sum (ΔP), between 1981-2010 and 2046-2075, for the GCM grid cell that covers the majority of the Tamakoshi River Basin (Figure 20). This calculation was done using the KNMI Climate Explorer (http://climexp.knmi.nl). For the model runs included in RCP4.5 and RCP8.5 separately, the 10$^{th}$ and 90$^{th}$ percentile values for ΔT and ΔP are determined, after resampling all GCM data to the same 2.5°x2.5° grid cell. These values represent the four corners of the spectrum of projections for temperature and precipitation change. The 10$^{th}$ percentile value for ΔT and 10$^{th}$ percentile value for ΔP are in the “cold, dry” corner of the spectrum. The 10$^{th}$ percentile value for ΔT and 90$^{th}$ percentile value for ΔP are in the “cold, wet” corner of the spectrum. The 90$^{th}$ percentile value for ΔT and 10$^{th}$ percentile value for ΔP are in the “warm, dry” corner of the spectrum. The 90$^{th}$ percentile value for ΔT and 90$^{th}$ percentile value for ΔP are in the “warm, wet” corner of the spectrum. The 10$^{th}$ and 90$^{th}$

percentile values are chosen rather than the minimum and maximum projections to avoid selecting outliers, cf. other studies [e.g. *Immerzeel et al.*, 2013; *Sorg et al.*, 2014]. The proximity of the model runs to the 10th and 90th percentile values is derived from the model runs' percentile rank scores corresponding to their projections for ΔT and ΔP with respect to the entire range of projections in the entire ensemble:

$$D_{P_i^T,P_i^P} = \sqrt{\left(\left(\left|P_i^T - P_j^T\right|\right)^2 + \left(\left|P_i^P - P_j^P\right|\right)^2\right)} \qquad \text{(Eq. 1)}$$

where $D_{P_i^T,P_i^P}$ is the distance of a model (j)'s ΔT and ΔP ($P_j^T$ and $P_j^P$ respectively) to the corner (i)'s 10th and/or 90th percentile score of ΔT and ΔP for the entire ensemble ($P_i^T$ and $P_i^P$ respectively). For each corner the five models with the lowest values for D and data available at a daily time step are selected from the ensemble. We select only models that have data available at a daily time step because this is a requirement for an empirical-statistical downscaling method to be applied to the GCM runs in a later stage. Nonetheless, model runs with data available at larger time steps are included in the initial pool of available model runs used to calculate the model runs' percentile scores, to have a complete representation of all projected possible futures. The initial selection results in 5 model runs x 4 corners = 20 model runs for each RCP (Figure 21).

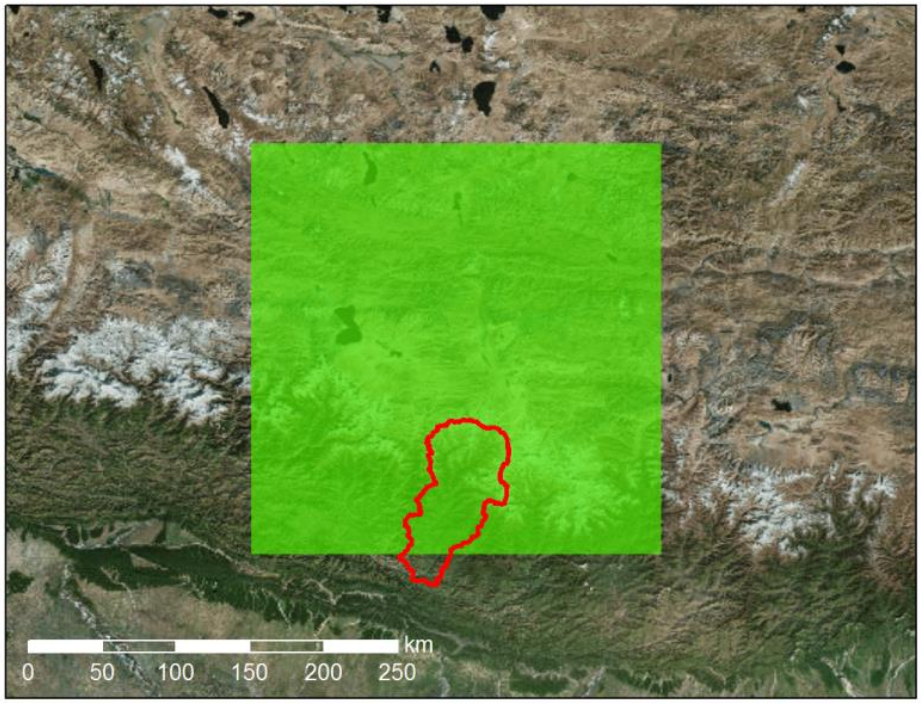


**Figure 20: Tamakoshi River Basin boundary indicated by red line. GCM grid cell covering the majority of the river basin indicated by green rectangle.**

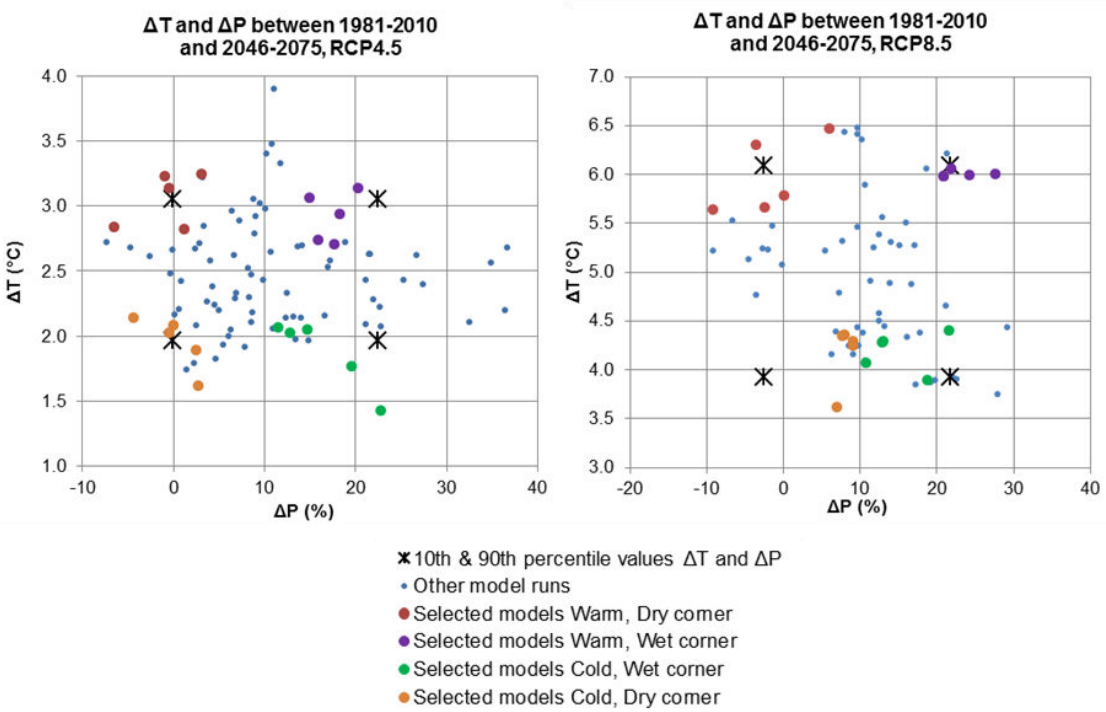


**Figure 21: Changes in mean air temperature and annual precipitation sum for RCP4.5 (left) and RCP8.5 (right) CMIP5 GCM runs for the Tamakoshi River Basin. Models selected during step 1 are indicated with colored dots.**

**Table 4: Description of ETCCDI indices used in step 2 of the climate model selection procedure.**

| Meteorological variable | ETCCDI index | Index description |
|---|---|---|
| Precipitation | R99pTOT | precipitation due to extremely wet days (> 99$^{th}$ percentile) |
| Precipitation | CDD | consecutive dry days: maximum length of dry spell (P < 1 mm) |
| Air temperature | WSDI | warm spell duration index: count of days in a span of at least six days where TX > 90$^{th}$ percentile ($TX_{ij}$ is the daily Tmax on day i in period j) |
| Air temperature | CSDI | Cold spell duration index: count of days in a span of at least six days where TN < 10$^{th}$ percentile (TNij is the daily Tmin on day i in period j |

### *7.2.3 Step 2: Refined selection based on projected changes in four indices for climatic extremes*

The number of model runs remaining after the initial selection process is further reduced during the refined selection step. In this step, the model runs are evaluated for their projected changes in climatic extremes. We evaluate the changes in climatic extremes for air temperature and precipitation, by considering the changes in two ETCCDI indices [*Peterson*, 2005] (Table 4) for both air temperature and precipitation. For characterization of changes in air temperature extremes we analyze changes in the warm spell duration index (WSDI) and the cold spell duration index (CSDI). For characterization of changes in precipitation extremes we consider the precipitation due to extremely wet days (R99pTOT) and the number of consecutive dry days (CDD). Since the climate model ensemble will be used to force a hydrological model, we have

chosen to analyze changes in R99pTOT and CDD as obvious indicators of precipitation extremes leading to associated hydrological extremes whereas CDD is an important indicator for dry spells that affect hydropower generation. Changes in WSDI and CSDI both have effects on the cryospheric processes (snow- and ice melt/accumulation), which are important in our study area. The indices are calculated from the daily model output, for each individual year in the future period (2046-2175) and reference period (1981-2010), for the GCM grid cells covering the study area (Figure 20). For both periods, the indices are then averaged over the period of thirty years. The changes in the indices are then calculated as a percentual change for the future period with respect to the reference period.

For each model selected during the initial selection, the most relevant index for air temperature and the most relevant index for precipitation are considered. For example, for the models in the warm, wet corner, WSDI indicating warm spells and R99pTOT indicating extreme precipitation events are considered. CDD and CSDI are not considered in that case, but they are considered for models in the dry and cold corners respectively. For the five models initially selected for each corner, the two relevant indices are both ranked and given scores 1 to 5. For example, in the warm, wet corner the model with the largest increase in R99pTOT scores 5 points for that index whereas the model with the smallest increase in R99pTOT scores 1 point for that index. Similarly, the model with the largest increase in WSDI scores 5 points for that index and the model with the smallest increase in WSDI scores 1 point for that index. Both scores are then averaged to obtain a final score. Based on that final score, the two models with the highest scores are selected (Table 5). Thus for each corner the number of models is reduced from five to two models. For each RCP 4 corners x 2 models = 8 models are selected, which are validated to the climatic reference product in the next step.

**Table 5: GCM runs analyzed during the refined selection step. Models selected for step 3 are indicated with yellow color.**

| RCP | Projection | model | ΔR99P (%) | ΔCDD (%) | ΔWSDI (%) | ΔCSDI (%) | ΔT (°C) | ΔP (%) | T index rank | P index rank | Combined score |
|---|---|---|---|---|---|---|---|---|---|---|---|
| RCP4.5 | Warm, dry | CMCC-CM_r1i1p1 | 167.3 | 13.2 | 1628.2 | -97.9 | 3.2 | -0.8 | 4 | 3 | 3.5 |
| | | CMCC-CMS_r1i1p1 | 68.3 | 18.2 | 811.7 | -100.0 | 3.1 | -0.5 | 3 | 4 | 3.5 |
| | | HadGEM2-AO_r1i1p1 | 35.2 | 25.3 | 640.5 | -90.4 | 2.8 | 1.3 | 1 | 5 | 3.0 |
| | | IPSL-CM5A-LR_r4i1p1 | 16.6 | 1.5 | 1921.8 | -98.7 | 3.2 | 3.2 | 5 | 1 | 3.0 |
| | | MPI-ESM-LR_r2i1p1 | 68.1 | 12.5 | 790.2 | -97.8 | 2.8 | -6.5 | 2 | 2 | 2.0 |
| | Warm, wet | CanESM2_r1i1p1 | 121.4 | -6.1 | 540.3 | -91.8 | 2.9 | 18.3 | 3 | 4 | 3.5 |
| | | CanESM2_r3i1p1 | 113.3 | -9.9 | 530.2 | -100.0 | 3.1 | 14.9 | 2 | 3 | 2.5 |
| | | CanESM2_r4i1p1 | 159.7 | -11.9 | 582.0 | -93.6 | 2.7 | 15.9 | 4 | 5 | 4.5 |
| | | IPSL-CM5A-MR_r1i1p1 | 71.8 | -17.8 | 744.0 | -94.8 | 3.1 | 20.3 | 5 | 1 | 3.0 |
| | | CanESM2_r2i1p1 | 102.9 | -8.8 | 459.7 | -97.3 | 2.7 | 17.7 | 1 | 2 | 1.5 |
| | Cold, wet | bcc-csm1-1_r1i1p1 | 127.8 | -4.6 | 953.0 | -97.9 | 1.8 | 19.6 | 1 | 5 | 3.0 |
| | | IPSL-CM5B-LR_r1i1p1 | 71.1 | -12.2 | 535.2 | -92.9 | 1.4 | 22.8 | 5 | 2 | 3.5 |
| | | CESM1-BGC_r1i1p1 | 114.0 | -4.3 | 467.1 | -94.2 | 2.0 | 14.7 | 4 | 4 | 4.0 |
| | | GISS-E2-R_r6i1p1 | -16.7 | -9.2 | 722.0 | -97.6 | 2.0 | 12.9 | 2 | 1 | 1.5 |
| | | NorESM1-M_r1i1p1 | 99.3 | 11.5 | 702.9 | -97.1 | 2.1 | 11.6 | 3 | 3 | 3.0 |
| | Cold, dry | bcc-csm1-1-m_r1i1p1 | 67.8 | 0.7 | 844.2 | -96.7 | 2.0 | -0.5 | 2 | 2 | 2.0 |
| | | inmcm4_r1i1p1 | 3.8 | 11.1 | 685.7 | -76.4 | 1.6 | 2.8 | 5 | 4 | 4.5 |
| | | MPI-ESM-MR_r1i1p1 | 89.0 | 2.4 | 689.3 | -93.2 | 2.1 | -4.3 | 4 | 3 | 3.5 |
| | | MPI-ESM-MR_r2i1p1 | 27.6 | 13.0 | 871.7 | -94.4 | 2.1 | 0.1 | 3 | 5 | 4.0 |
| | | MRI-CGCM3_r1i1p1 | 83.1 | -0.6 | 448.7 | -99.0 | 1.9 | 2.6 | 1 | 1 | 1.0 |
| RCP8.5 | Warm, dry | CMCC-CM_r1i1p1 | 407.5 | 19.4 | 3258.3 | -100.0 | 5.8 | 0.2 | 5 | 2 | 3.5 |
| | | CMCC-CMS_r1i1p1 | 173.6 | 30.4 | 1555.9 | -100.0 | 6.3 | -3.5 | 1 | 4 | 2.5 |
| | | IPSL-CM5A-LR_r2i1p1 | 210.9 | 19.3 | 2460.3 | -100.0 | 6.5 | 6.0 | 4 | 1 | 2.5 |
| | | MPI-ESM-LR_r2i1p1 | 108.2 | 28.9 | 1953.9 | -100.0 | 5.6 | -9.1 | 2 | 3 | 2.5 |
| | | MPI-ESM-LR_r3i1p1 | 97.6 | 39.9 | 2358.8 | -99.7 | 5.7 | -2.4 | 3 | 5 | 4.0 |
| | Warm, wet | CanESM2_r1i1p1 | 200.5 | -13.4 | 1153.9 | -98.8 | 6.0 | 24.3 | 3 | 1 | 2.0 |
| | | CanESM2_r2i1p1 | 277.7 | -8.8 | 1080.3 | -98.6 | 6.1 | 21.9 | 1 | 2 | 1.5 |
| | | CanESM2_r4i1p1 | 333.2 | -13.1 | 1283.2 | -100.0 | 6.0 | 21.0 | 4 | 3 | 3.5 |
| | | CanESM2_r5i1p1 | 387.5 | 4.0 | 1125.2 | -100.0 | 6.0 | 27.7 | 2 | 5 | 3.5 |
| | | IPSL-CM5A-MR_r1i1p1 | 379.8 | 23.0 | 3429.0 | -100.0 | 6.2 | 21.3 | 5 | 4 | 4.5 |
| | Cold, wet | bcc-csm1-1_r1i1p1 | 229.2 | -15.2 | 2139.7 | -100.0 | 4.4 | 21.7 | 1 | 4 | 2.5 |
| | | CCSM4_r2i1p1 | 159.1 | 4.9 | 2483.0 | -100.0 | 4.1 | 10.8 | 1 | 2 | 1.5 |
| | | CNRM-CM5_r1i1p1 | 222.7 | -4.1 | 1167.4 | -98.2 | 3.9 | 18.9 | 4 | 3 | 3.5 |
| | | EC-EARTH_r9i1p1 | 68.9 | 1.6 | 1476.8 | -84.6 | 4.3 | 13.0 | 5 | 1 | 3.0 |
| | | MIROC5_r1i1p1 | 411.7 | -3.0 | 1734.5 | -100.0 | 4.3 | 13.0 | 1 | 5 | 3.0 |
| | Cold, dry | CCSM4_r1i1p1 | 162.7 | 16.1 | 2628.1 | -99.9 | 4.3 | 9.2 | 3 | 3 | 3.0 |
| | | CCSM4_r6i1p1 | 71.8 | -3.3 | 1134.0 | -87.4 | 4.2 | 9.1 | 5 | 2 | 3.5 |
| | | inmcm4_r1i1p1 | 1.7 | 20.8 | 1614.4 | -92.4 | 3.6 | 7.0 | 4 | 5 | 4.5 |
| | | MRI-CGCM3_r1i1p1 | 136.1 | -9.8 | 1185.7 | -100.0 | 4.4 | 8.0 | 1 | 1 | 1.0 |
| | | NorESM1-M_r1i1p1 | 129.5 | 20.8 | 1024.9 | -100.0 | 4.3 | 7.7 | 1 | 4 | 2.5 |

### *7.2.4 Final selection based on model skill in simulating the annual cycle of air temperature and precipitation.*

The final selection of models is based on a validation of model performance to the selected HI-AWARE reference climate dataset (Table 2) [*Lutz and Immerzeel*, 2015]. For mean air temperature and precipitation sum, the bias between the GCM run and the reference dataset is calculated on annual basis and for the key seasons (monsoon (June-Sep) and winter (December-Feb)). The biases for precipitation are expressed as a percentage and the biases for air temperature are expressed as degrees Celsius. The biases are normalized and expressed as a fraction of the largest found bias within the ensemble (Table 6). For example,



for the CMCC-CMS_r1i1p1 model run for RCP4.5, the normalized P bias for the monsoon is 0.4. The maximum bias for monsoon P in the RCP4.5 ensemble is -72.1% (IPSL-CM5B-LR-r1i1p1) whereas the bias for the CMCC-CMS_r1i1p1 model run is 26.7%. Thus the normalized P bias is 26.7 / 72.1 = 0.4. Normalized annual and seasonal scores are averaged for precipitation and temperature separately. Finally, a combined score is calculated by summing the resulting two values. In each corner (warm/wet, warm/dry, etc.), the GCM run with the lowest scores, indicating the lowest bias, is selected. The selected models form the climate model ensemble that will be downscaled before they are used in the climate change impact assessment.

**Table 6: Biases between GCM runs and reference climate dataset for the Tamakoshi River Basin.**

| RCP | Projection | model | P bias total (%) | P bias monsoon (%) | T bias total (°C) | T bias monsoon (°C) | T bias winter (°C) | P bias total normalized | P bias monsoon normalized | T bias total normalized | T bias monsoon normalized | T bias winter normalized | P bias score | T bias score | Combined score |
|---|---|---|---|---|---|---|---|---|---|---|---|---|---|---|---|
| RCP4.5 | Warm, dry | CMCC-CM_r1i1p1 | 21.7 | 13.5 | -7.9 | -5.0 | -11.5 | 0.4 | 0.2 | 1.0 | 1.0 | 1.0 | 0.3 | 1.0 | 1.3 |
| | | CMCC-CMS_r1i1p1 | 37.2 | 26.7 | -0.6 | 0.1 | -8.3 | 0.7 | 0.4 | 0.1 | 0.0 | 0.3 | 0.5 | 0.1 | 0.7 |
| | Warm, wet | CanESM2_r1i1p1 | -34.5 | -30.4 | 1.4 | 3.3 | -0.7 | 0.7 | 0.4 | 0.2 | 0.7 | 0.1 | 0.5 | 0.3 | 0.8 |
| | | CanESM2_r4i1p1 | -30.7 | -27.3 | 1.3 | 3.0 | -0.1 | 0.6 | 0.4 | 0.2 | 0.6 | 0.0 | 0.5 | 0.2 | 0.7 |
| | Cold, wet | IPSL-CM5B-LR_r1i1p1 | -40.3 | -72.1 | -5.7 | -3.4 | -6.5 | 0.8 | 1.0 | 0.7 | 0.7 | 0.6 | 0.9 | 0.7 | 1.6 |
| | | CESM1-BGC_r1i1p1 | 45.5 | 53.3 | -4.5 | -1.7 | -8.1 | 0.9 | 0.7 | 0.6 | 0.3 | 0.7 | 0.8 | 0.5 | 1.3 |
| | Cold, dry | inmcm4_r1i1p1 | -10.4 | -21.2 | -3.4 | -0.2 | -6.9 | 0.2 | 0.3 | 0.4 | 0.0 | 0.6 | 0.2 | 0.4 | 0.6 |
| | | MPI-ESM-MR_r2i1p1 | 52.3 | 54.7 | -0.7 | -0.3 | -3.8 | 1.0 | 0.8 | 0.1 | 0.1 | 0.2 | 0.9 | 0.1 | 1.0 |
| RCP8.5 | Warm, dry | CMCC-CM_r1i1p1 | 20.7 | 11.2 | -7.9 | -5.0 | -11.7 | 0.4 | 0.2 | 0.7 | 0.8 | 0.8 | 0.3 | 0.7 | 1.0 |
| | | MPI-ESM-LR_r3i1p1 | 55.6 | 60.9 | -0.9 | -0.6 | -4.7 | 1.0 | 1.0 | 0.1 | 0.1 | 0.2 | 1.0 | 0.1 | 1.1 |
| | Warm, wet | CanESM2_r4i1p1 | -32.6 | -29.8 | 1.4 | 3.0 | -0.5 | 0.6 | 0.5 | 0.1 | 0.4 | 0.0 | 0.5 | 0.2 | 0.7 |
| | | CanESM2_r5i1p1 | -34.1 | -31.4 | 1.2 | 3.2 | -0.7 | 0.6 | 0.5 | 0.1 | 0.5 | 0.0 | 0.6 | 0.2 | 0.7 |
| | | IPSL-CM5A-MR_r1i1p1 | 11.8 | 15.4 | -2.3 | -2.4 | -2.1 | 0.2 | 0.3 | 0.2 | 0.4 | 0.1 | 0.2 | 0.2 | 0.5 |
| | Cold, wet | CNRM-CM5_r1i1p1 | -12.6 | -22.3 | -11.5 | -6.6 | -15.6 | 0.2 | 0.4 | 1.0 | 1.0 | 1.0 | 0.3 | 1.0 | 1.3 |
| | | EC-EARTH_r9i1p1 | -14.8 | -19.7 | -4.0 | -3.8 | -4.4 | 0.3 | 0.3 | 0.3 | 0.6 | 0.3 | 0.3 | 0.4 | 0.7 |
| | | MIROC5_r1i1p1 | 37.8 | 37.8 | 2.0 | 2.4 | 0.2 | 0.7 | 0.6 | 0.2 | 0.4 | 0.0 | 0.7 | 0.2 | 0.8 |
| | Cold, dry | CCSM4_r6i1p1 | 51.4 | 58.1 | -4.5 | -1.8 | -7.8 | 0.9 | 1.0 | 0.4 | 0.3 | 0.5 | 0.9 | 0.4 | 1.3 |
| | | inmcm4_r1i1p1 | -10.9 | -22.0 | -3.3 | -0.2 | -6.2 | 0.2 | 0.4 | 0.3 | 0.0 | 0.4 | 0.3 | 0.3 | 0.5 |

## 7.3 Climate model downscaling

There are many different statistical downscaling approaches and choosing the most appropriate method is challenging, especially for complex mountainous climate types like in Tamakoshi River Basin. *Themeßl et al.* [2011b] compared different empirical-statistical downscaling methods for precipitation in the Austrian Alps and found that the Quantile Mapping method has best performance in mountainous climate, particularly at high quantiles, which is promising for assessing future changes in extreme precipitation events. Other advantages of Quantile Mapping are that i) it can be applied to other climatic variables, including air temperature, as well, and ii) that it useful for the analysis of extremes. A Quantile Mapping approach applied at catchment scale application in the Langtang and Baltoro catchments in Indus and Ganga basins was successful [*Immerzeel et al.*, 2013]. Because of its robustness and good performance over mountainous areas, we select the Quantile Mappig (QM) approach for the empirical-statistical downscaling of climate change scenarios in this project.

Quantile mapping is applied on a daily basis (t) and for each grid cell (i) separately resulting in a corrected time series $Y^{cor}$ using a correction function (CF) as defined here [*Themeßl et al.*, 2011b]:

$$Y_{t,i}^{cor} = X_{t,i}^{raw} + CF_{t,i} \quad \text{Eq. 2}$$

$$CF_{t,i} = ecdf_{m,i}^{obs,cal^{-1}}(P_{t,i}) - ecdf_{m,i}^{mod,cal^{-1}}(P_{t,i}) \quad \text{Eq. 3}$$

$$P_{t,i} = ecdf_{m,i}^{mod,cal}(X_{t,i}^{raw}) \quad \text{Eq. 4}$$

CF represents the difference between the observed (obs) and the modeled (mod) inverse empirical cumulative density distributions ($ecdf^{-1}$), for the representative day of the year (doy) in

the calibration period (cal) at probability P. P is obtained by relating the raw climate model output $X^{raw}$ to the corresponding ecdf in the calibration period. For QM calibration ecdfs are constructed for each month of the year (as in [*Immerzeel et al.*, 2013]). As observed data we use the bias-corrected HI-AWARE reference climate product (Section 6.1 and Section 6.2).

Figure 22 serves as an illustrated example of the QM methodology. The upper panel shows all daily temperature observations in July during 1981-2010 and the corresponding GCM values for one grid cell. For both distributions an empirical distribution function can be constructed (middle panel). With both ecdfs the correction function can be determined to correct GCM values from the future run to downscaled values (lower panel). If for example, the GCM future run projects T = 14 °C on 10 July 2073 (lower panel), then this value can be looked up in the ecdf from the GCM values in the control run (middle panel) and the corresponding value from the ecdf for observations can be determined (e.g. T = 12 °C). Thus the downscaled value will be 12 °C (lower panel). This is done for all daily values. The approach is comparative for other meteorological values, like for example precipitation (example in Figure 23).

As described in [*Themeßl et al.*, 2011b], the QM procedure can be extended by frequency adaptation (FA), to account for a methodological problem, occurring when the dry-day frequency in the model result is greater than in the observations, resulting in a systematic wet precipitation bias. Usually this is not the case because of the underestimate of the dry-day frequency ("drizzling effect") in GCMs and RCMs. Problems have however been reported with the so called summer drying problems of RCMs in south-eastern Europe [e.g. *Hagemann et al.*, 2004]. With FA, only the fraction $\Delta P_0 = \frac{\left(ecdf_{doy,i}^{mod,cal}(0) - ecdf_{doy,i}^{obs,cal}(0)\right)}{ecdf_{doy,i}^{obs,cal}(0)}$ of dry-day cases with probability $P_0$ are corrected randomly by linearly interpolating between zero precipitation and the precipitation amount of $ecdf_{doy,i}^{mod,cal^{-1}}\left(ecdf_{doy,i}^{mod,cal}(0)\right)$, i.e. the first precipitation class in QM without FA). We will first test the necessity of this additional extension for the HKH region.

In addition [*Themeßl et al.*, 2011b] further extended the QM methodology for improved simulation of new extremes, being values of extremes outside the range of the calibration period, by including constant extrapolation of the correction value (i.e. the difference between $ecdf^{obs,cal}$ and $ecdf^{mod,cal}$) at the highest and lowest quantiles of the calibration range. Considering the example in Figure 23, a value in the future GCM run of 80 mm is outside the range of the ecdf of the GCM control run. In that case the future downscaled value would be determined as:

$$P_{Future_{DS}} = \max(P_{OBS}) \cdot \frac{P_{FUTURE_{GCM}}}{\max\left(P_{FUTURE_{GCM}}\right)} = 35 \cdot \frac{80}{65} = 43\ mm$$



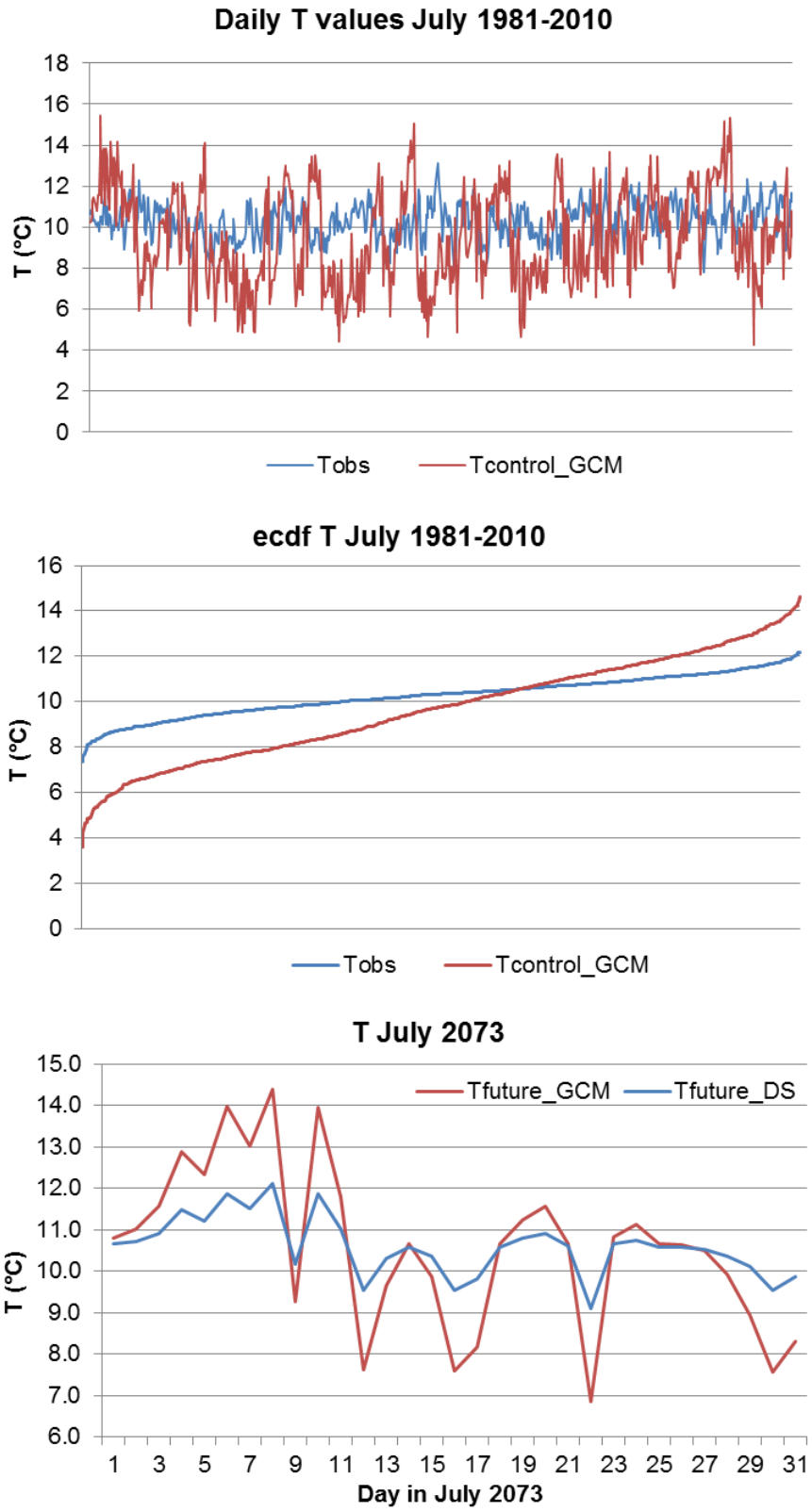


**Figure 22: Illustrative example of GCM signal downscaling by Quantile Mapping for one grid cell. Upper panel: All daily observations and GCM control run values for days in July during control period (1981-2010). Middle panel: Empirical distribution functions (ecdf) constructed for observations and GCM control run values in upper panel. Lower panel: Future daily temperature for a July in the future as from raw GCM input and corresponding downscaled values.**

For this project, the downscaling procedure is as follows:

1) GCM runs for the reference period (1981-2010) are resampled and smoothed to the hydrological model resolution.
2) For each hydrological model grid cell the ecdfs are determined for two variables (Tavg and P) for grid cells in the reference climate dataset for 1981-2010 and the grid cells in the GCM simulations for 1981-2010 for each month (Jan-Dec)
3) Future GCM data (2011-2075), for each of the 8 GCMs is resampled and smoothed to the hydrological model resolution.
4) Future GCM data for each of the 8 GCMs, is corrected for each day for each hydrological model grid cell for each of the 2 meteorological parameters for each studied time slice in the future are corrected to generate downscaled hydrological model forcing.

Maximum and minimum daily temperature (Tmax and Tmin) are downscaled differently. For this we have assumed that the range between Tmax and Tavg, and Tmin and Tavg is correctly represented in the GCMs. Therefore, we have downscaled these forcings according to the procedure below:

1. Project and resample Tavg, Tmax, and Tmin to the hydrological model resolution.
2. Calculate the difference between the resampled GCM Tmax and Tavg:
   Tmx_diff = Tmax – Tavg
3. Calculate the difference between the resampled GCM Tmin and Tavg:
   Tmn_diff = Tmin – Tavg
4. Use the downscaled Tavg from the QM methodology (see step 4 above)
5. Add the differences from step 2 and step 3 to the downscaled Tavg to calculate the downscaled Tmax and Tmin:
   a. Tmax_downscaled = Tavg(QM) + Tmx_diff
   b. Tmin_downscaled = Tavg(QM) + Tmn_diff



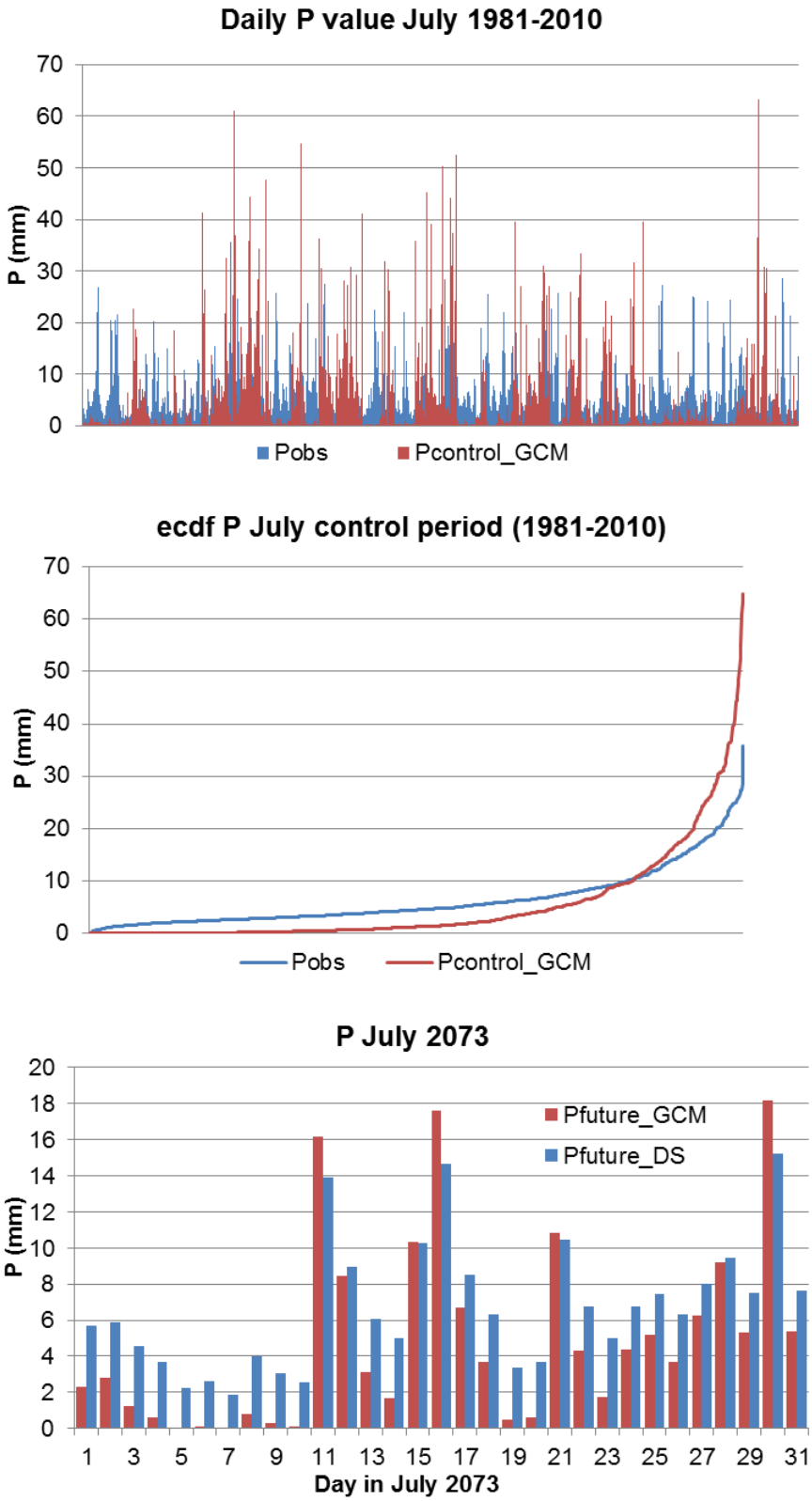


**Figure 23: Illustrative example of GCM signal downscaling by Quantile Mapping for one grid cell. Upper panel: All daily observations and GCM control run values for days in July during control period (1981-2010). Middle panel: Empirical distribution functions (ecdf) constructed for observations and GCM control run values in upper panel. Lower panel: Future daily temperature for a July in the future as from raw GCM input and corresponding downscaled values.**

# 8 SPHY model and calibration

## 8.1 Introduction to the SPHY model

The Spatial Processes in HYdrology (SPHY) model [*Terink et al.*, 2015] was developed with the explicit aim to simulate terrestrial hydrology at flexible scales, under various land use and climate conditions. SPHY is a spatially distributed leaky bucket type of model, and is applied on a cell-by-cell basis. In order to minimize the number of input parameters, and avoid complexity and long model run-times, SPHY does not include energy balance calculations, and is therefore a water-balance based model. The main terrestrial hydrological processes are described in a physically consistent way so that changes in storages and fluxes can be assessed adequately over time and space. SPHY is written in the Python programming language using the PCRaster [*Karssenberg et al.*, 2001, 2010; *Karssenberg*, 2002] dynamic modelling framework.

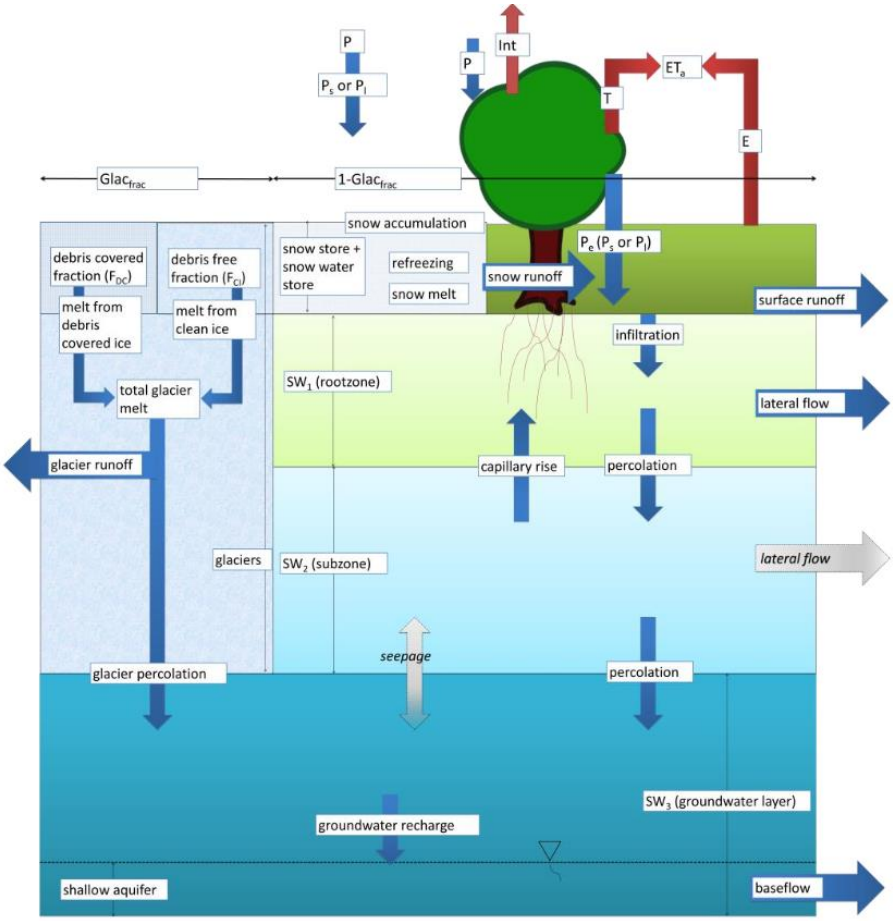


**Figure 24: SPHY model concepts [Terink et al., 2015].**

Figure 24 provides a schematic overview of the SPHY modeling concepts. SPHY is grid based and cell values represent averages over a cell. For glaciers, sub-grid variability is taken into account: a cell can be glacier free, partially glacierized, or completely covered by glaciers. The cell fraction not covered by glaciers consists of either land covered with snow or land that is free of snow. Land that is free of snow can consist of vegetation, bare soil, or open water.

The soil column structure is similar to VIC [*Liang et al.*, 1994, 1996], with two upper soil storages and a third groundwater storage. Their corresponding drainage components are



surface runoff, lateral flow and baseflow. SPHY simulates for each cell precipitation in the form of rain or snow, depending on the temperature. Precipitation that falls on land surfaces can be intercepted by vegetation and evaporated in part or whole. The snow storage is updated with snow accumulation and/or snowmelt. A part of the liquid precipitation is transformed in surface runoff, whereas the remainder infiltrates into the soil. The resulting soil moisture is subject to evapotranspiration, depending on the soil properties and fractional vegetation cover, while the remainder contributes to river discharge by means of lateral flow from the first soil layer, and baseflow from the groundwater layer.

Melting of glacier ice contributes to the river discharge by means of a slow and fast component, being (i) percolation to the groundwater layer that eventually becomes baseflow, and (ii) direct runoff. The cell-specific runoff, which becomes available for routing, is the sum of surface runoff, lateral flow, baseflow, snowmelt and glacier melt.

SPHY has been successfully applied in several studies in the Hindu Kush Himalayan region [*Lutz et al.*, 2012, 2014a, 2016a]. More details regarding the SPHY model can be found in *Terink et al.* [2015].

## 8.2 SPHY model glacier module concepts

In the current version of SPHY (2.1) glaciers are implemented as a fixed mass generating glacier melt using a degree day factor. In other words; glaciers remain constant in area and mass throughout the entire simulation period, while in reality glaciers disappear at a certain moment if ablation (melt) exceeds accumulation for a significant period of time. Additionally, the current version of SPHY does not account for precipitation falling onto the glacier, which can either fall as rain or snow. This means snowfall, accumulation and melt of snow is not accounted for.

For a valuable assessment of the potential for hydropower in the future, it is essential that glaciers are implemented as dynamic entities that can melt, redistribute ice, and disappear over time if ablation exceeds accumulation. Therefore, the glacier module in the current version of SPHY has been improved to account for:

- Precipitation falling on the glacier (rain or snow);
- Accumulation and melt of a dynamic snowpack on the glacier;
- Redistribution of ice from the accumulation to the ablation zone (Figure 25);
- Removal of glacier fraction if ice depth becomes zero.

These improvements are realized using a i) high-resolution DEM, ii) a map with glacier IDs (according to the Randolph Glacier Inventory v5.0 [*Pfeffer et al.*, 2014]), iii) initial ice thickness (Glaptop2 [*Frey et al.*, 2014; *Linsbauer et al.*, 2016]), and iv) the model grid domain. As a pre-processing step a glacier table is created that creates records with Unique IDs (UIDs); a unique combination of the model grid cell ID and glacier ID of a glacier that is located within that particular model grid cell. For that glacier ID fraction located within the model grid cell an average elevation is calculated using the high-resolution DEM. This allows for more accurate temperature estimations for that fraction, which eventually improves the calculation of snowfall and rainfall. The initial glacier volume for each UID is calculated by multiplying the glacier fraction with the cell area and initial ice depth. Each model time-step this table is updated using precipitation and temperature as input.

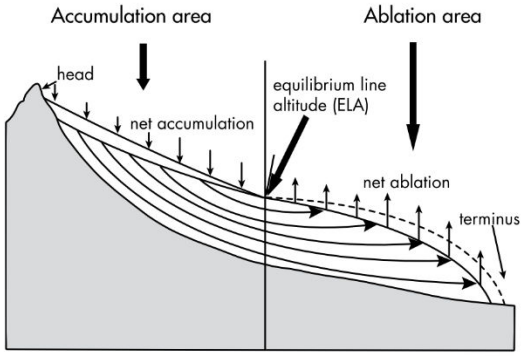


**Figure 25: Illustration of a glacier's accumulation and ablation area, and the Equilibrium Line Altitude (ELA) [Armstrong, 2010].**

Accumulated snow in the glacier's accumulation zone is transformed into ice and is distributed downstream towards the ablation area. This process of ice redistribution is implemented in SPHY by accumulating all melt and snow for each hydrological year and glacier, and calculate the difference. If this difference is negative, then a glacier is losing mass and ice from the ablation zone will be redistributed over the ablation zone according to the volume ice redistribution. This will be updated once a year, and is done at the end of the monsoon for the Tamakoshi River Basin.

## 8.3 Input data

As input, SPHY requires static data as well as dynamic data. For the static data, the most relevant are the Digital Elevation Model (DEM), land use type, glacier extents and ice depths, and soil characteristics. The DEM was obtained from HydroSHEDS[1]. GLOBCOVER2009 [*Bontemps et al.*, 2011] was used for the definition of land use classes. Hydrological soil properties were derived from HiHydroSoil [*De Boer*, 2015], which provides these properties on a spatial resolution of 1 km. Input data used for glaciers is described in the previous section.

For dynamic data SPHY requires gridded maps of daily precipitation and the average-, minimum-, and maximum daily temperature. For the reference climate period we use the bias-corrected HI-AWARE dataset, as described in Section 6.1 and 6.2. For the future climate we use an ensemble of 8 downscaled GCMs (Section 7.3).

## 8.4 Calibration

The SPHY model was calibrated using a two-step approach: first the model was calibrated to match the overall average glacier mass balance in this region, and secondly the model was calibrated to match the observed river discharge.

### *8.4.1 Glacier mass balance*

Several studies determined the mass balance of glaciers in the Hindu Kush Himalayan region [*Gardelle et al.*, 2013; *Kääb et al.*, 2015]. The Tamakoshi River Basin is located in the Everest region (Figure 26), and the average annual mass balance in this area is approx. -370 mm/year (Table 7). As a first step the SPHY model's glacier mass balance has been calibrated for the period 2001-2009 to match with the average observed mass balance of -370 mm/year. The year 2000 was used to initialize the model. Calibration was done manually by optimizing the degree

[1] http://www.hydrosheds.org/

day factor for clean ice (DDFG), the degree day factor for debris covered ice (DDFDG), the critical temperature for precipitation to fall as rain or snow (Tcrit), snow storage capacity for liquid water (SnowSc), and the degree day factor for snow (DDFS).

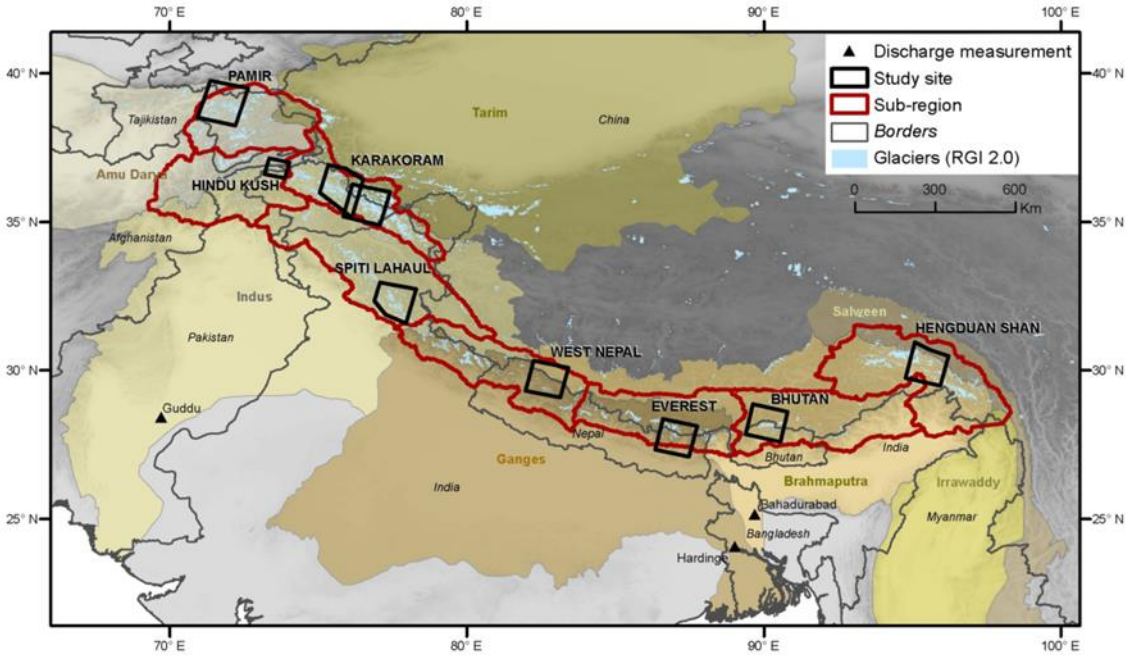


**Figure 26: Sites in the HKH region where geodetic mass balance data has been analyzed [Gardelle et al., 2013]. Everest is the site which is nearest to the Tamakoshi River Basin.**

**Table 7: Glacier elevation difference trends over the Pamir–Karakoram–Himalaya [Kääb et al., 2015].**

| Zone | Glacier area ($km^2$) | This study ($m\,yr^{-1}$, $\pm$ at $1\sigma$-level) | Gardner et al. (2013; $m\,yr^{-1}$, $\pm$ at $2\sigma$-level) | Neckel et al. (2014; $m\,yr^{-1}$, $\pm$ at $1\sigma$-level) | Gardelle et al. (2013; $m\,yr^{-1}$, $\pm$ at $1\sigma$-level) |
|---|---|---|---|---|---|
| Eastern Nyainqêntanglha[a] | 6000 | $-1.34 \pm 0.29$ | $-0.30 \pm 0.13$<br>$-0.40 \pm 0.41$[b] | $-0.81 \pm 0.32$ | $-0.39 \pm 0.16$ |
| Bhutan | 3500 | $-0.89 \pm 0.16$ | $-0.89 \pm 0.18$ | $-0.78 \pm 0.27$ | $-0.26 \pm 0.15$ |
| Everest | 8500 | $-0.37 \pm 0.10$ | $-0.44 \pm 0.20$ | | $-0.30 \pm 0.16$ |
| West Nepal | 7500 | $-0.43 \pm 0.09$ | | $-0.44 \pm 0.26$ | $-0.38 \pm 0.16$ |
| Spiti–Lahaul | 9500 | $-0.49 \pm 0.12$ | $-0.53 \pm 0.13$ | | $-0.53 \pm 0.16$ |
| Karakoram | 21 000 | $-0.10 \pm 0.06$ | $-0.12 \pm 0.15$ | | $+0.12 \pm 0.19$ |
| Hindu Kush | 5500 | $-0.49 \pm 0.10$ | | | $-0.14 \pm 0.19$ |
| Pamir | 6500 | $-0.48 \pm 0.14$ | $-0.13 \pm 0.22$ | | $+0.16 \pm 0.15$ |
| Western Kunlun Shan–Tarim | 12 500 | $+0.05 \pm 0.07$ | $+0.17 \pm 0.15$ | $+0.04 \pm 0.29$ | |
| Area-weighted mean | 80 500 | $-0.37 \pm 0.10$ | | | |

The area-average annual mass balance of all glaciers in the Tamakoshi River Basin was calibrated as -391 mm/year. This result is very close to the observed value of -370±0.10, and therefore satisfactory to be used in the remainder of this study. The calibrated model parameters are shown in Table 8. Figure 27 shows per hydrological year the area-weighted accumulation, melt, and change in mass for all glaciers in the Tamakoshi River Basin. It is clear that there is more melt than accumulation, and therefore the overall mass balance being negative. The area-averaged annual glacier mass balance with all fluxes is shown in Table 9.

**Table 8: Calibrated SPHY model glacier and snow parameters.**

| *Parameter* | *Calibrated value* | *Unit* |
|---|---|---|
| DDFG | 4 | mm °C$^{-1}$ day$^{-1}$ |
| DDFDG | 2 | mm °C$^{-1}$ day$^{-1}$ |
| Tcrit | 2 | °C |
| SnowSc | 0.5 | - |
| DDFS | 5.5 | mm °C$^{-1}$ day$^{-1}$ |

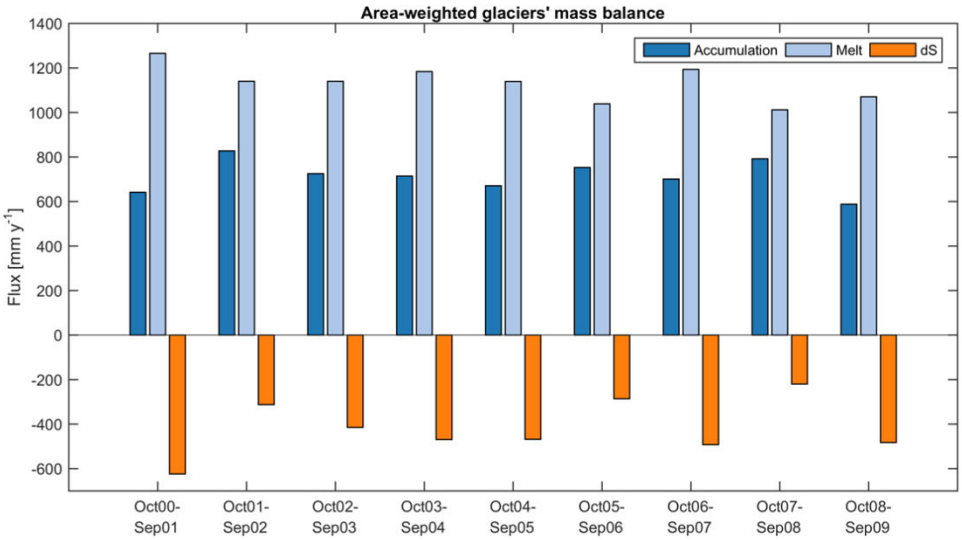


**Figure 27: Calibrated area-weighted mass balance of all glaciers in the Tamakoshi River Basin for the period 2000-2009. For each hydrological year the total accumulation, melt, and change in mass (dS) is shown.**

**Table 9: Area-averaged annual fluxes from all glaciers in the Tamakoshi River Basin.**

| *Flux* | *mm year$^{-1}$* |
|---|---|
| Precipitation | 2070 |
| Rain | 977 |
| Snow | 1093 |
| Snow melt | 522 |
| Snow runoff | 581 |
| Glacier melt | 1141 |
| Glacier runoff | 1047 |
| Glacier percolation | 864 |

### *8.4.2 Discharge*

Observed daily discharge for the period 2001-2009 was available for two stations, being Busti (ID 647) and Rasnalu (ID 650). The locations of these stations are shown in Figure 28, and are in proximity of the Hydropower plants Tamkoshi-III and Khimti. Therefore, if calibration is successful, then also the simulated discharge for these hydropower plants is accurate.



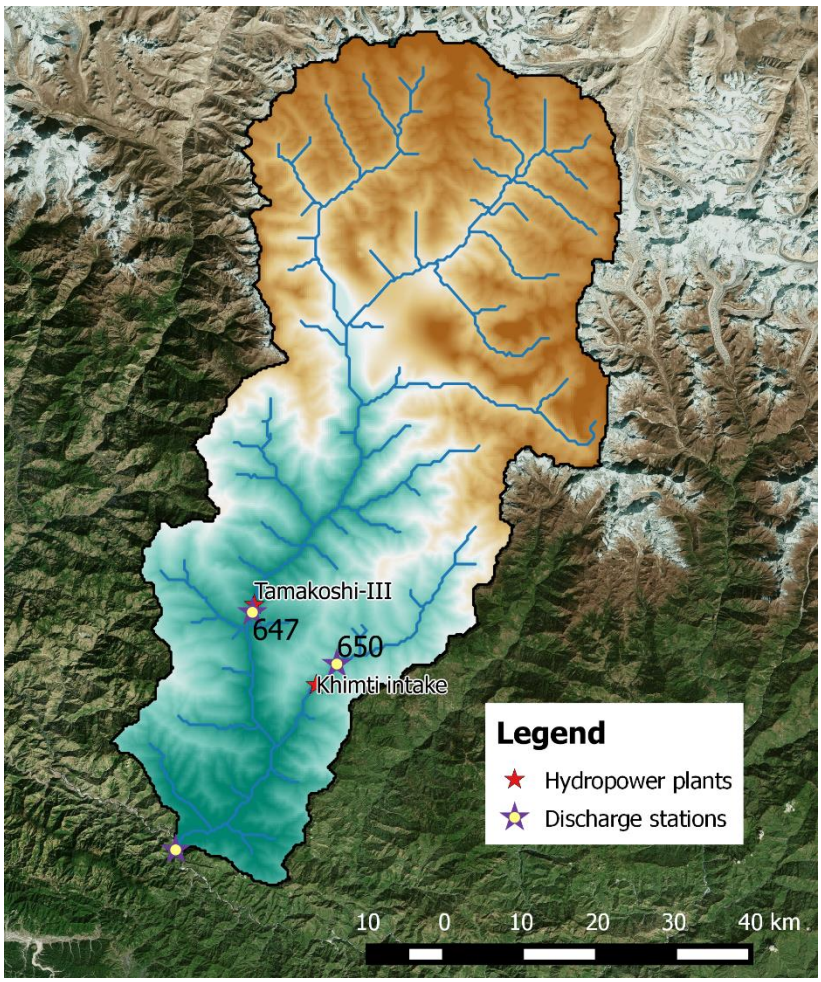


**Figure 28: Location of discharge stations Busti (ID 647) and Rasnalu (ID 650).**

**Table 10: Average annual water balance for the upstream areas of Busti and Rasnalu.**

| *Flux* | *Busti (ID 647)* *[mm year$^{-1}$]* | *Rasnalu (ID 650)* *[mm year$^{-1}$]* |
|---|---|---|
| Precipitation | 2100 | 2759 |
| Evapotranspiration | 339 | 732 |
| Discharge | 1410 | 1864 |

River discharge is calibrated for the period 2001-2009, using the year 2000 as initialization period. The following five model parameters were selected for calibration:

- alphaGW
- deltaGW
- glacF
- kx

Additionally, a fractional map is calibrated that adjust the saturated hydraulic conductivity (Ksat) of the root- and subzone soil layers. Calibration was done using the automatic calibration package SPOTPY [*Houska et al.*, 2015], using the Maximum Likelihood Estimation (MLE) optimization algorithm to minimize the Mean Squared Error between the observed and simulated streamflow . SPHY was calibrated for station ID 647, and validated for ID 650.

Figure 29 and Figure 30 show the hydrographs of calibrated vs. observed daily discharge for Busti and Rasnalu station, respectively. The Nash-Sutcliffe [*Nash and Sutcliffe*, 1970] and bias model performance indicators are shown as well. The Nash-Sutcliffe efficiency (NS) can range from $-\infty$ to 1. An efficiency of 1 corresponds to a perfect match of modeled discharge to the observed data. An efficiency of 0 indicates that the model predictions are as accurate as the mean of the observed data, whereas an efficiency less than zero occurs when the observed mean is a better predictor than the model. Essentially, the closer the model efficiency is to 1, the more accurate the model is. The bias is defined as the difference between the average simulated and average observed discharge. It is preferred to have a bias that is close to 0. Positive biases indicate overestimated discharge, while negative biases indicate underestimated discharge.

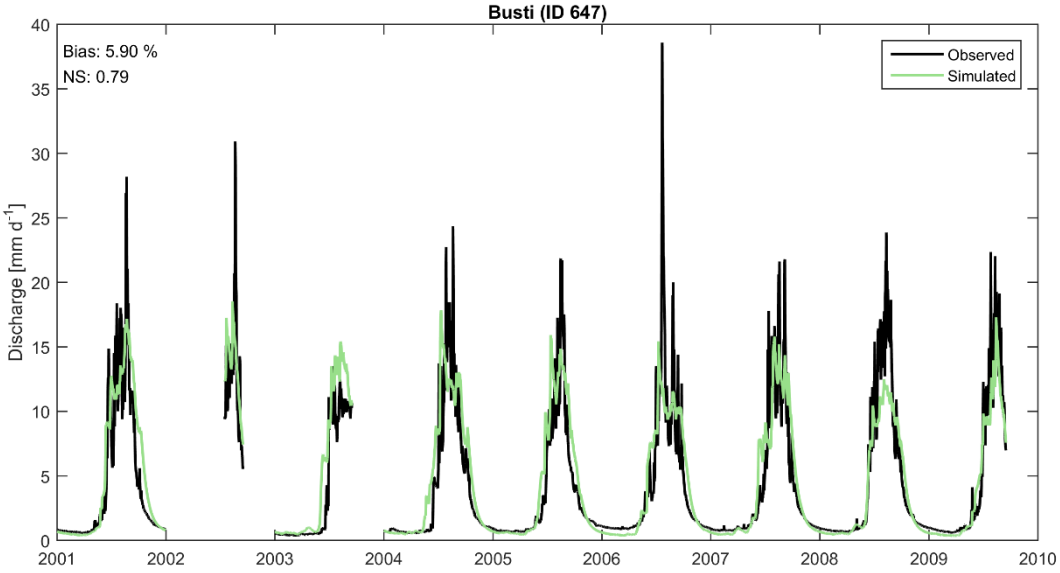


**Figure 29: Hydrograph of calibrated vs. observed daily discharge for Busti station (ID 647). Missing values in 2002 and 2003 are not taken into account.**

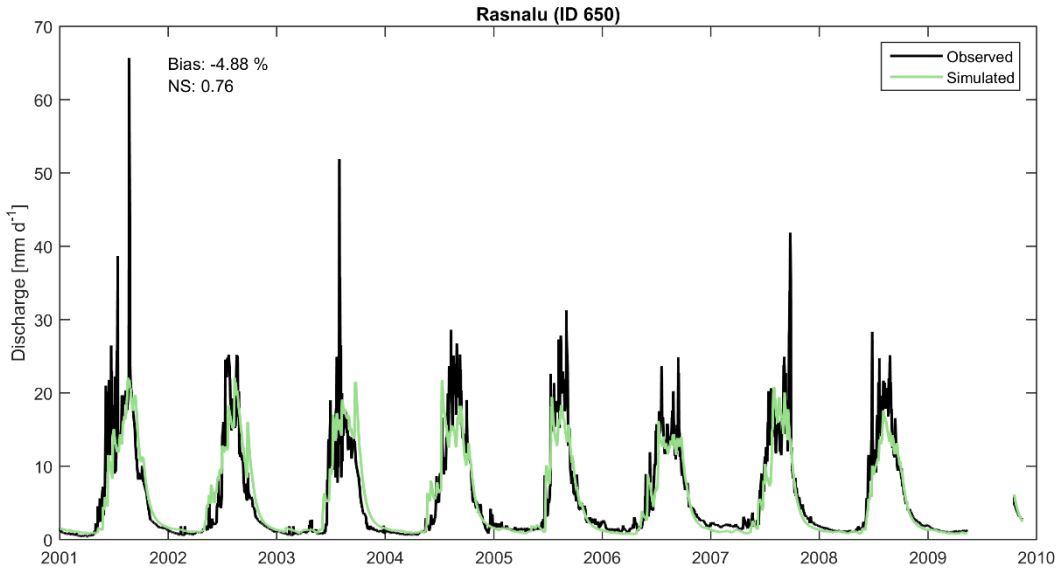


**Figure 30: Hydrograph of validated vs. observed daily discharge for Rasnalu station (ID 650). Missing values in 2009 are not taken into account.**



With NS-efficiencies of 0.79 and 0.76, and biases of 5.90% and -4.88% for Busti and Rasnalu, respectively, it can be concluded that the SPHY model is calibrated very satisfactory. It is clear that the model underestimates the extreme peak flows. There may be several reasons for the underestimation of high peak flows. First, according to DHM, who collects and manages these datasets (Table 11), the quality of the discharge data of the two stations are classified as 'Fair', which suggest that the observed data might have some issues related to the physical condition and/or the location of the discharge measurement. Second, because of the discharge rating curves (which changes over time), there are large uncertainties in the estimation of high peak flows.

**Table 11: Discharge station quality [http://www.dhm.gov.np/hydrological-station/].**

| *Station no.* | *Name* | *Elevation [MASL]* | *Drainage area [km$^2$]* | *Quality* |
|---|---|---|---|---|
| 647 | Busti | 849 | 2753 | Fair |
| 650 | Rasnalu | 1120 | 313 | Fair |

The section above evaluated the model performance on a daily basis. For Hydropower generation, however, it is also relevant to evaluate the model's performance on a monthly time-scale. Hydrographs of calibrated vs. observed monthly discharge are shown in Figure 31 and Figure 32 for Busti and Rasnalu, respectively. Based on these hydrographs it can be concluded that monthly performance is even better as daily model performance, and that the model is suitable to evaluate the impacts of climate change on Hydropower potential for Tamakoshi-III and Khimti.

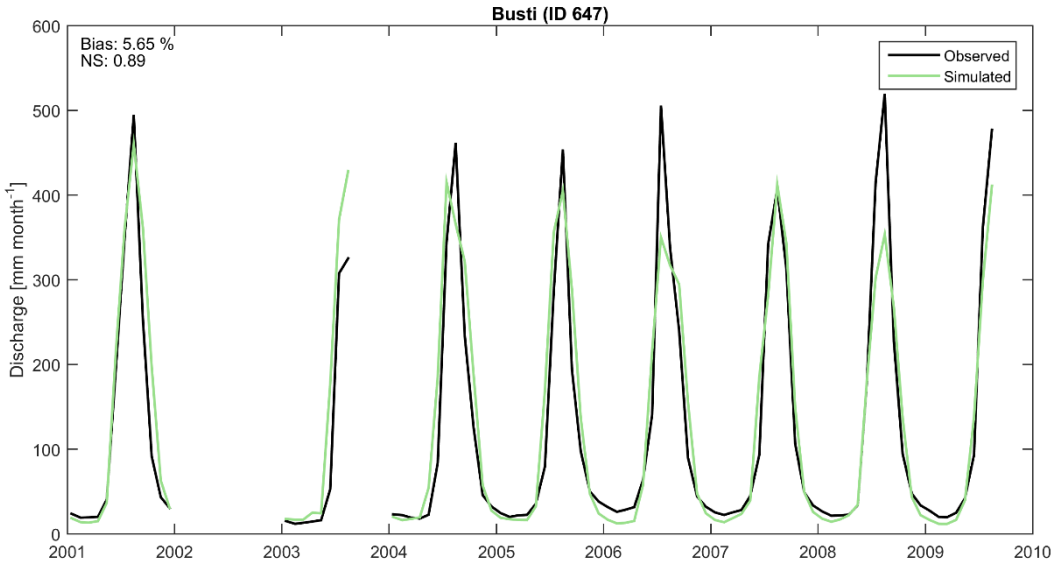


**Figure 31: Hydrograph of calibrated vs. observed monthly discharge for Busti station (ID 647). Missing values in 2002 and 2003 are not taken into account.**

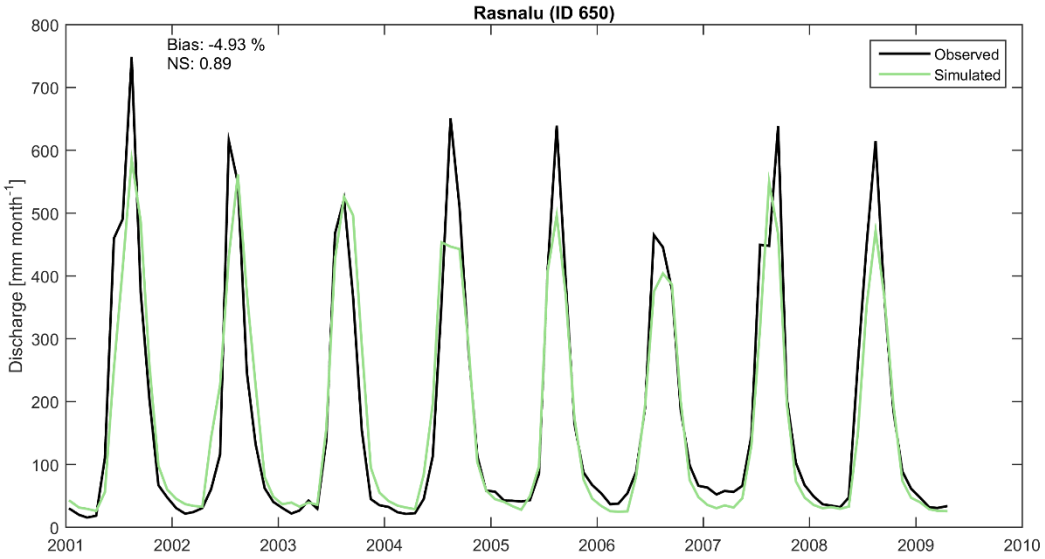


**Figure 32: Hydrograph of validated vs. observed monthly discharge for Rasnalu station (ID 650). Missing values in 2009 are not taken into account.**

# 9 Hydrological impacts of climate change

## 9.1 Basin wide impacts

### *9.1.1 Spatial patterns of precipitation and temperature*

Figure 33 shows the spatial changes in precipitation and temperature for the two future periods 2016-2045 and 2046-2075 (referred to as P1 and P2 hereafter) with respect to the reference climate 1981-2010. Changes are calculated based on the average signal of the 4 RCP4.5 GCMs. For P1 we can expect an increase in annual precipitation of 2-3%, while this increase is estimated to be 12% for P2. Average annual temperatures are expected to increase with 0.5-1 °C for P1, and 1.4-2 °C for P2. For temperature the increase is more evident in the southern part of the basin. This is likely related to another GCM grid cell that is used for the lower part.

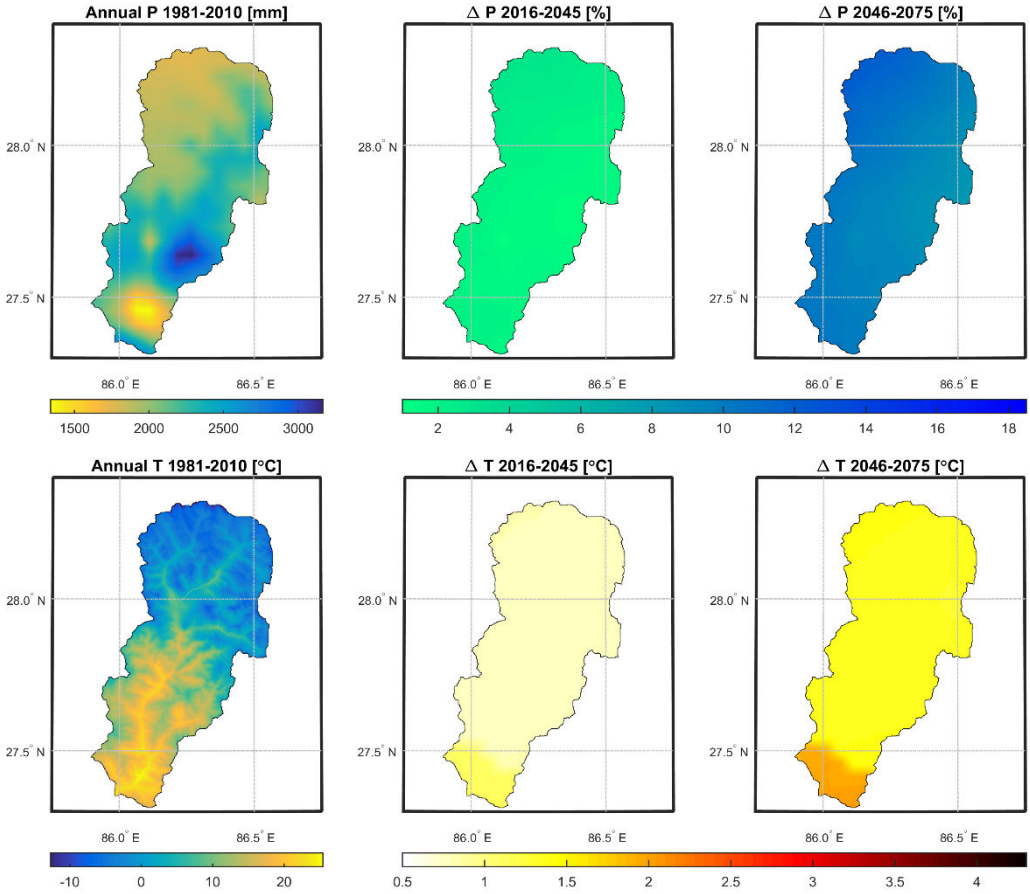


**Figure 33: Top (from left to right): average annual precipitation (P) for the reference climate, and the change in annual precipitation (%) for 2016-2045 (P1) and 2046-2075 (P2), both averaged over the 4 RCP4.5 GCMs. Bottom (from left to right): average annual temperature (T) for the reference climate, and the change in annual temperature (°C) for 2016-2045 and 2046-2075, both averaged over the 4 RCP4.5 GCMs.**

Figure 33 calculated the difference based on the average signal of the 4 RCP4.5 GCMs. In each GCM, the physics of the atmosphere are represented differently, and therefore each GCM produces a different precipitation and temperature signal. Figure 34 shows the standard deviation (δ) of the 4 RCP4.5 GCMs for the annual precipitation (top) and annual temperature (bottom) for P1 and P2. This can be interpreted as the uncertainty in the future estimates for

precipitation and temperature. It is clear that the variation in annual precipitation between the GCMs can range between 70 and 160 mm for P1, and 90-200 mm for P2, with the largest uncertainties in the southeastern part of the basin. Logically, this range is broader for P2 because the far future is more uncertain than the nearby future. Standard deviations of average annual temperature for the RCP4.5 GCMs ranges between 0.25-0.45 °C for P1, and 0.5-0.75 for P2., indicating a more uncertain 2046-2075 period.

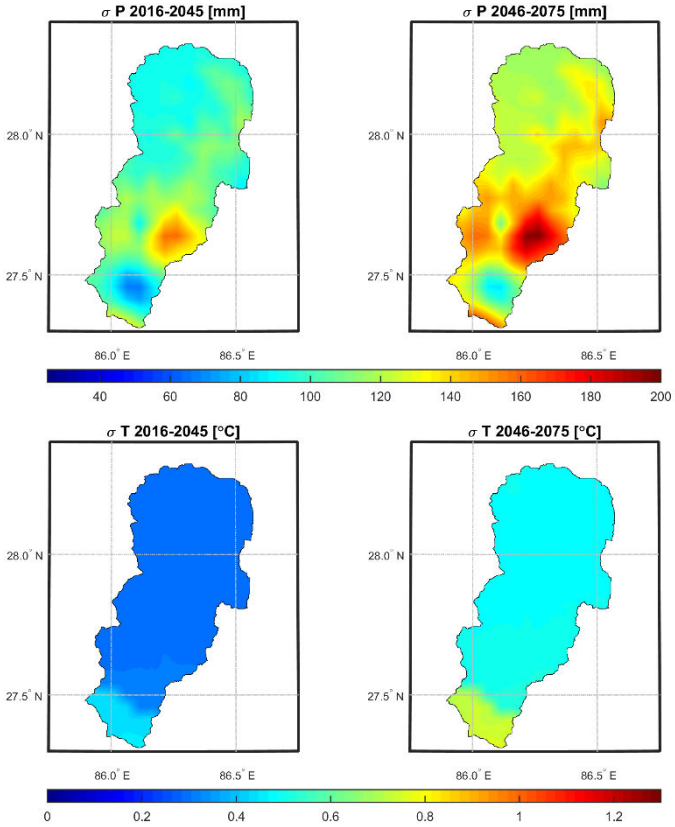


**Figure 34: Top: standard deviations of the 4 RCP4.5 average annual precipitation sums for the two future periods. Bottom: same, but then for average annual temperature.**

Similar analyses have been conducted for the RCP8.5 GCMs, which are based on a higher radiative forcing pathway [*van Vuuren et al.*, 2011]. Figure 35 shows the spatial changes in precipitation and temperature for P1 and P2, based on the RCP8.5 GCMs. Compared to the changes based on the RCP4.5 GCMs (Figure 33), it is clear that changes in average annual precipitation and temperature are larger for the RCP8.5 GCMs. For 2016-2045 it is expected that the average annual precipitation increases with 5.5-8%, while this is 14-18.5% for 2046-2075. Temperature is expected to increase with 0.8-1.4 °C for 2016-2045, and with 2.2-2.9 °C for 2046-2075.

Similar as done for RCP4.5, Figure 36 shows the standard deviation (δ) of the 4 RCP8.5 GCMs for the annual precipitation (top) and temperature (bottom) for P1 and P2. Standard deviations of annual precipitation for the RCP8.5 GCMs range between 25 and 70 mm for P1, and 70-135 mm for P2. Again these uncertainties are larger for the far future, but smaller compared to the uncertainties found for the RCP4.5 GCMs. For temperature the RCP8.5 GCMs are more uncertain, with standard deviations ranging between 0.38 and 0.62 °C for P1, and 0.68 and 1.05 °C for P2.



To take these uncertainties into account, this study evaluates the impact of climate change by analyzing the average, minimum, and maximum of GCM signals for both RCP4.5 and RCP8.5. This provides us with the broadest range of discharge possibilities for the future.

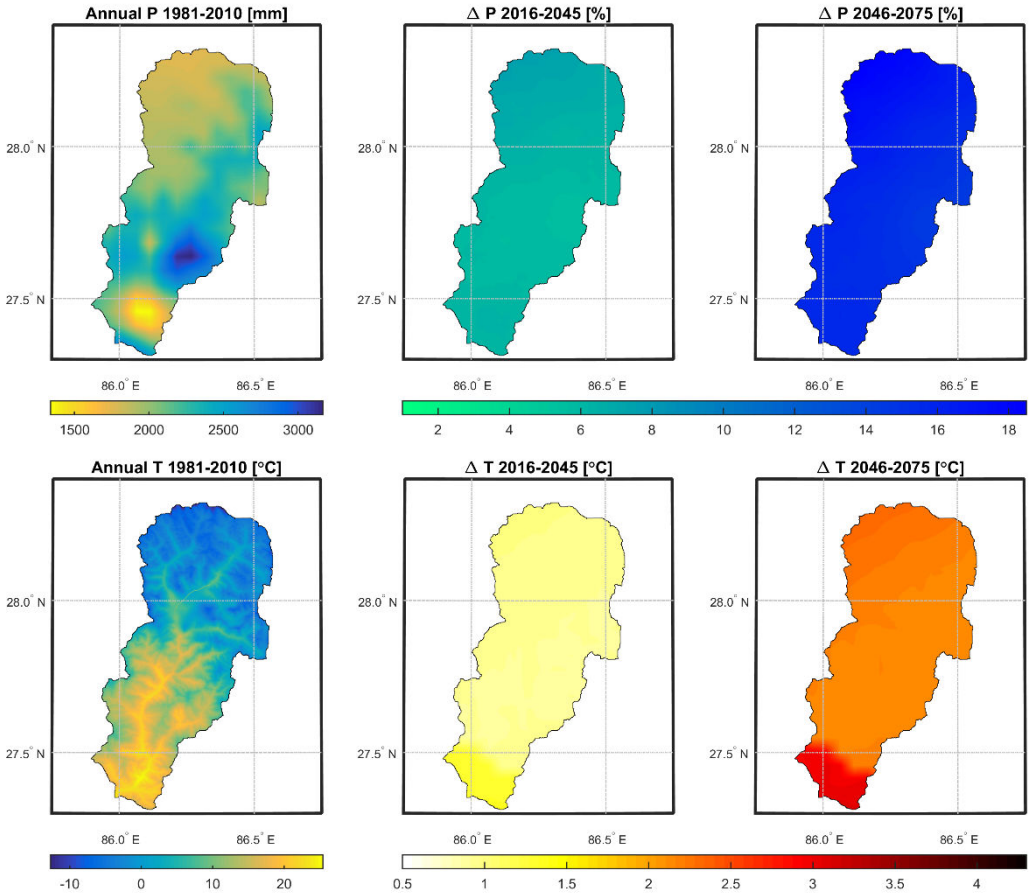


**Figure 35: Top (from left to right): average annual precipitation (P) for the reference climate, and the change in annual precipitation (%) for 2016-2045 (P1) and 2046-2075 (P2), both averaged over the 4 RCP8.5 GCMs. Bottom (from left to right): average annual temperature (T) for the reference climate, and the change in annual temperature (°C) for 2016-2045 and 2046-2075, both averaged over the 4 RCP8.5 GCMs.**

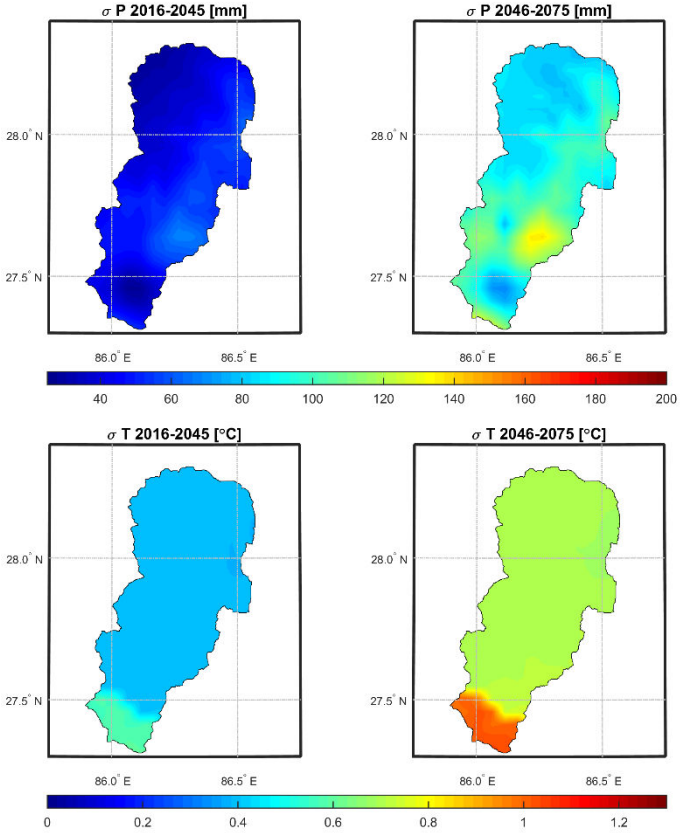


**Figure 36: Top: standard deviations of the 4 RCP8.5 average annual precipitation sums for the two future periods. Bottom: same, but then for average annual temperature.**

### *9.1.2 Annual time-series*

Figure 37 shows the basin average annual precipitation for the reference climate (1981-2010) and the future climate (2016-2075), as represented by four RCP4.5 GCMs. Currently, precipitation ranges between 1800 and 2500 mm per year. All four RCP4.5 GCMs show an increasing trend in annual precipitation. Annual precipitation sums ≥3000 mm are not unlikely. At the same time, we can also expect some years with less precipitation (1500 mm).

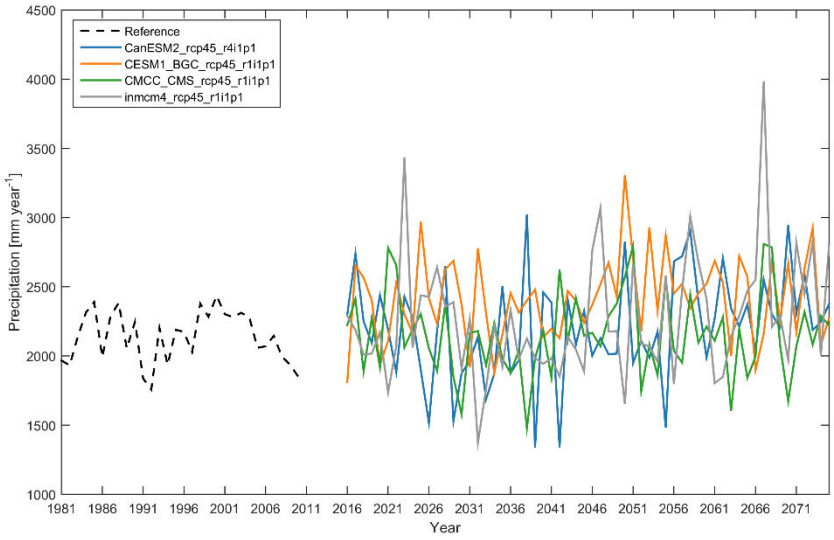


**Figure 37: Basin average annual precipitation sums for reference climate and 4 RCP4.5 GCMs.**

For RCP8.5 the increase in annual precipitation Figure 38is even more evident than for RCP4.5. Figure 38 shows a clear increasing trend for all RCP8.5 GCMs in annual precipitation. Based on these projections we may expect annual precipitation to reach 3000 mm during 2016-2045, and even larger sums are expected during 2046-2075. The most extreme case is shown by CanESM2_rcp85_r4i1p1, with approx. 4000 mm year$^{-1}$ near the end of 2046-2075. Compared to RCP4.5, we notice a lower frequency in years with precipitation ranging between 1500-2000 mm.

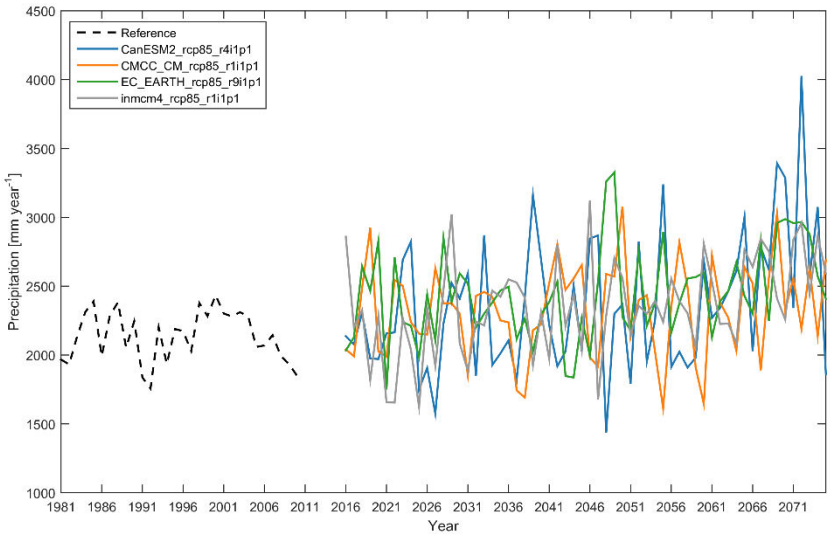


**Figure 38: Basin average annual precipitation sums for reference climate and 4 RCP8.5 GCMs.**

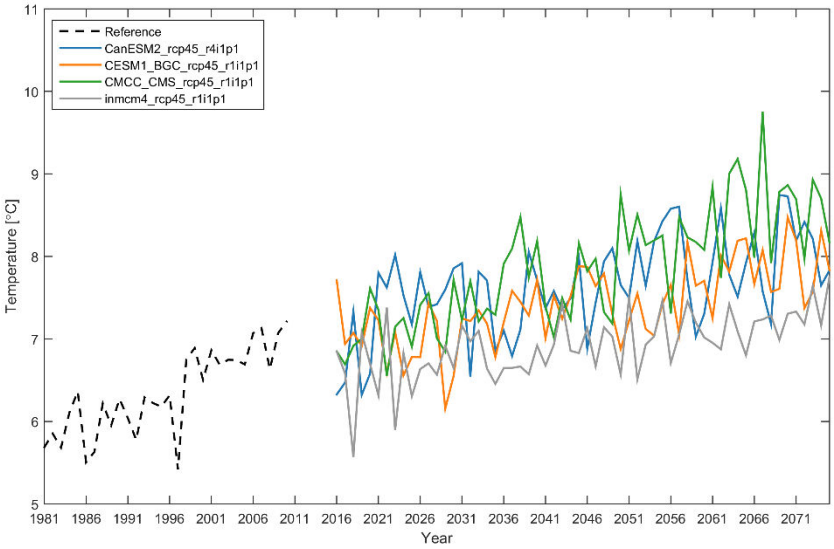


**Figure 39: Basin average annual temperature for reference climate and 4 RCP4.5 GCMs.**

Basin average annual temperature projections for the reference climate and future climate, as represented by the four RCP4.5 GCMs, is shown in Figure 39. The reference period already shows an increasing trend in annual temperature, with annual temperatures ranging between 5.5 and 7°C. This trend continues to increase during the period 2016-2075. The average temperature during the period 1981-2010 is approx. 6.5°C, and is projected to be 7.0°C on average for 2016-2046. For 2046-2075 the average annual temperature of the 4 GCMs is approx. 8°C, which is an increase of 1.5°C with respect to the period 1981-2010.

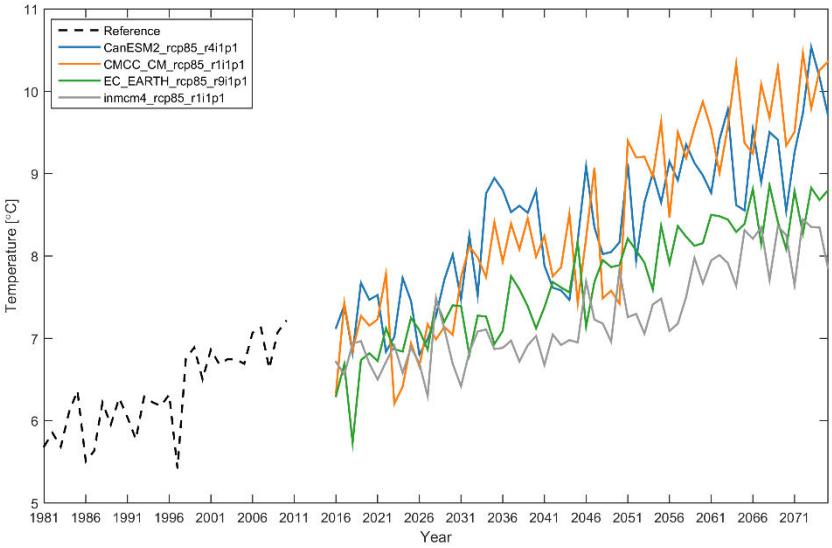


**Figure 40: Basin average annual temperature for reference climate and 4 RCP8.5 GCMs.**

Similar as for RCP4.5, Figure 40 shows the basin average annual temperature projections for the four RCP8.5 GCMs. It is clear that a stronger temperature increase is projected for RCP8.5, with an average annual temperature of approx. 7.5 °C for 2016-2045, and 8.5°C for 2046-2075. The latter period is therefore projected to be approx. 2°C warmer compared to the reference period. The range in temperature projections between the RCP8.5 GCMs is larger than those for RCP4.5. This range can be more than 2°C, meaning that the uncertainty in temperature projections is quite uncertain. These higher temperatures will affect snow- and glacier melt substantially.

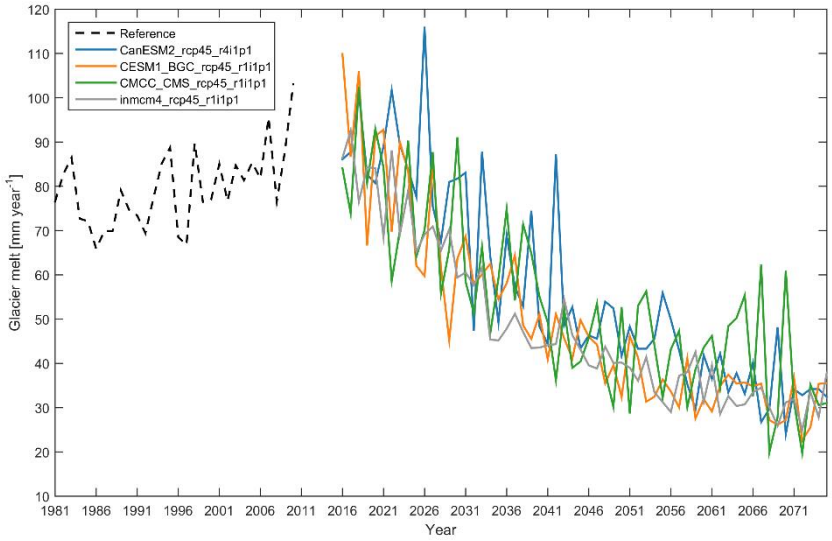


**Figure 41: Basin average glacier melt for reference climate and 4 RCP4.5 GCMs.**

Figure 41 shows the basin average annual glacier melt as modelled by the SPHY model for the reference climate and future climate, using the four RCP4.5 GCM projections of precipitation and temperature. Average annual glacier melt for the reference climate is approx. 80 mm year$^{-1}$, and ranges between 65 and 100 mm year$^{-1}$. The projected increase in temperature for 2016-2045 (Figure 39) results in an increased melt rate from glaciers, leading to a gradual retreat of these glaciers, and eventually the disappearance of those glaciers. With the glaciers retreating,



less glacier surface area is available for melting, which explains the decrease in glacier melt for 2016-2045. This decrease is strongest during 2016-2045.

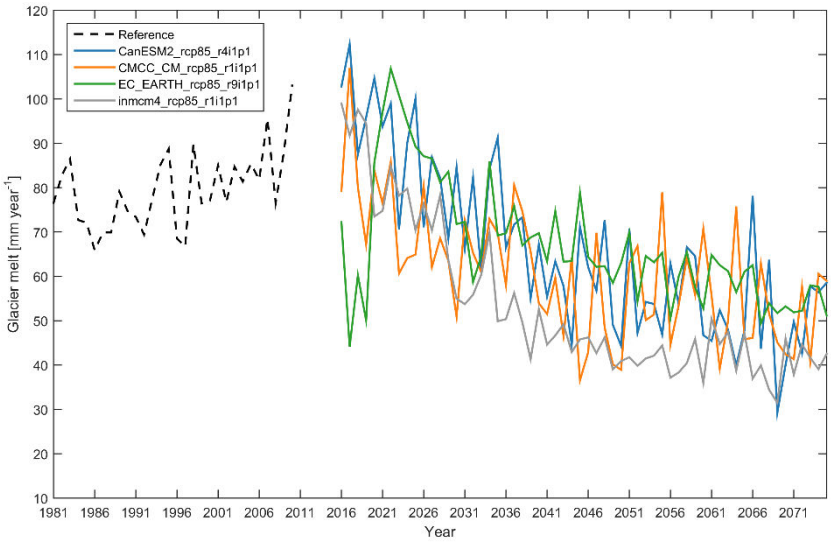


**Figure 42: Basin average glacier melt for reference climate and 4 RCP8.5 GCMs.**

Glacier melt as modelled by the SPHY model for the reference climate and the future climate, using the four RCP8.5 GCM projections of precipitation and temperature as input, is shown in Figure 42. Also for the RCP8.5 projections average annual glacier melt is expected to decrease. However, this decrease in melt is smaller compared to that of RCP4.5. This is related to the fact that RCP8.5 temperature projections are higher, resulting in a higher melting rate. This significantly affects the glaciers in the higher elevation areas, where ice depths are much larger compared to those in the lower elevation areas. Because of these larger ice depths, the percentual loss in volume is much larger compared to the loss in area for these high-elevation glaciers. In other words; the higher RCP8.5 temperature projections, and thus higher melting rates, especially reduce the glacier volume instead of glacier surface area in these regions, which explains the higher glacier melt around 2075 for the RPC8.5 projections. Additionally, the higher precipitation projections for RCP8.5 may lead to more snowfall in these higher elevated areas, which can contribute to a slight increase in glacier mass in those areas.

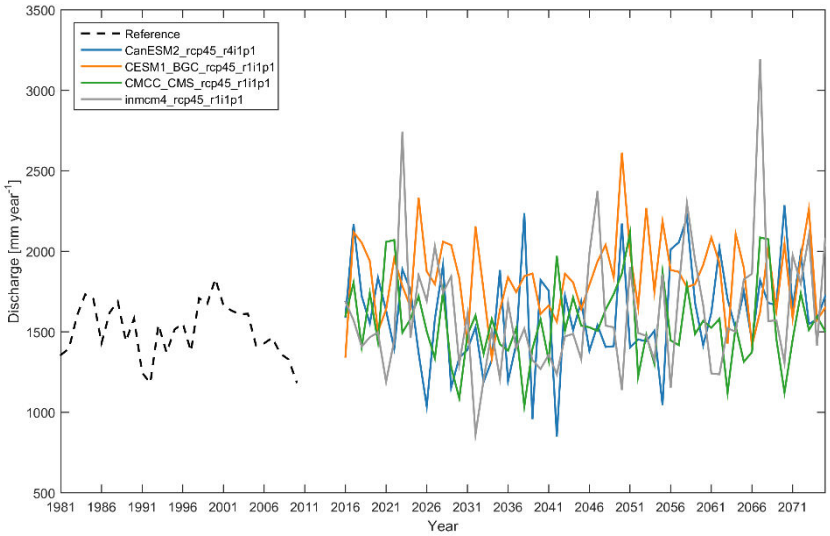


**Figure 43: Basin average discharge for reference climate and 4 RCP4.5 GCMs.**

The projected increase in both precipitation (Figure 37 and Figure 38) and temperature (Figure 39 and Figure 40) will result in an increase in river discharge. This is shown in Figure 43, with the basin average discharge for the reference climate and future period, based on the four RCP4.5 GCM projections. For the reference period, the basin average annual discharge fluctuates around 1500 mm year$^{-1}$. The expected average annual discharge for 2016-2075 is approx. 1700 mm year$^{-1}$, and can vary between 1000 and 2500 mm year$^{-1}$ with exceptions of more than 2500 mm year$^{-1}$. Discharges are highest for inmcm4_rcp45_r1i1p1, which is related to the higher precipitation projections of this GCM.

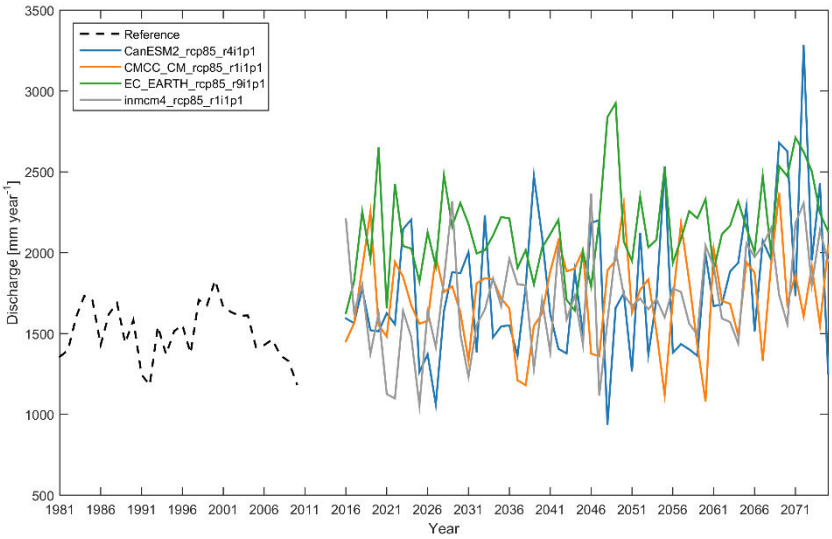


**Figure 44: Basin average discharge for reference climate and 4 RCP8.5 GCMs.**

With the higher precipitation and temperature projections of the RCP8.5 GCMs, it is logical that also the basin average annual discharge is higher for these GCMs, which is shown in Figure 44. Based on the RCP8.5 GCMs, the expected basin average annual discharge for 2016-2075 is approx. 1900 mm year$^{-1}$, and the frequency of years with discharge >2000 mm year$^{-1}$ is higher compared to that of the RCP4.5.

### *9.1.3 Monthly changes*

Changes in precipitation are also assessed on a monthly basis (Figure 45). It can be seen that the increase in precipitation is most evident during the monsoon, especially during July-August. Currently, the average monthly precipitation for July-August is 550 mm month$^{-1}$. For 2016-2045 this may increase to 650 mm month$^{-1}$, while this can reach 700 mm month$^{-1}$ during 2046-2075. It is also indicated that it is not unlikely that we may expect less precipitation during July-August, especially during P1.

Figure 46 shows the change in average monthly temperature for the reference climate and the periods 2016-2045 and 2046-2075. As shown earlier, both periods show an increase in basin average temperature, with the largest increase expected during 2046-2075. Temperature increases are largest during the winter and monsoon months, which is especially true for 2046-2075. For 2046-2075, an increase of 2-3 °C is not unlikely during the winter and monsoon months. This inevitably will lead to more precipitation to fall as rain instead of snow.



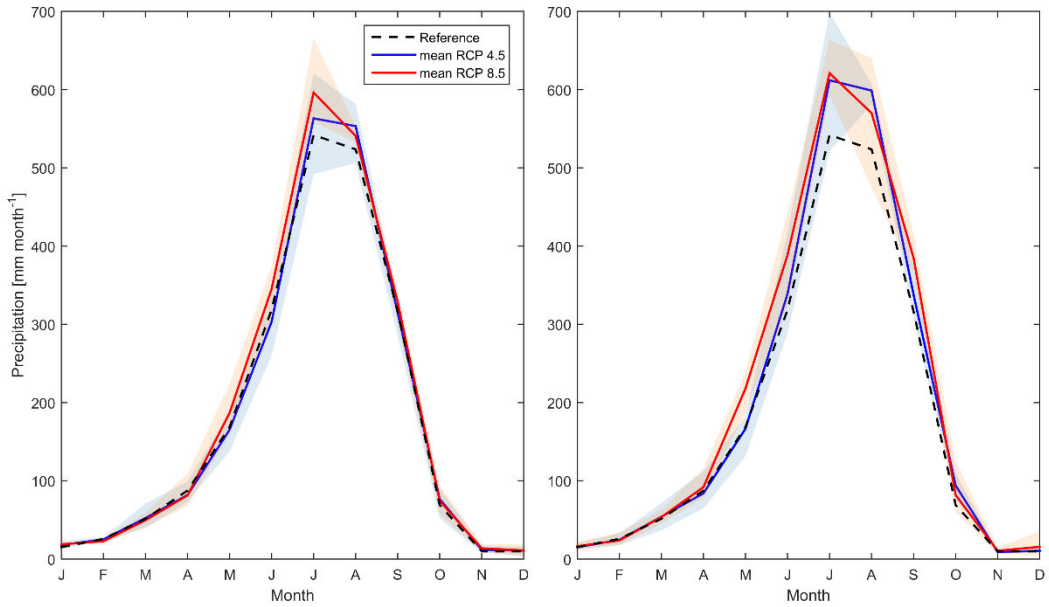


**Figure 45: Left: basin average monthly precipitation for the reference climate, and the 2016-2045 period for the average of the RCP4.5 GCMs and RCP8.5 GCMs, respectively. Blue and red bands represent the range between the maximum and minimum of GCM projections for RCP4.5 and RCP8.5. Right: idem, but for the 2046-2075 period.**

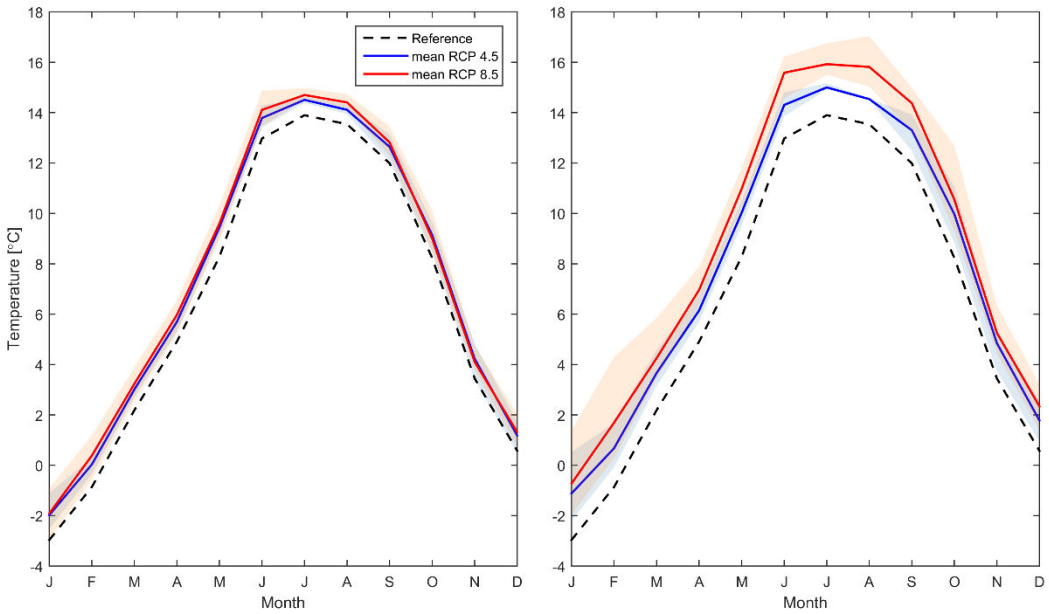


**Figure 46: Left: basin average monthly temperature for the reference climate, and the 2016-2045 period for the average of the RCP4.5 GCMs and RCP8.5 GCMs, respectively. Blue and red bands represent the range between the maximum and minimum of GCM projections for RCP4.5 and RCP8.5. Right: idem, but for the 2046-2075 period.**

Figure 47 shows the change in average monthly glacier melt for the reference climate and the periods 2016-2045 and 2046-2075. Due to increased temperatures, glaciers gradually retreat and as a result contribute to a lesser extent to the total river discharge. Because of the retreating glaciers, melt from glaciers is smaller for both future periods, especially for 2046-2075. On average, glacier melt during July-August decreases from 23 to 19 mm month$^{-1}$ for 2016-2045, and to 12 mm month$^{-1}$ for 2046-2075, which is almost half of what is generated during the reference period.

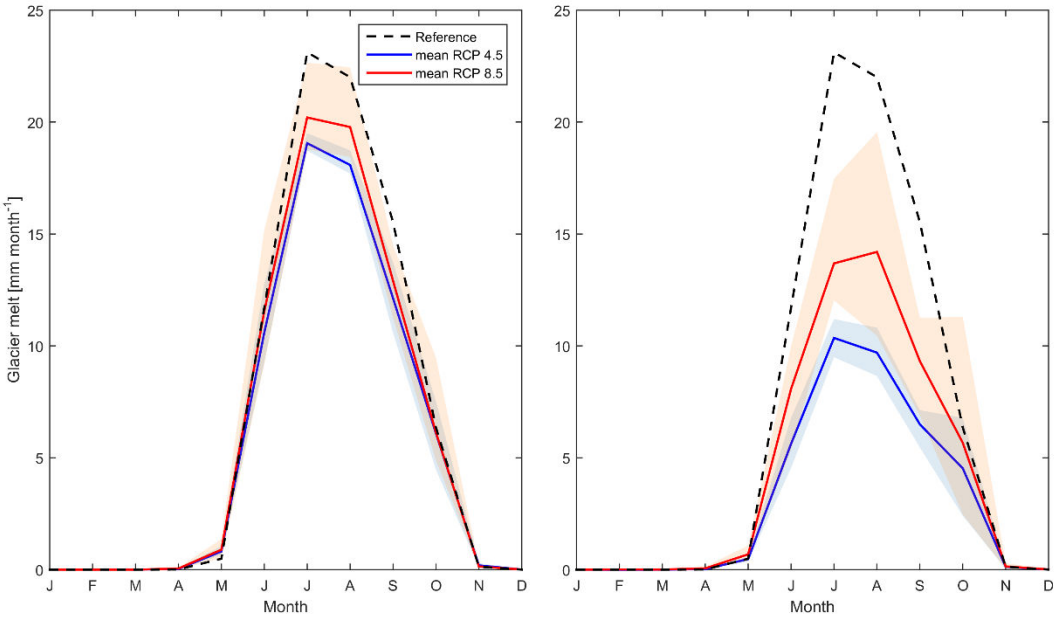


**Figure 47: Left: basin average monthly glacier melt for the reference climate, and the 2016-2045 period for the average of the RCP4.5 GCMs and RCP8.5 GCMs, respectively. Blue and red bands represent the range between the maximum and minimum of GCM projections for RCP4.5 and RCP8.5. Right: idem, but for the 2046-2075 period.**

However, considering the monthly discharge volumes (Figure 48), the contribution of glacier melt to the total flow is minor (6% for the reference climate). The higher temperatures result in more precipitation falling as rain instead of snow, which causes an increase in river discharge during the first few months of the year. The increase in precipitation during the monsoon causes the river discharge to increase during 2016-2045 and 2046-2075. For August the average discharge may increase from approx. 375 to 475 mm month$^{-1}$ for P1, and to 500 mm month$^{-1}$ for P2. During October-December no substantial changes in river discharge are expected.

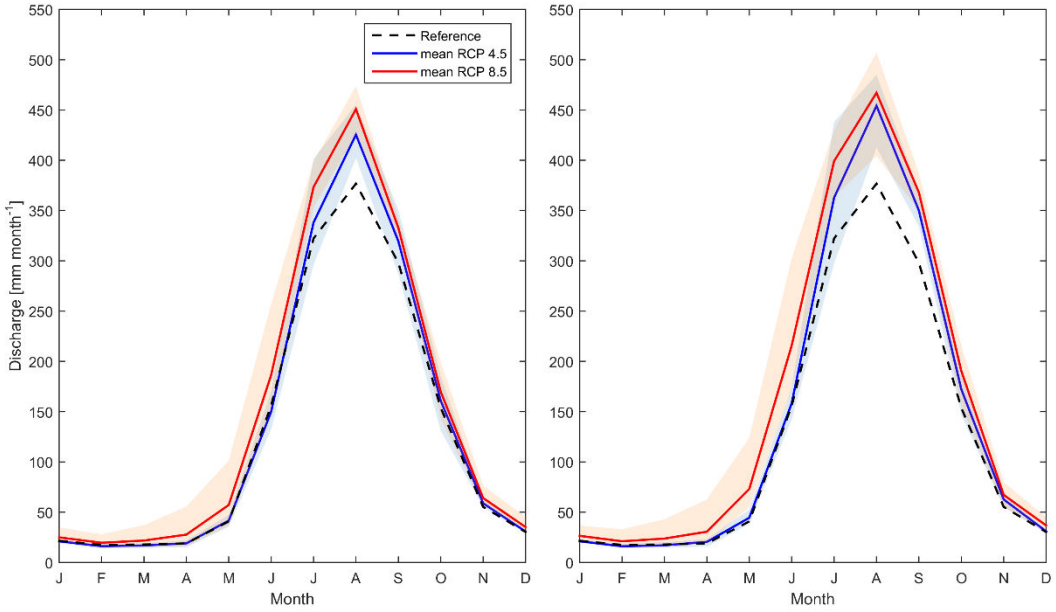


**Figure 48: Left: basin average monthly discharge for the reference climate, and the 2016-2045 period for the average of the RCP4.5 GCMs and RCP8.5 GCMs, respectively. Blue**



**and red bands represent the range between the maximum and minimum of GCM projections for RCP4.5 and RCP8.5. Right: idem, but for the 2046-2075 period.**

## 9.2 Tamakoshi-III

### *9.2.1 Annual time-series of discharge*

Figure 49 and Figure 50 show the average annual discharge for the periods 1981-2010 and 2016-2075 for Tamakoshi-III. The expected discharge simulated using the RCP4.5 GCMs as input is shown in Figure 49, while the expected discharge using the RCP8.5 GCMs as input is shown in Figure 50.

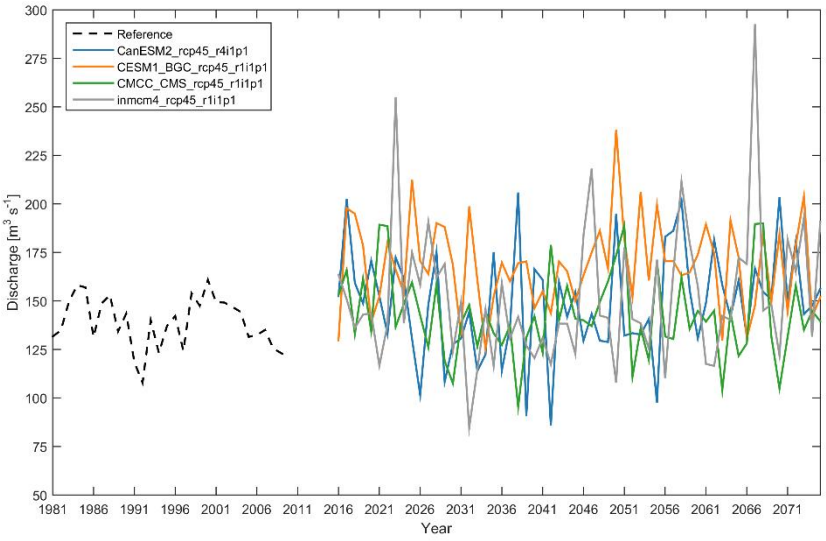


**Figure 49: Average annual discharge for Tamakoshi-III for the reference climate and 4 RCP4.5 GCMs.**

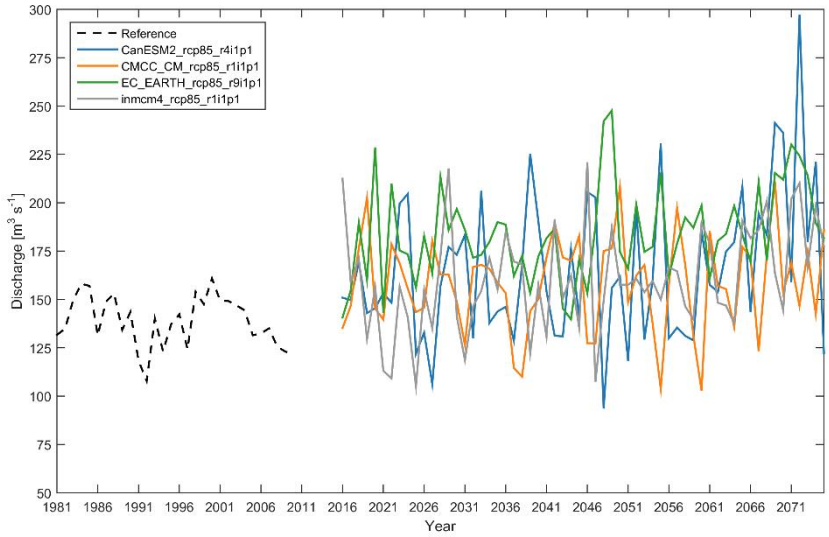


**Figure 50: Average annual discharge for Tamakoshi-III for the reference climate and 4 RCP8.5 GCMs.**

As a result of increased precipitation and temperature, an increase in discharge is expected for the period 2016-2075. The average annual discharge for Tamakoshi-III ranges between 100 and 165 $m^3/s$ for the reference period. As a result of climate change, using the RCP4.5 GCM

projections, we may expect the average annual discharge for 2016-2075 to vary between 100-200 $m^3/s$. Years with more than 200 $m^3/s$ are not unlikely. The stronger increase in precipitation and temperature, as projected by the RCP8.5 GCMs, leads to higher discharge expectations for 2016-2075, ranging between 125-225 $m^3/s$.

### *9.2.2 Monthly changes*

The total discharge as simulated by the SPHY model consists of four components, being baseflow, glacier runoff, snow runoff, and rain runoff. The contribution of each of these flow components to the total discharge at Tamakoshi-III is shown in Figure 51 for the reference period (1981-2010), and the two future periods 2016-2045 and 2046-2075. For the reference period, the annual contribution of these flow components to the total flow is 7-8% for glacier runoff, 18-19% for snow runoff, 12-13% for baseflow runoff, and 61-62% for rainfall runoff.

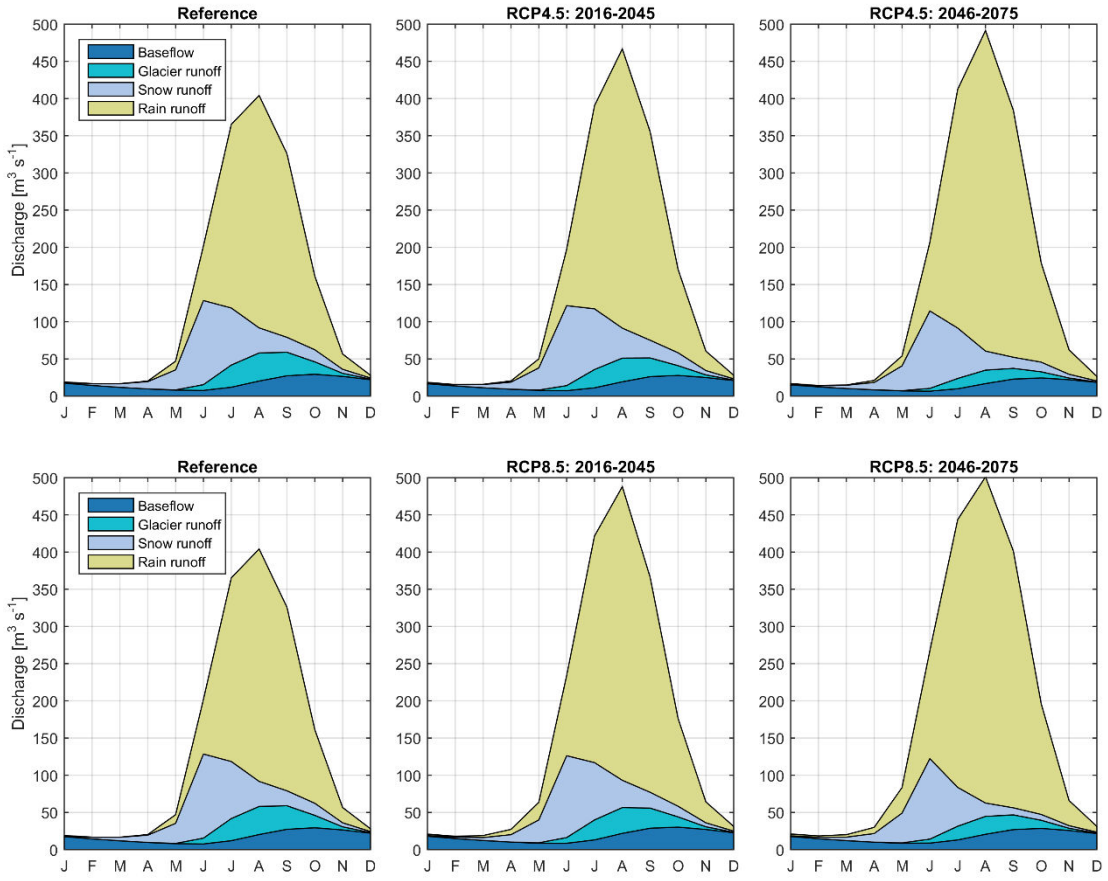


**Figure 51: Top: average monthly discharge for Tamakoshi-III as contributed by baseflow, glacier runoff, snow runoff, and rain runoff. Results are shown the reference period (1981-2010), and the two future periods 2016-2045 and 2046-2075, which are based on the average of the RCP4.5 GCMs. Bottom: idem, but based on the RCP8.5 GCMs.**

From Figure 51 it is clear that rain runoff (surface runoff + lateral flow) is the largest contributor to the total discharge, which occurs mainly during the monsoon season. As a result of climate change we see an increase in precipitation and temperature, and thus an increase in rain runoff. The average monthly discharge is highest during August, and is approx. 400 $m^3/s$ for the reference period. This increases to 470 and 490 $m^3/s$ for 2016-2045 and 2046-2075, respectively (RCP4.5 GCM projections). This increase is higher for the RCP8.5 GCM projections, being 480 $m^3/s$ for 2016-2045 and 500 $m^3/s$ for 2046-2075. Compared to the



reference climate we notice a decrease in glacier runoff as a result of the melting and disappearing of glaciers. Another interesting change is the smaller contribution of snow runoff, which is especially evident during 2046-2075. This is the result of the increase in temperature, leading to more precipitation to fall as rain instead of snow.

The change in average monthly discharge at Tamakoshi-III is also shown in Figure 52, including uncertainty bands that reflect the difference between the maximum and minimum of the RCP GCMs. Based on this we may expect the average monthly discharge during August to vary between 450-500 $m^3/s$ during 2016-2045, and 450-550 $m^3/s$ during 2046-2075. The overall expected increase discharge is a positive development for Hydropower development.

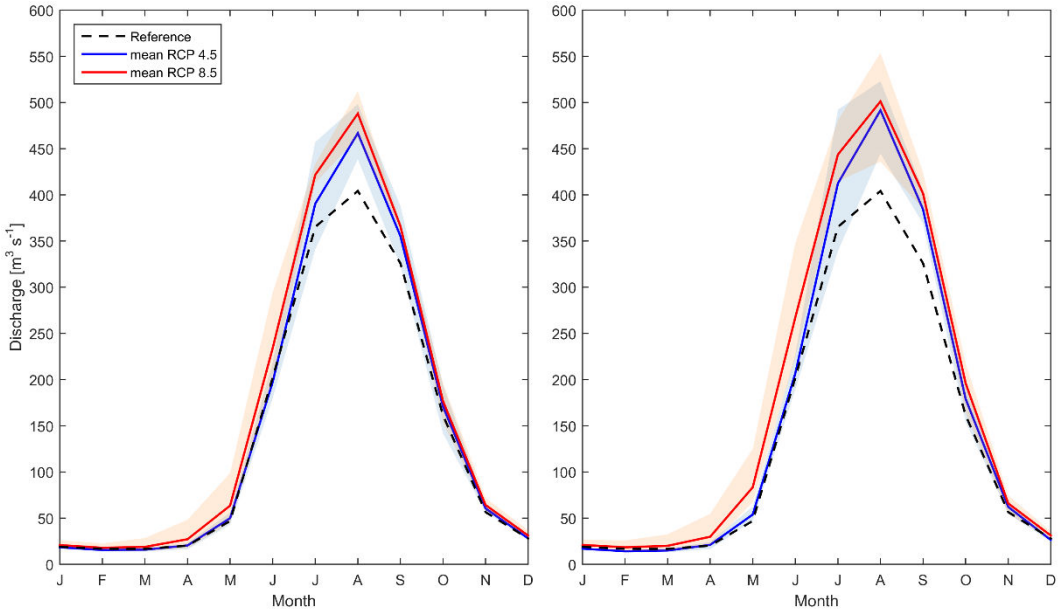


**Figure 52: Left: average monthly discharge for Tamakoshi-III for the reference climate, and the 2016-2045 period for the average of the RCP4.5 GCMs and RCP8.5 GCMs, respectively. Blue and red bands represent the range between the maximum and minimum of GCM projections for RCP4.5 and RCP8.5. Right: idem, but for the 2046-2075 period.**

### *9.2.3 Extremes*

The previous two sections focused on annual and monthly averages only, while for Hydropower development extreme discharge events may produce conditions outside the current dam design criteria. For example, run-of-river systems are unable to store discharge that exceeds the maximum production capacity. This section therefore analyzes the impact of climate on extreme river discharge by comparing the maximum annual discharge of the reference climate with those of the future climate.

Figure 53 shows the return periods of maximum annual discharge of the reference climate, and compares it with those of the two future periods 2016-2045 (left plots) and 2046-2075 (right plots), as represented by the 4 RCP4.5 GCMs (top plots) and 4 RCP8.5 GCMs (bottom plots). Since only 30 years of data was available, a Generalized-Extreme-Value (GEV) distribution [*Kotz and Nadarajah*, 2000] has been fitted through the data points to extent the analysis for return periods up to a 100 years.

For the reference climate (1981-2010) we notice that the maximum annual discharge that occurs once every 10 years is approx. 650 $m^3/s$. With the same probability (1/10 year), this

extreme discharge increases to 1000-1100 $m^3/s$ for 2016-2045, and 1200-1300 $m^3/s$ for 2046-2075, which is approx. twice as much as is the case for the reference period. Once every 100 years we may experience a river discharge of roughly 700 $m^3/s$. Although these long return periods are more uncertain, we already can see a substantial increase in maximum annual river discharge for this 1/100 year event for the two future periods. It is clear that the fit through the inmcm4_rcp45_r1i1p1 data points is very sensitive to one outlier, and therefore we put less confidence in this fit. Considering the other fits, however, it is clear that the 1/100 year maximum annual discharge in the future increases from 700 to approx. 1400 $m^3/s$ for 2016-2045, and to 1600 $m^3/s$ for 2046-2045.

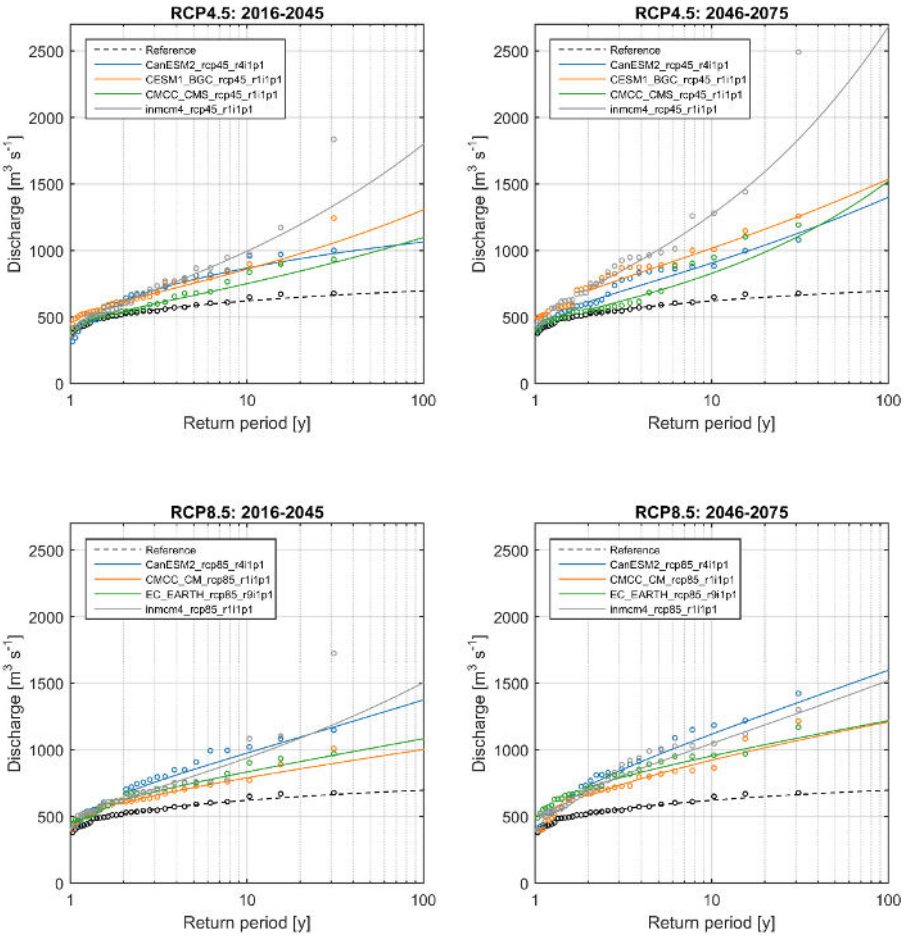


**Figure 53: Return periods of maximum annual discharge for Tamakoshi-III. A Generalized-Extreme-Value (GEV) distribution has been fitted through the data. Left and right plots differentiate between the two future periods, while top and bottom distinguish between RCP4.5 and RCP8.5.**

## 9.3 Khimti

### *9.3.1 Annual time-series of discharge*

Figure 54 and Figure 55 show the average annual discharge for the periods 1981-2010 and 2016-2075 for Khimti intake. The expected discharge simulated using the RCP4.5 GCMs as input is shown in Figure 54, while the expected discharge using the RCP8.5 GCMs as input is shown in Figure 55.



Compared to Tamakoshi-III, the river discharge at Khimti intake is substantially smaller (130 $m^3/s$ at Tamakoshi-III vs 23 $m^3/s$ at Khimti (annual average)). The average annual discharge for Khimti intake ranges between 15 and 30 $m^3/s$ for the reference period. Using the RCP4.5 GCM projections, we can expect an average annual discharge at Khimti intake that ranges between 15-35 $m^3/s$ during 2016-2075. An average annual river discharge of more than 35 $m^3/s$ is not unlikely in the future. The stronger increase in precipitation and temperature, as projected by the RCP8.5 GCMs, leads to higher discharge expectations for 2016-2075, ranging between 15-40 $m^3/s$. EC_EARTH_rcp85_r9i1p1 results in the highest projections of average annual river discharge, with values of more than 40 $m^3/s$ not being unlikely. This means we may expect twice the average annual discharge in the future for Khimti intake.

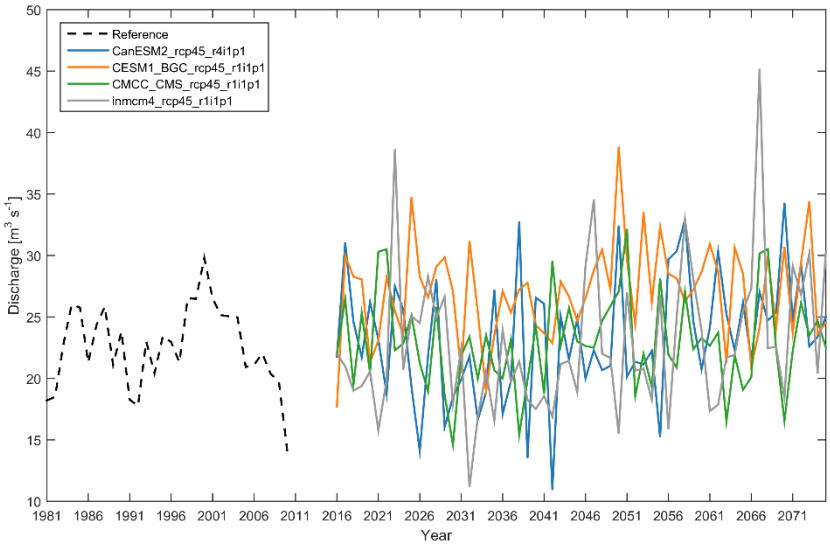


**Figure 54: Average annual discharge for Khimti intake for the reference climate and 4 RCP4.5 GCMs.**

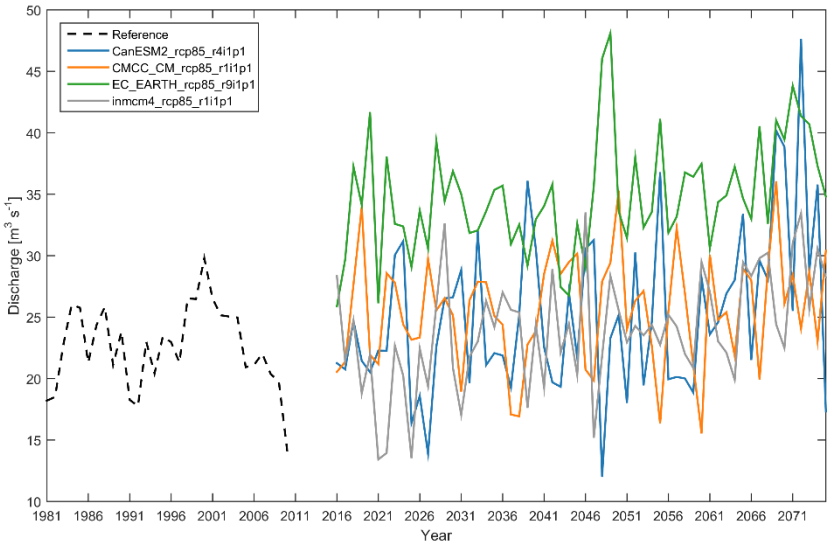


**Figure 55: Average annual discharge for Khimti intake for the reference climate and 4 RCP8.5 GCMs.**

### *9.3.2 Monthly changes*

Since almost no glaciers are to be found upstream of Khimti intake, discharge at Khimti is even more rainfall dominated than Tamakoshi-III. The contribution of each of the flow components to the total discharge at Khimti intake is shown in Figure 56 for the reference period (1981-2010),

and the two future periods 2016-2045 and 2046-2075. For the reference period, the annual contribution of these flow components to the total flow is 0% for glacier runoff, 2-3% for snow runoff, 20-21% for baseflow runoff, and 76-77% for rainfall runoff.

From Figure 56 it is clear that most discharge is generated during the monsoon season, which is mainly contributed by rain runoff (surface runoff + lateral flow). As a result of climate change we see an increase in precipitation, and thus an increase in rain runoff. The average monthly discharge is highest during August, and is approx. 67 $m^3/s$ for the reference period. This increases to nearly 72 and 79 $m^3/s$ for 2016-2045 and 2046-2075, respectively (RCP4.5 GCM projections). This increase is higher for the RCP8.5 GCM projections, being approx. 78 $m^3/s$ for 2016-2045 and 83 $m^3/s$ for 2046-2075. Because of the lower elevation area upstream of Khimti intake (Figure 2), most precipitation falls as snow, and does therefore barely contribute to the discharge.

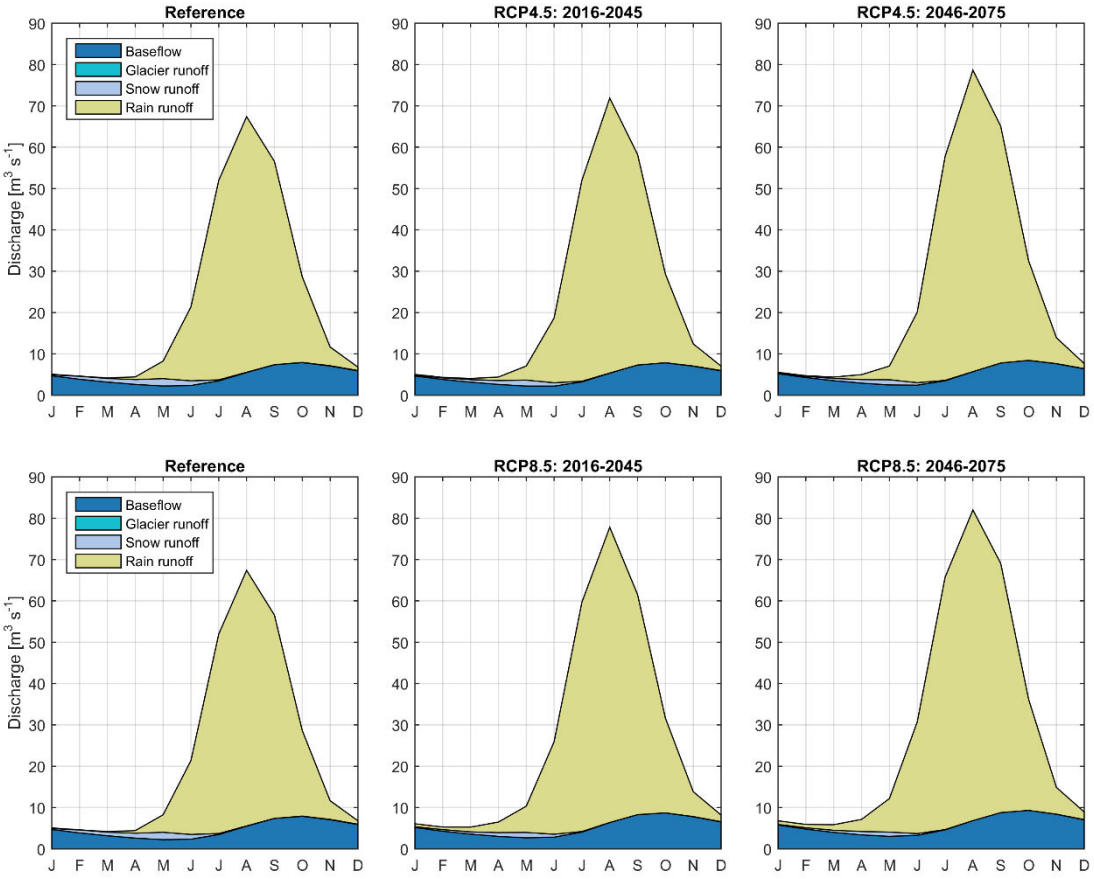


**Figure 56: Top: average monthly discharge for Khimti intake as contributed by baseflow, glacier runoff, snow runoff, and rain runoff. Results are shown the reference period (1981-2010), and the two future periods 2016-2045 and 2046-2075, which are based on the average of the RCP4.5 GCMs. Bottom: idem, but based on the RCP8.5 GCMs.**

The change in average monthly discharge at Khimti intake is also shown in Figure 56, including uncertainty bands that reflect the difference between the maximum and minimum of the RCP GCMs. Based on this we may expect the average monthly discharge during August to vary between 65-85 $m^3/s$ during 2016-2045, and 70-95 $m^3/s$ during 2046-2075. The overall expected increase discharge is a positive development for Hydropower development. We may also expect an increase in discharge during the pre-monsoon season.



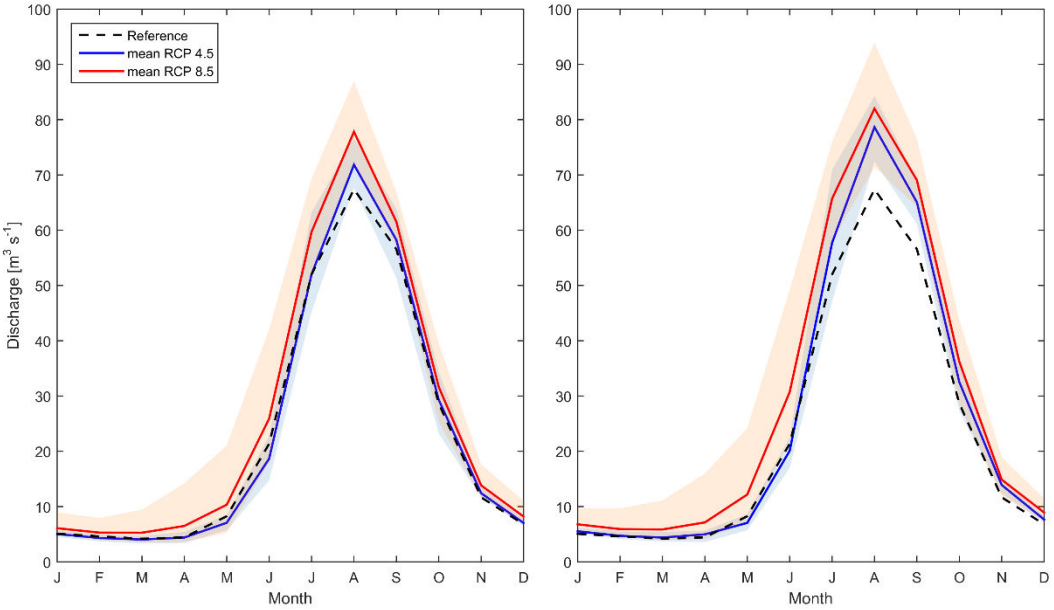


**Figure 57: Left: average monthly discharge for Khimti intake for the reference climate, and the 2016-2045 period for the average of the RCP4.5 GCMs and RCP8.5 GCMs, respectively. Blue and red bands represent the range between the maximum and minimum of GCM projections for RCP4.5 and RCP8.5. Right: idem, but for the 2046-2075 period.**

### *9.3.3 Extremes*

Similar as for Tamakoshi-III, Figure 58 shows for Khimti intake the return periods of maximum annual discharge of the reference climate, and compares it with those of the two future periods 2016-2045 (left plots) and 2046-2075 (right plots), as represented by the 4 RCP4.5 GCMs (top plots) and 4 RCP8.5 GCMs (bottom plots). Since only 30 years of data was available, a Generalized-Extreme-Value (GEV) distribution [*Kotz and Nadarajah*, 2000] has been fitted through the data points to extent the analysis for return periods up to a 100 years.

For the reference climate (1981-2010) we notice that the maximum annual discharge that occurs once every 10 years is approx. 110 $m^3/s$. With the same probability (1/10 year), this extreme discharge increases to 150-160 $m^3/s$ for 2016-2045, and 170-190 $m^3/s$ for 2046-2075. Once every 100 years we may experience a river discharge of roughly 130 $m^3/s$ for the reference period. Although these long return periods are more uncertain, we already can see a substantial increase in maximum annual river discharge for this 1/100 year event for the two future periods. The GEV fit through the inmcm4_rcp45_r1i1p1 data points is very sensitive to one outlier, and therefore we put less confidence in this fit. Considering the other fits, however, it is clear that the 1/100 year maximum annual discharge in the future increases from 130 to approx. 190-200 $m^3/s$ for 2016-2045, and to 240-330 $m^3/s$ for 2046-2075.

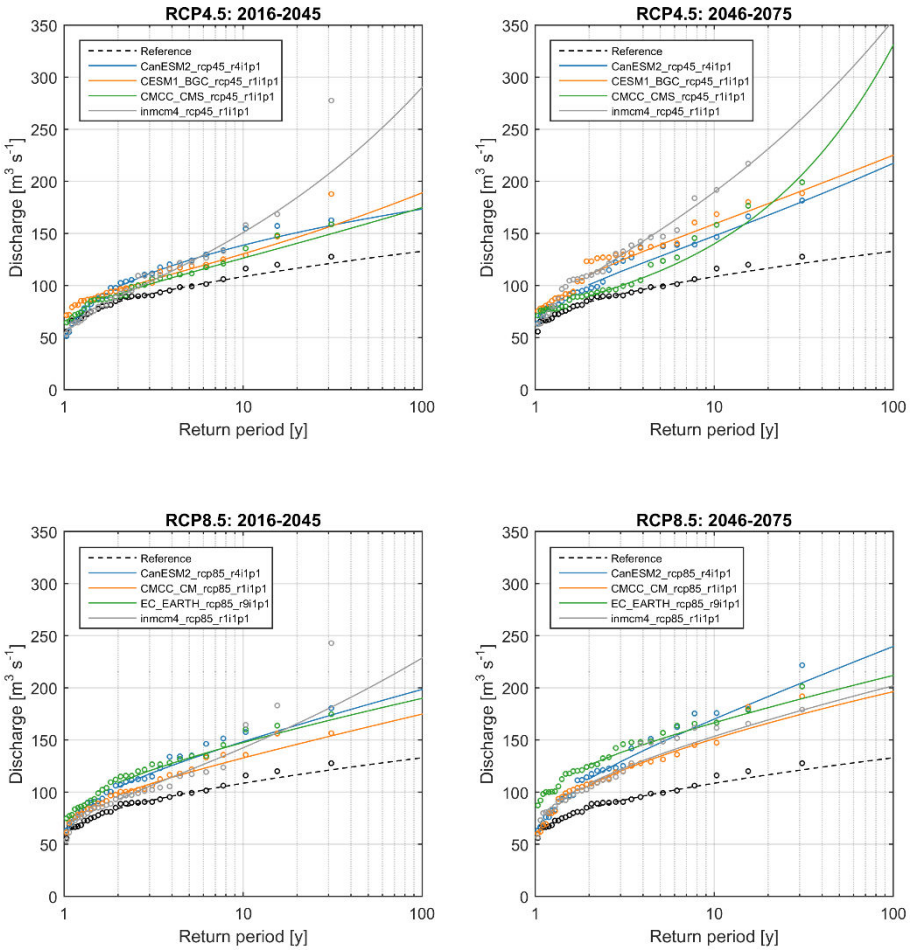


**Figure 58: Return periods of maximum annual discharge for Khimti intake. A Generalized-Extreme-Value (GEV) distribution has been fitted through the data. Left and right plots differentiate between the two future periods, while top and bottom distinguish between RCP4.5 and RCP8.5.**

# 10 Hydropower Potential

## 10.1 Approach

### *10.1.1 Overall*

In the previous Chapters a detailed understanding of present hydrology and future changes to the hydrological cycle and its uncertainty has been presented. It is very relevant in terms of investment decisions to what extent this will affect potential hydropower generation. The Water Evaluation and Planning tool (WEAP) [*Sieber and Yates*, 2015] is used to asses this potential hydropower production. The simulated daily discharge from the SPHY model (see previous Chapter) at two proposed hydropower locations (Tamakoshi-III and Khimti) were fed into the WEAP model to evaluate hydropower potential under various climate change projections and hydropower facility design scenarios. WEAP has been used in the past to predict successfully hydropower in the Himalayan region [*Sahukhal and Bajracharya*, 2015], and more specifically for impact of climate change on hydropower [*Droogers et al.*, 2009].

Potential hydropower locations used are shown in Figure 59. Two locations are selected for further analysis: Tamakoshi-III (dam) and Khimti-intake (run-off-river). Summarized characteristics of these two potential locations are provided in Table 12.

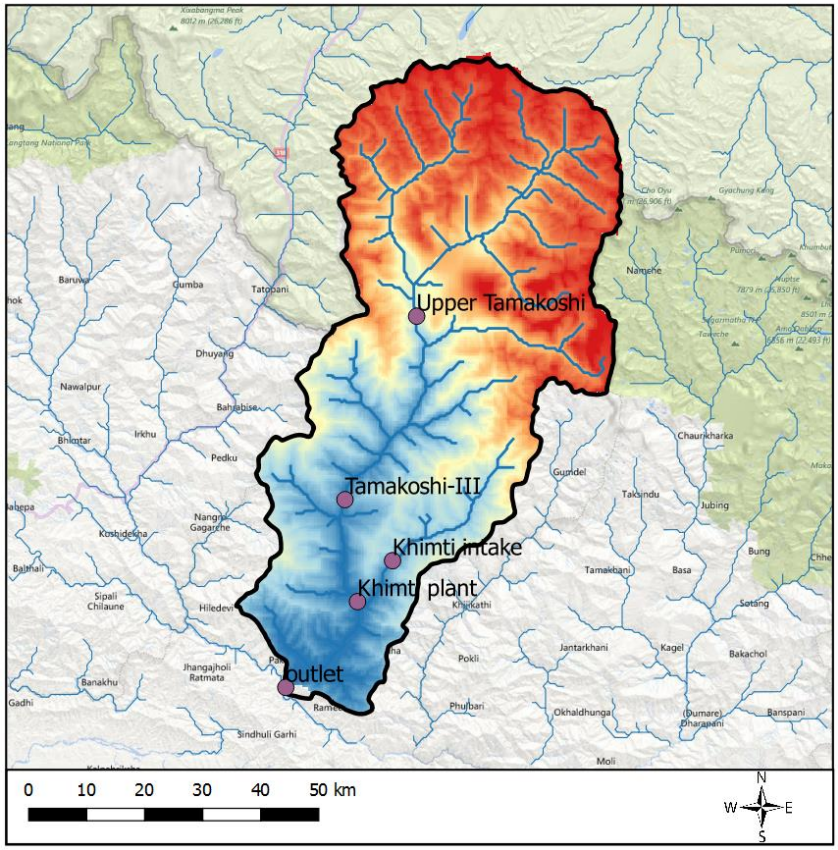


**Figure 59: Location of the proposed hydropower site. Tamakoshi-III (dam) and Khimti-intake (ROR) were selected for further analysis.**

**Table 12: Main characteristics of the two proposed hydropower facilities. Tamakoshi-III has a reservoir and Khimti-intake is a run-off-river.**

| | Tamakoshi-III | Khimti-Intake |
|---|---|---|
| *RESERVOIR* | | |
| Reservoir (MCM) | 157 | N/A |
| Highest level (masl) | 940 | N/A |
| Lowest level (masl) | 890 | N/A |
| Tunnel inlet (masl) | 860 | N/A |
| Weir length effective (m) | 200 | N/A |
| Tailwater elevation (masl) | 660 | N/A |
| *HYDROPOWER* | | |
| Max turbine flow (m3/s) | 306 | 11.65 |
| Plant factor (%) | 90 | 90 |
| Generating efficiency (%) | 92 | 92 |
| Head (m) | 330/380 | 660 |
| Installed capacity (MW) | 600 | 60 |

### *10.1.2 WEAP model*

WEAP places the demand side of the equation--water use patterns, equipment efficiencies, re-use, prices, hydropower energy demand, and allocation--on an equal footing with the supply side--streamflow, groundwater, reservoirs and water transfers. WEAP is a laboratory for examining alternative water development and management strategies. There are various reasons for choosing the WEAP framework. Most important is that WEAP is completely focused towards scenario analysis in a user-friendly approach. Second, WEAP is very scalable and a first-order setup of a particular region can be easily expanded when more data/resources are available. Third, WEAP is commonly used world-wide for IWRM analyses, including hydropower assessment.

A detailed discussion on WEAP can be found in the WEAP manual which can be obtained from the WEAP website (http://www.weap21.org/). In summary WEAP has the following features:

- Integrated Approach: Unique approach for conducting integrated water resources planning assessments.
- Stakeholder Process: Transparent structure facilitates engagement of diverse stakeholders in an open process.
- Water Balance: A database maintains water demand and supply information to drive mass balance model on a link-node architecture.
- Hydropower Analysis: A versatile approach to hydropower scenario analysis in an integrated way, including impacts and economics.
- Simulation Based: Calculates water demand, supply, runoff, infiltration, crop requirements, flows, and storage, and pollution generation, treatment, discharge and in-stream water quality under varying hydrologic and policy scenarios.
- Policy Scenarios: Evaluates a full range of water development and management options, and takes account of multiple and competing uses of water systems.
- User-friendly Interface: Graphical drag-and-drop GIS-based interface with flexible model output as maps, charts and tables.
- Model Integration: Dynamic links to other models and software, such as QUAL2K, MODFLOW, MODPATH, PEST, Excel and GAMS. Links to all other models can be developed quite easily since WEAP can read and write plain text files similar as SWAT, SPHY, SWAP, Mike11, HEC-HMS, HEC-RAS and Geo-SFM.



For this specific study focus is on the hydropower modules of WEAP. However, the model as developed can be easily extended to make a more balanced analysis for competing water demand scenarios.

Hydropower generation in WEAP is computed from the flow passing through the turbine, based on the reservoir release or run-of-river streamflow, and constrained by the turbine's maximum flow capacity. Note that the amount of water that flows through the turbine is calculated differently for local reservoirs, river reservoirs and run-of-river hydropower. For river reservoirs, all water released downstream is sent through the turbines, but water pumped from the reservoir to satisfy direct reservoir withdrawals is not sent through the turbines. For local reservoirs, all linked demand sites are assumed to be downstream of the reservoir, so all reservoir releases are sent through the turbines. For run-of-river hydropower nodes, the "release" is equal to the downstream outflow from the node. Details of the calculation algorithms can be found in the WEAP User Guide.

### *10.1.3 Model Setup*

The WEAP model has been setup based on the design characteristics of the potential hydropower facilities and the flow data as generated by the SPHY model (see previous Chapter). In the figure below a screenshot of the developed model is shown. Extensive use of the so-called “Read-By-File” option was used to ensure a good connection to the SPHY model results. Also “Key-Assumptions” were used effectively to ease scenario analysis. Finally, WEAP’s built in API (application programming interface) was used to automate various input and output processes.

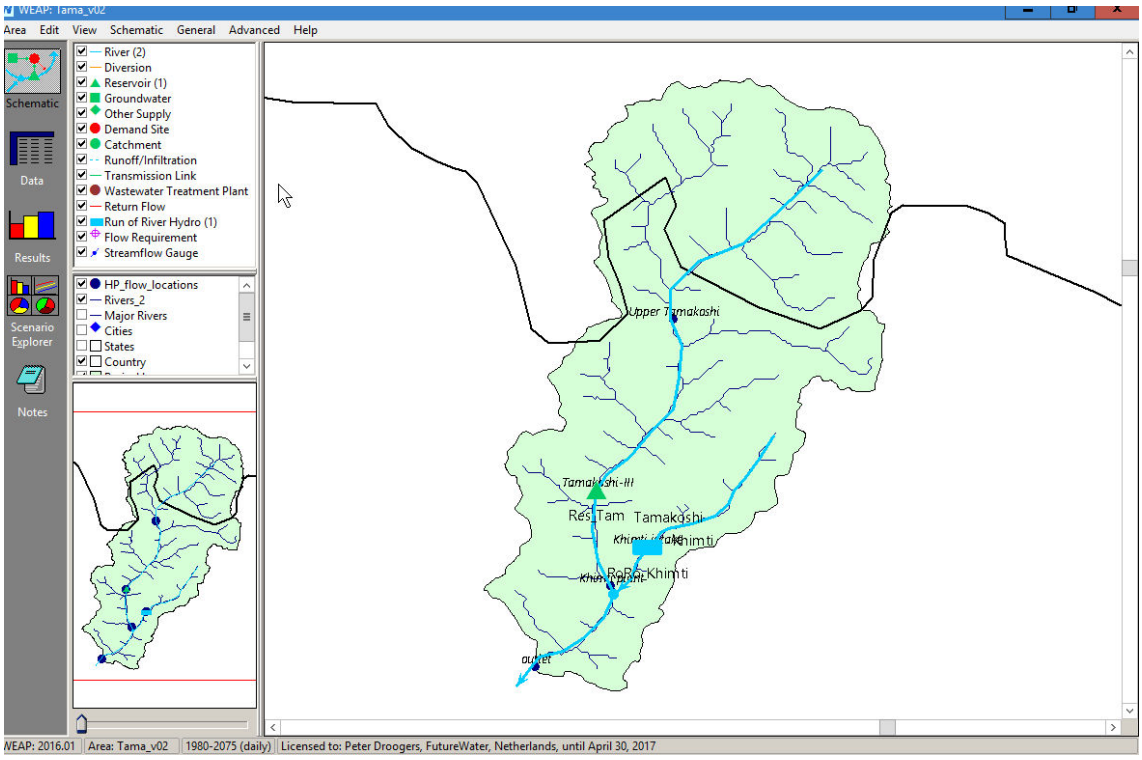


**Figure 60: Screenshots of the WEAP model as developed for the Tamakoshi River Basin: schematic overview of main model components.**

## 10.2 Current situation

The WEAP models was first setup to explore what the hydropower production would have been in the past assuming the Tamakoshi-III and the Khimti hydropower plants were effective. To consider variation in weather conditions a 30-years period (1981-2010) was used. Expected hydropower production would be on average 2743 GWh/y of which Tamakoshi-III would have generated 2354 GWh/y and Khimti 389 GWh/y (Table 13). Year-to-year variation is modest (Figure 61) with during drier years (1981-1982 and 2009-2010) annual production levels around 10% lower than long-term averages. Day-to-day variation is however substantial with peak levels during July to October (Figure 62). Obviously for Khimti with its run-of-river plant, no regulation is possible. For Tamakoshi-III, with a reservoir, regulation and storage might be possible. For this specific study the operational rule was set that a maximum of 4% of reservoir storage can be abstracted on each particular day. Obviously, more advanced operational rules are possible depending on the overall energy demand policies.

A comparison between initial calculations of Statkraft's hydropower model for Khimti and the results for WEAP is made. Figure 63 shows that overall results are quite comparable, differences might result from differences in calculation algorithms.

**Table 13: Potential hydropower production over a historic period of 30 years (1981-2010) assuming that hydropower station would have exist.**

| | Tamakoshi-III | Khimti | Total |
|---|---|---|---|
| Average (GWh/y) | 2354 | 389 | 2743 |
| Minimum (GWh/y) | 1997 | 320 | 2332 |
| Maximum (GWh/y) | 2540 | 448 | 2988 |

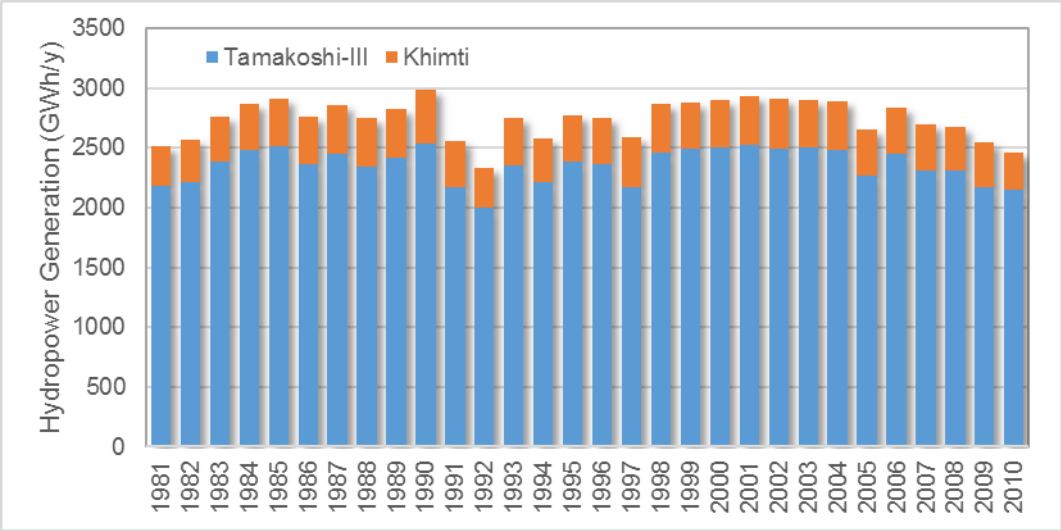


**Figure 61: Stacked bar plot of potential hydropower generation over the last 30 years, assuming Tamakoshi-III and Khimti would have been constructed and operational.**

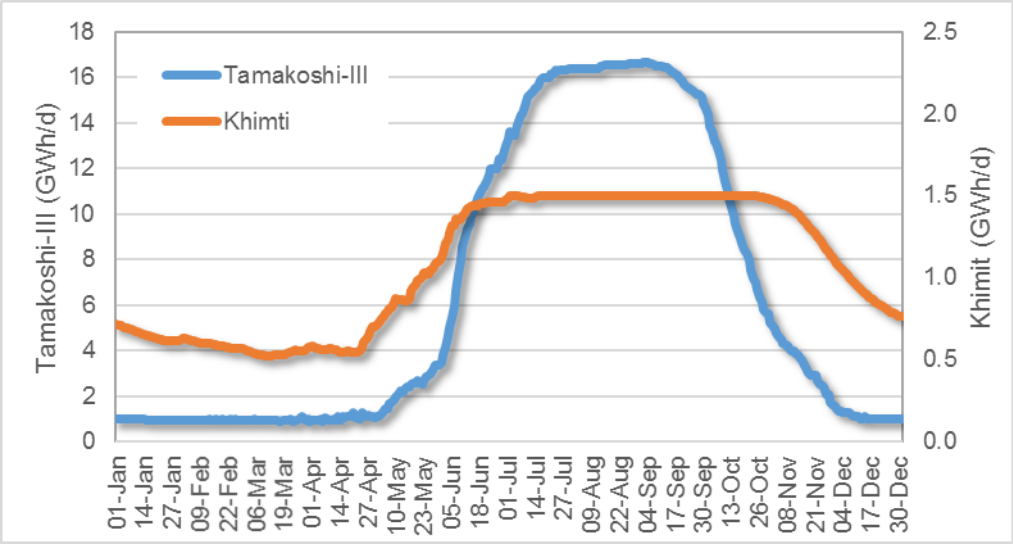


**Figure 62: Potential hydropower generation over the last 30 years assuming Tamakoshi-III and Khimti would have been constructed and operational. Figure display the daily averages over a period of 30 years (1981-2010).**

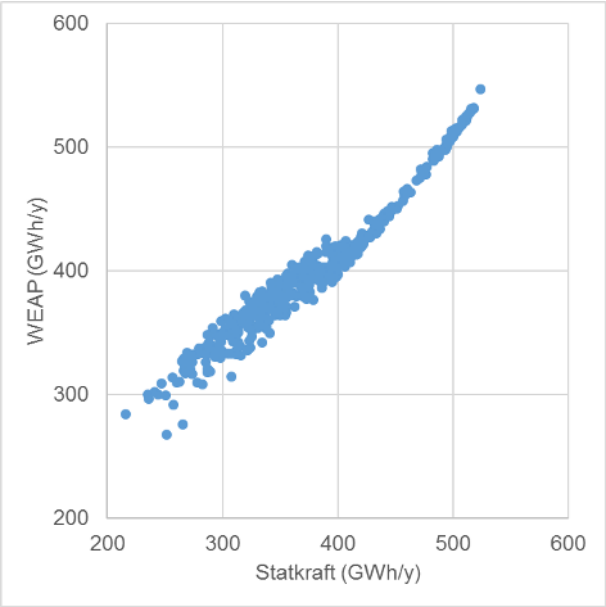


**Figure 63: Comparison of the potential hydropower generation for Khimti based on the Statkraft and the WEAP (this report) methodology. Results are presented for the period 2016-2075 and for the eight climate scenarios combined.**

## 10.3 Hydropower production under changing climate

Based on the flows as calculated by the SPHY model for the eight climate projections expected hydropower production is calculated using the WEAP model. There is quite some variation of projected hydropower generation based on the climate models, the RCP and the time horizon considered. In Figure 64 the full range of projected hydropower generation for the eight scenarios and for all the years is shown. The Figure shows that in general the climate models behave in the same trend, with the exception of the EC-Earth model (a model based on the ECMWF weather forecast model).

Overall, higher hydropower production can be expected in the future as a results of higher discharge. These higher discharges are expected because of the increase in precipitation in combination with changes in glaciers' extent. The differences between the RCp4.5 and RCP 8.5 projections is quite noticeable (Figure 65 and Figure 66), but in general a positive trend can be seen for both.

Year-to-year variation in hydropower production is explored and can be quite high and is climate model dependent (Figure 67 and Figure 68). Somewhat surprisingly, this annual variation for Tamakoshi-III is higher compared to Khimti (Figure 69 and Figure 70), while Tamakoshi-III has a regulating reservoir. Main reason is that the storage capacity of Tamakoshi-III is relatively low compared to the high flows during the wet season. Other reason is that Khimti's design capacity is relatively low, so even in years with low flows it still operates at its design capacity.

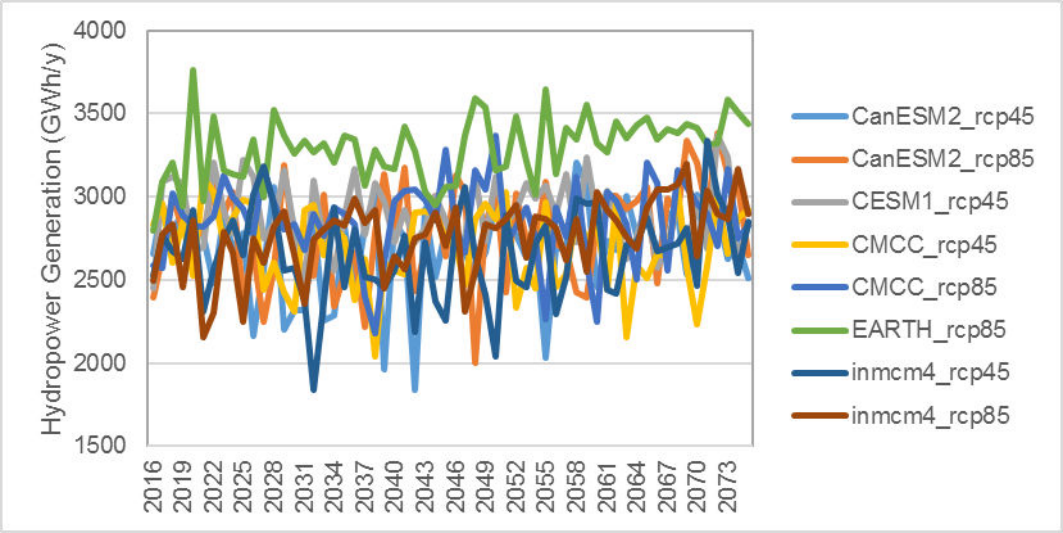


**Figure 64: Potential hydropower generation (sum of Tamakoshi-III and Khimti) under the eight climate change projections.**

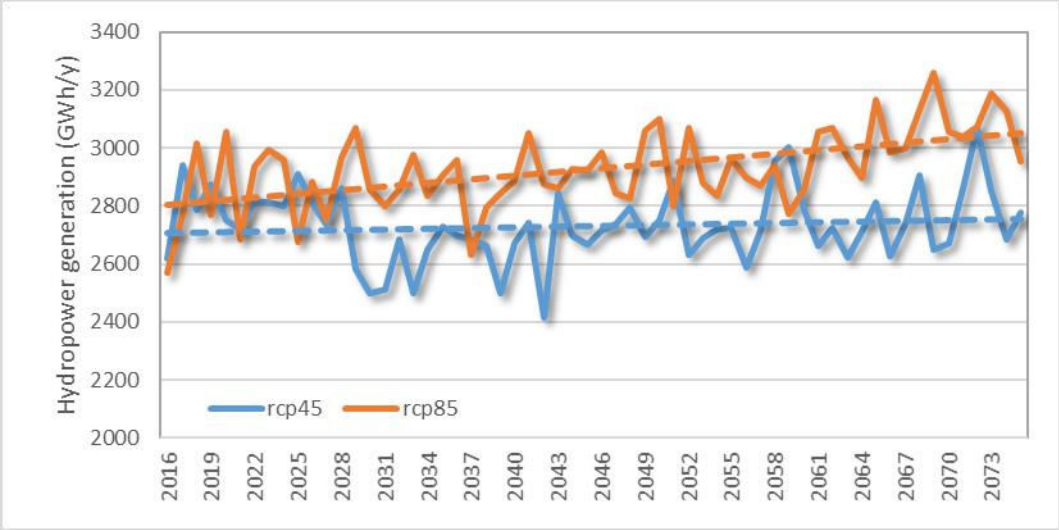


**Figure 65: Potential hydropower generation (sum of Tamakoshi-III and Khimti) under the eight climate change projections averaged over RCP4.5 and RCP8.5.**

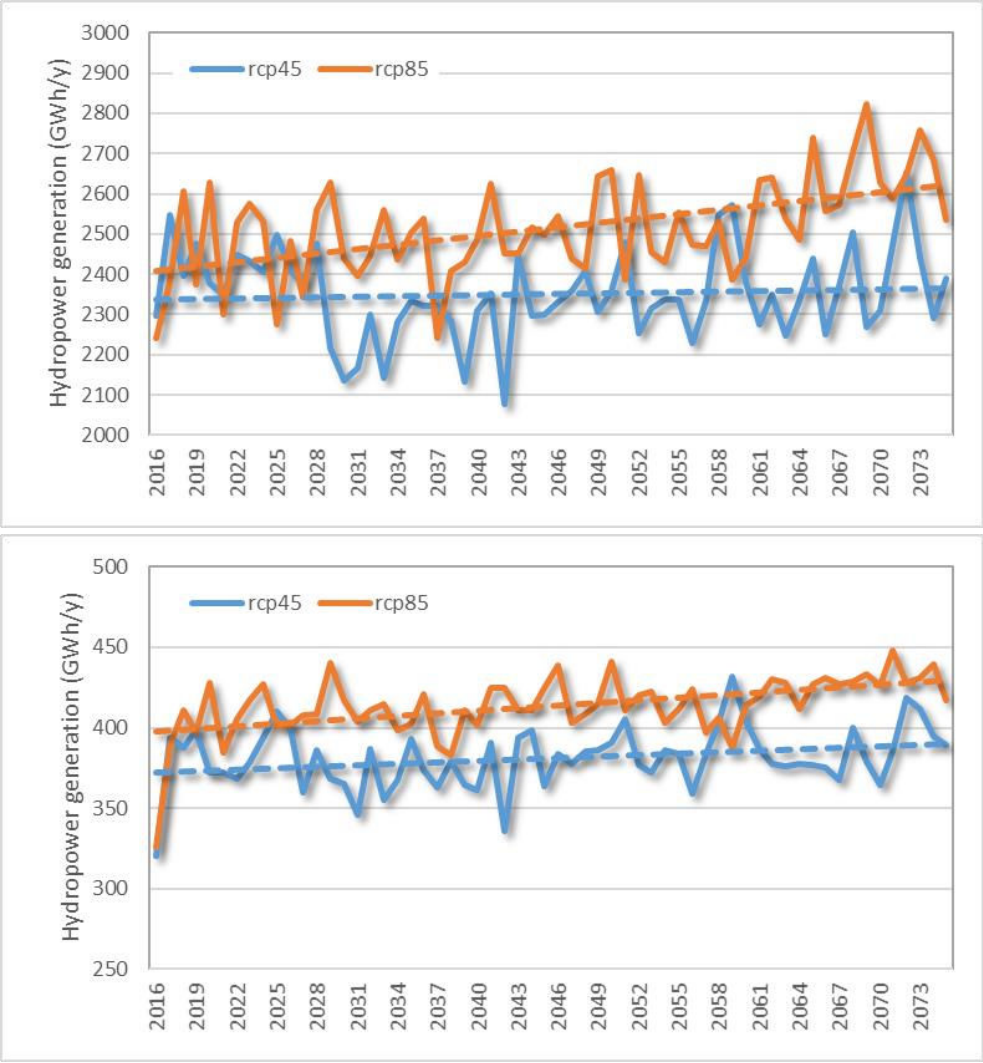


**Figure 66: Potential hydropower generation under the eight climate change projections averaged over RCP4.5 and RCP8.5. Tamakoshi-III (top) and Khimti (bottom).**

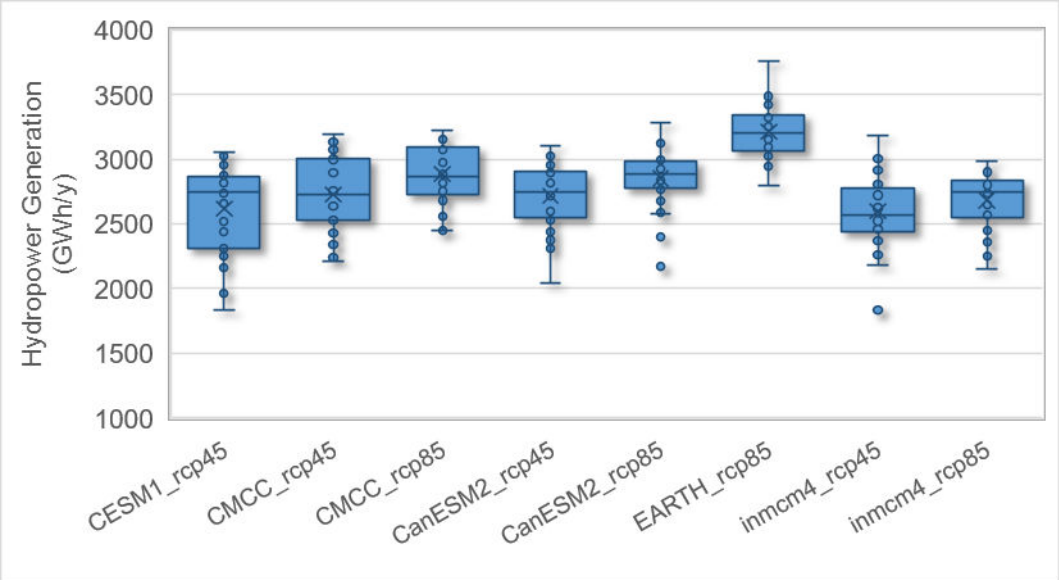


**Figure 67: Potential hydropower generation (sum of Tamakoshi-III and Khimti) under the eight climate change projections for the near future (2016-2045).**

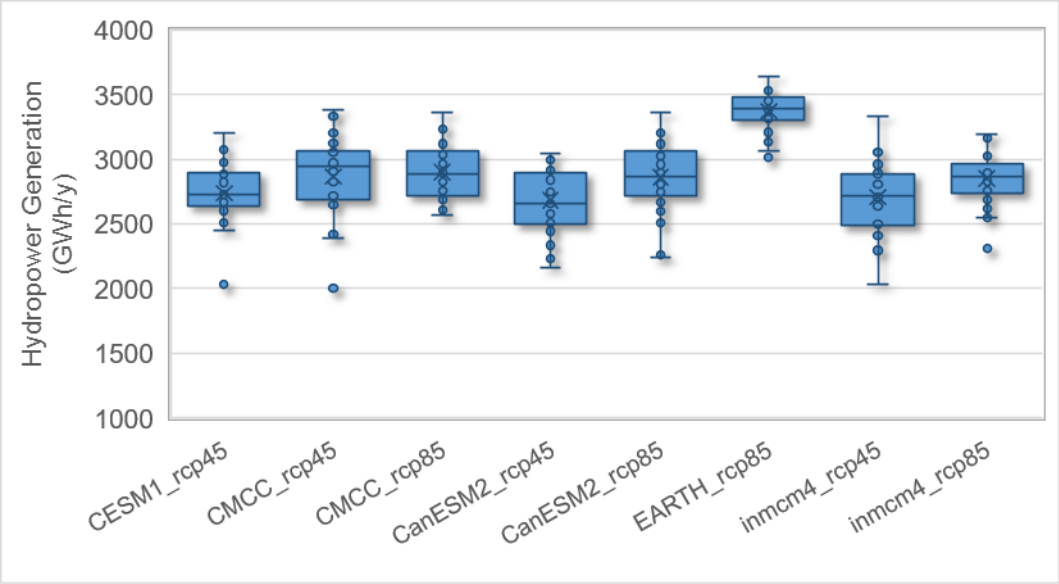


**Figure 68: Potential hydropower generation (sum of Tamakoshi-III and Khimti) under the eight climate change projections for the distant future (2046-2075).**

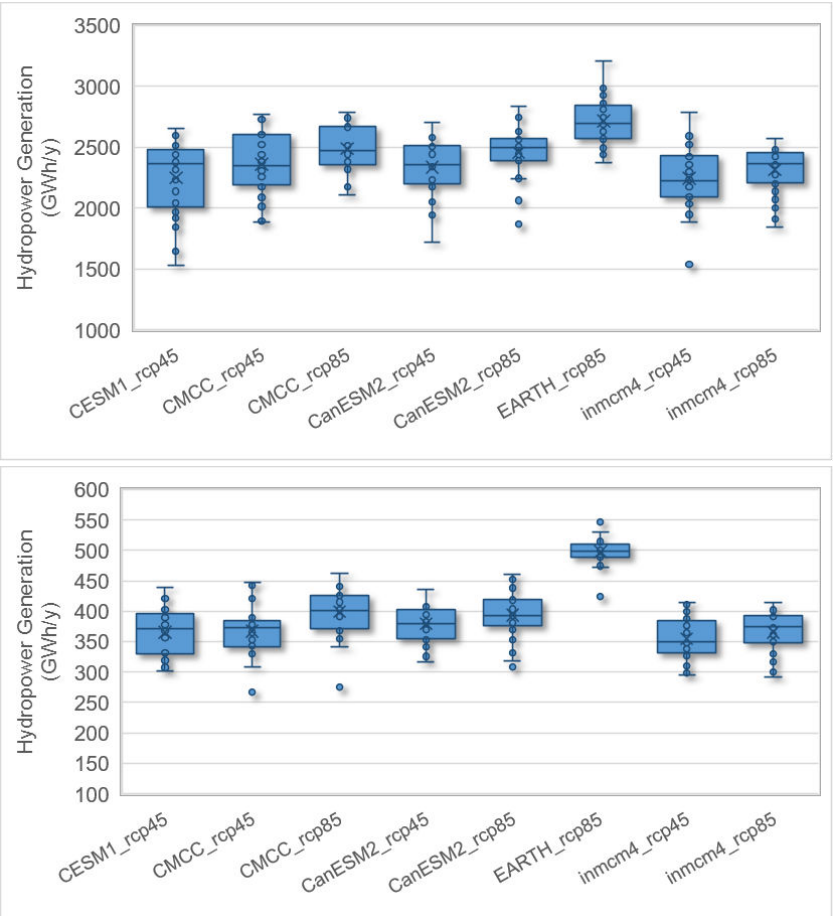


**Figure 69: Potential hydropower generation under the eight climate change projections for the near future (2016-2045). Tamakoshi-III (top) and Khimti (bottom).**

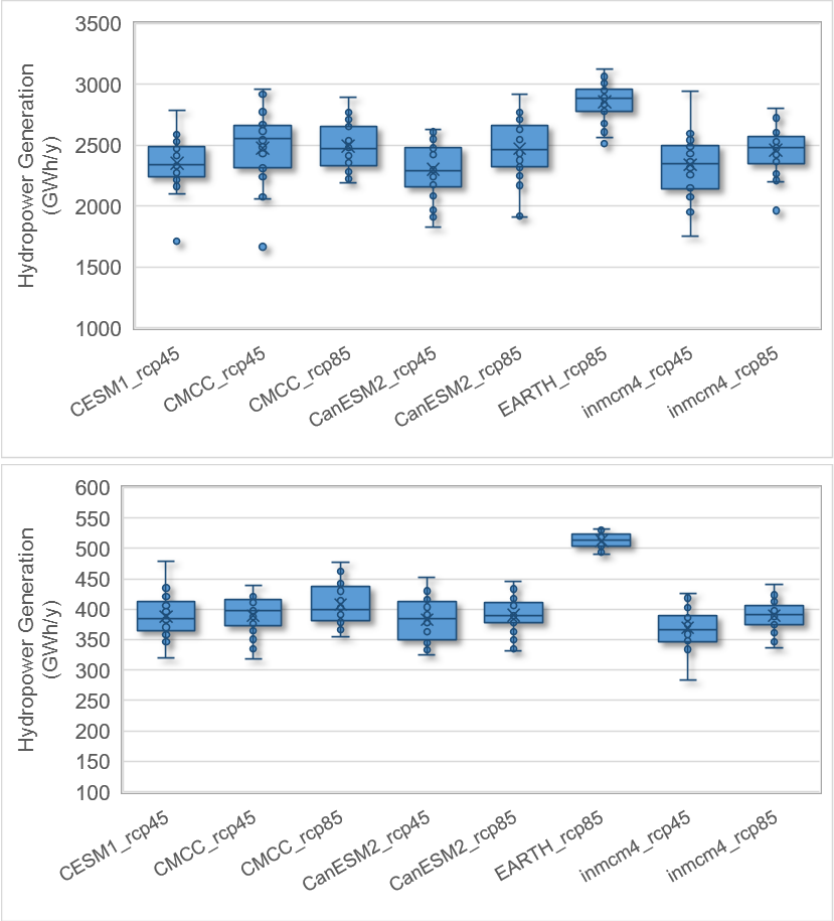


**Figure 70: Potential hydropower generation under the eight climate change projections for the distant future (2046-2075). Tamakoshi-III (top) and Khimti (bottom).**

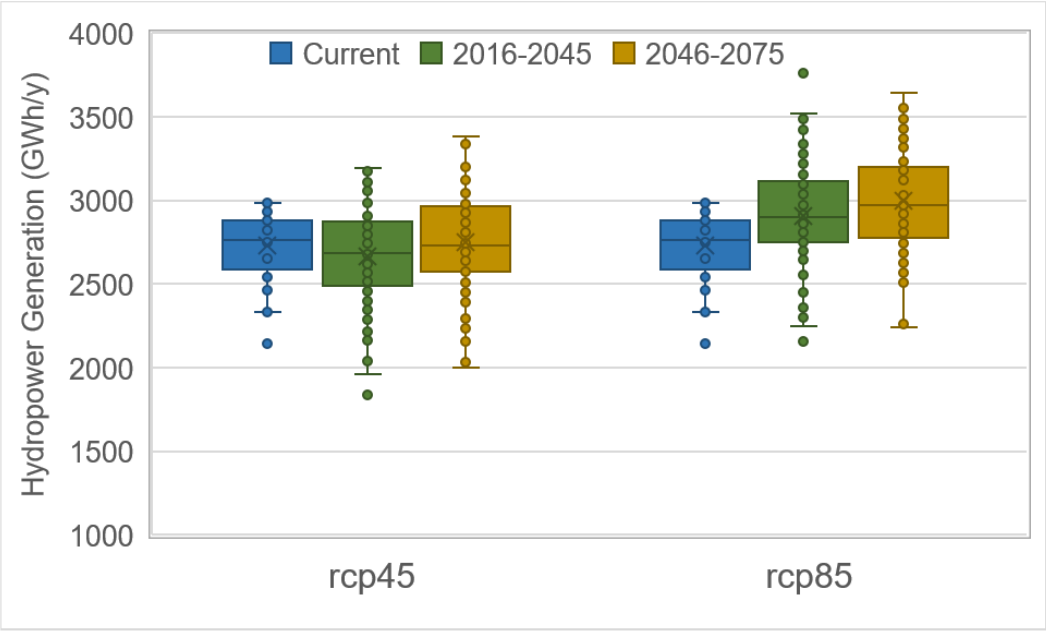


**Figure 71: Potential hydropower generation (sum of Tamakoshi-III and Khimti) for the near (2016-2045) and distant (2046-2075) future presented as box-whisker plots.**

## 10.4 Scenario Analysis of Hydropower Potential

Results presented in the previous sections are based on the designed hydropower specifications and show that climate change will have a limited impact on the forecasted hydropower production. Overall, a small increase in hydropower production can be expected in the future due to changes in discharge. To explore whether other design capacities of the two facilities might impact hydropower production an initial set of scenarios has been analyzed. The same modeling approach using WEAP was used and two types of scenarios were evaluated: (i) different reservoir capacities of Tamakoshi-III, and (ii) different maximal turbine flows for Tamakoshi-III and Khimti. All scenarios were analyzed for the eight set of climate models and focus is again on the near-future 2016-2045 and 2046-2075.

Main conclusions regarding the reservoir scenarios is that an increase in reservoir storage capacity will benefit hydropower production to a certain extend (Figure 72). For the quite extreme increase in reservoir capacity of 2 to 5 times, hydropower generation will increase by about 5% to 22% for Tamakoshi-III. An extended benefit-cost analysis could reveal whether such an expansion of design reservoir capacity is cost-effective. Likewise, reducing the storage capacity by 50% would reduce hydropower projection by about 8%. These results are all based assuming that operational rules for releases from the reservoir will remain unchanged.

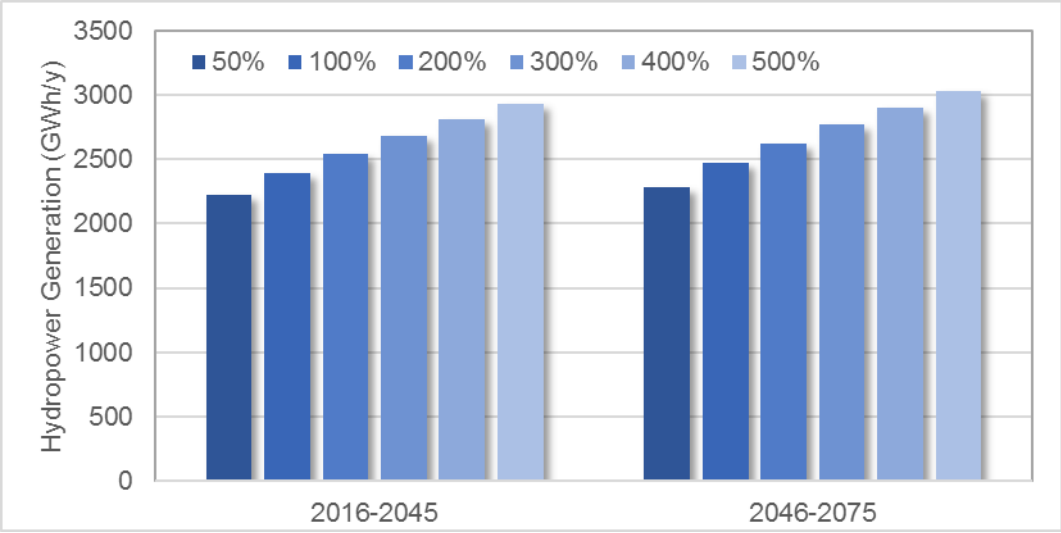


**Figure 72: Potential hydropower generation of Tamakoshi-III for a range of reservoir storage capacities (100% is 157 MCM).**

For the scenario on changes in design capacity of the maximum turbine flow results (Tamakoshi-III and Khimti combined) are shown in Figure 73. Doubling the design capacity will increase projected hydropower production by about 20%. For Tamakoshi-III only (Figure 74), the proposed design capacity seems to be well planned, as an increase will have only a minor impact on hydropower generation. However, for Khimti there seems to be a real potential to reevaluate the maximum flow design capacity; doubling the capacity will generate about 55% more hydropower.

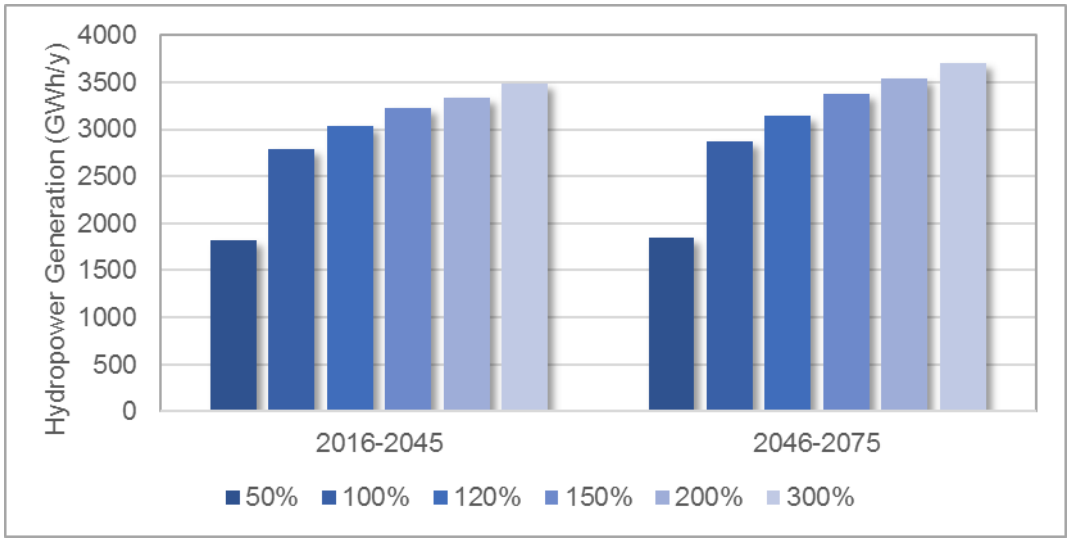


**Figure 73: Potential hydropower generation (sum of Tamakoshi-III and Khimti) for a range of maximum turbine flow designs.**

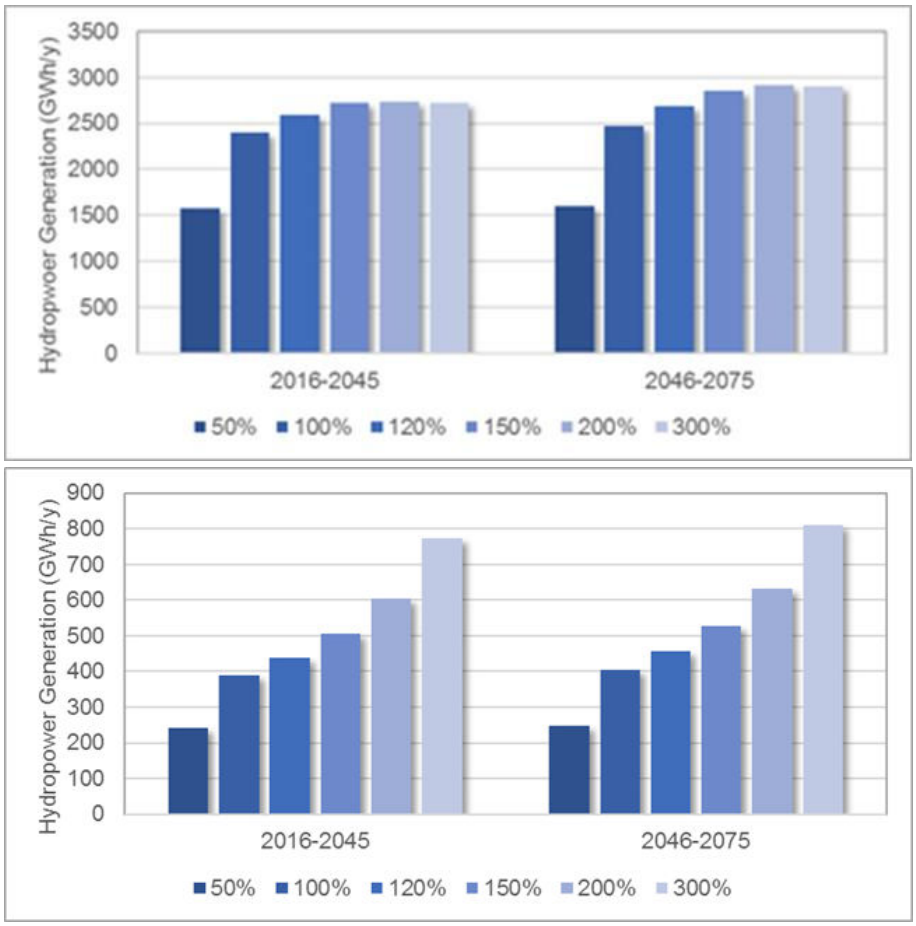


**Figure 74: Potential hydropower generation for a range of maximum turbine flow designs. Top: Tamakoshi-III (100% is 306 $m^3 s^{-1}$); bottom: Khimti (100% is 11.65 $m^3 s^{-1}$).**

# 11 Conclusions and recommendations

## 11.1 Conclusions

As a result of a changing climate [*Immerzeel et al.*, 2010; *Lutz and Immerzeel*, 2013; *Lutz et al.*, 2014b] and growing demand in energy for Nepal [*DOED*, 2016; *Shrestha et al.*, 2016], Statkraft[1], as being the largest developer for hydropower in this region, is interested in the impact of climate change on the potential for hydropower development in the Tamakoshi River Basin, Nepal. The overall objective of this study was therefore to improve the understanding of the expected impacts of climate change on water availability in the context of potential hydropower development in the Tamakoshi River Basin, with a specific focus on the hydropower plants Tamakoshi-III and Khimti.

This objective was achieved by forcing a spatially distributed hydrological model (SPHY, [*Terink et al.*, 2015]) with a baseline climate (representing current climate conditions), and an ensemble of 8 possible future climates, represented by 8 statistically downscaled GCMs (General Circulation Models) of which 4 GCMs were selected from the Representative Concentration Pathway (RCP) 4.5 and 4 from RCP 8.5. The change in precipitation, temperature, glacier melt, and river discharge between the baseline climate and future climates was evaluated for the entire Tamakoshi river basin, and specifically for Tamakoshi-III and Khimti. Simulated river discharges from the baseline climate and future climates were used as input in the "Water Evaluation and And Planning" (WEAP) system to assess the potential for hydropower under the baseline and future climate, whereas for the future climate the potential was evaluated using various storage capacities and maximum turbine flow designs.

For the entire basin it can be concluded that we can expect an overall increase in precipitation and temperature, and a gradual decrease in glacier melt. Since the change in flow due to the increase in precipitation is larger than the decrease in glacier melt, and the contribution of glacier melt to the total river discharge in this basin is minor, an increase in river discharge is projected for the future. Precipitation is expected to increase with 2-8% for 2016-2045, and with 12-18% for 2046-2075. This increase is strongest during July-August, with an average of 550 mm month$^{-1}$ for the baseline climate increasing towards 650 mm month$^{-1}$ for 2016-2045, and 700 mm month$^{-1}$ for 2046-2075. The average annual basin temperature is expected to increase with 0.5-1.4 °C for 2016-2045, and with 1.4-2.9 °C for 2046-2075. The contribution from glacier melt to the total discharge is minor, and is on basin average approx. 23 mm month$^{-1}$ during July-August for the baseline climate. This may decrease to 18-23 mm month$^{-1}$ for 2016-2045, and 8-19 mm month$^{-1}$ for 2046-2075. For August the average discharge may increase from approx. 375 to 475 mm month$^{-1}$ for 2016-2045, and to 500 mm month$^{-1}$ for 2046-2075. During October-December no substantial changes in river discharge are expected.

For Tamakoshi-III we may expect average annual discharges varying between 125-225 m$^3$/s in the future (currently 130 m$^3$/s on average). This increase is mainly contributed to the increase in rainfall, especially during the monsoon season. The current monthly average discharge at Tamakoshi-III peaks at 400 m$^3$/s during August, whilst this may increase towards 450-500 m$^3$/s for 2016-2045, and 450-550 m$^3$/s for 2046-2075. Extreme analyses showed that the maximum annual discharge with a return period of once every 10 years for the baseline climate is approx. 650 m$^3$/s for Tamakoshi-III. With the same probability (1/10 year), this extreme discharge increases to 1000-1100 m$^3$/s for 2016-2045, and 1200-1300 m$^3$/s for 2046-2075. The current

[1] http://www.statkraft.com/



maximum annual discharge with 100-year return period is approx. 700 $m^3/s$. These numbers are estimated using GEV-fits, and should therefore interpreted with care. As a result of climate change, this maximum annual discharge with 100-year return period may increase towards 1400 $m^3/s$ for 2016-2045, and to 1600 $m^3/s$ for 2046-2045.

Compared to Tamakoshi-III, Khimti is located in a much smaller tributary and therefore river discharge is substantially smaller for Khimti. Also for Khimti we can conclude an increase in average annual river discharge. For the baseline climate the average annual discharge is approx. 23 $m^3/s$, and this may increase towards 30-35 $m^3/s$. For Khimti this increase is only contributed by rainfall, since no glaciers are to be found upstream of Khimti. Same as for Tamakoshi-III, monthly discharge at Khimti peaks during August with an average monthly discharge of 67 $m^3/s$ for the baseline climate. This can be expected to increase towards 65-85 $m^3/s$ during 2016-2045, and 70-95 $m^3/s$ during 2046-2075. Extreme analyses showed that the maximum annual discharge with a return period of once every 10 years for the baseline climate is approx. 110 $m^3/s$ for Khimti. With the same probability (1/10 year), this extreme discharge increases to 150-160 $m^3/s$ for 2016-2045, and 170-190 $m^3/s$ for 2046-2075. The current maximum annual discharge with 100-year return period is approx. 130 $m^3/s$. The maximum annual discharge with 100-year return period may increase towards 190-200 $m^3/s$ for 2016-2045, and to 240-330 $m^3/s$ for 2046-2075.

Using the SPHY simulated discharge from the baseline climate as input to the WEAP model, the average energy production was estimated to be 2354 and 389 GWh/y for Tamakoshi-III and Khimti, respectively. Annual fluctuations in energy production are small with maxima and minima ranging between 2540 and 1997 GWh/y for Tamakoshi-III, and 448 and 320 GWh/y for Khimti. Seasonal energy production levels differ substantially, with the largest energy production during the months June-October.

As a result of the expected increase in river discharge, higher hydropower production can be expected in the future. The annual variation for Tamakoshi-III is higher compared to Khimti, while Tamakoshi-III has a regulating reservoir. Main reason for this is that the storage capacity of Tamakoshi-III is relatively low compared to the high flows during the wet season. Another reason is that Khimti's design capacity is relatively low, so even in years with low flows it still operates at its design capacity. The total energy production from both plants is expected to increase from 2700-2800 GWh/y to 2750-3050 GWh/y on average. For Tamakoshi-III only, an increase is expected from 2350-2400 GWh/y to 2370-2600 GWh/y. The increase for Khimti is from 370-400 GWh/y to 390-430 GWh/y. While the increase in discharge is a positive development for hydropower generation, the increase in total flow and extremes may have a negative impact on floods, the vulnerability of infrastructure, erosion, and the sedimentation of reservoirs.

Using WEAP two types of scenarios were evaluated: (i) different reservoir capacities of Tamakoshi-III, and (ii) different maximal turbine flows for Tamakoshi-III and Khimti. With an increase in reservoir capacity of 2 to 5 times, hydropower generation will increase by about 5% to 22% for Tamakoshi-III. Likewise, reducing the storage capacity by 50% would reduce hydropower projection by about 8%. For the different maximum turbine flow scenarios, it can be concluded that for Tamakoshi-III the maximum turbine flow design capacity is well-planned, as an increase will have only a minor impact on hydropower generation. However, for Khimti there seems to be a real potential to re-evaluate the maximum flow design capacity; doubling the capacity will generate about 55% more hydropower.

These projected potential hydropower productions are associated with certain uncertainties. Obviously, the most important uncertainty is the projected flows in the rivers at the potential hydropower plant locations. This is handled by considering a broad range of climate projections. Another important source of uncertainty is the actual configuration of the plant itself with factors as maximum turbine flow and generating efficiencies. Finally, operations and maintenance of the actual plant once constructed are as usual an important uncertainty factor in terms of hydropower production.

## 11.2 Recommendations

The study reveals that the combination of SPHY and WEAP can be a powerful tool to assess potential impact of climate change on hydropower generation and a key conclusion is that with the next 50 years the hydropower potential is likely to increase as a result of climate change. This is the result of the specific hydrological characteristics of the Tama Koshi basin, however it is likely that regionally the response is similar. Differences between basins will primarily be caused by differences in the extent of glaciers and the hypsometry of the basin. It would be recommendable to do a similar assessment with these tools for Nepal as a whole or even for a larger region.

In term of specific recommendations, the results could be further improved and detailed if (i) results of higher resolution RCMs would be used as a basis for the downscaling, (ii) more hydro-meteorological observations are made in particular in the higher parts of the catchment, (iii) RCP2.6 and 6.5 could also be included to get a more comprehensive overview of potential climate change impacts, (iv) improvement were made to the routing scheme such that peak flow simulations are improved and (v) to include and assess the impact of operational rules of those plants that run of a reservoir.

This study has tackled the problem from a hydrological perspective, however it would be interesting to collaborate with economists and social sciences to take this a step further and assess the potential economic revenues versus the potential adverse effects of dam construction. Such a cost-benefit analysis could lead to detailed recommendations on where to plan which size of power plant while maximizing economic revenue and minimizing any negative environmental or social impacts.



# 12 References


Armstrong, R. L. (2010), *The Glaciers of the Hindu Kush-Himalayan Region: A summary of the science regarding glacier melt/ retreat in the Himalayan, Hindu Kush, Karakoram, Pamir, and Tien Shan mountain ranges*, Kathmandu.

Arora, V. K., J. F. Scinocca, G. J. Boer, J. R. Christian, K. L. Denman, G. M. Flato, V. V Kharin, W. G. Lee, and W. J. Merryfield (2011), Carbon emission limits required to satisfy future representative concentration pathways of greenhouse gases, , *38*, 3–8, doi:10.1029/2010GL046270.

Bajracharya, S. R., S. B. Maharjan, F. Shrestha, O. R. Bajracharya, and S. Baidya (2014), *Glacier status in Nepal and decadal change from 1980 to 2010 based on landsat data*, Kathmandu.

van Beek, L. P. H., and M. F. P. Bierkens (2008), *The Global Hydrological Model PCR-GLOBWB: Conceptualization, Parameterization and Verification*, Utrecht.

Biemans, H., L. H. Speelman, F. Ludwig, E. J. Moors, a J. Wiltshire, P. Kumar, D. Gerten, and P. Kabat (2013), Future water resources for food production in five South Asian river basins and potential for adaptation - A modeling study., *Sci. Total Environ.*, *468–469*, S117–S131, doi:10.1016/j.scitotenv.2013.05.092.

Blázquez, J., and M. N. Nuñez (2013), Analysis of uncertainties in future climate projections for South America: Comparison of WCRP-CMIP3 and WCRP-CMIP5 models, *Clim. Dyn.*, *41*(3–4), 1039–1056, doi:10.1007/s00382-012-1489-7.

Boe, J., L. Terray, F. Habets, and E. Martin (2007), Statistical and dynamical downscaling of the Seine basin climate for hydro-meteorological studies, *Int. J. Climatol.*, *27*, 1643–1655, doi:10.1002/joc.

De Boer, F. (2015), *HiHydroSoil: A high resolution soil map of hydraulic properties*, Wageningen, The Netherlands.

Bontemps, S., P. Defourny, E. van Bogaert, O. Arino, V. Kalogirou, and J. Ramos Perez (2011), *GLOBCOVER 2009. Products Description and Validation Report.*

Bordoy, R., and P. Burlando (2013), Bias correction of regional climate model simulations in a region of complex orography, *J. Appl. Meteorol. Climatol.*, *52*, 82–101, doi:10.1175/JAMC-D-11-0149.1.

Cannon, A. J. (2014), Selecting GCM Scenarios that Span the Range of Changes in a Multimodel Ensemble : Application to CMIP5 Climate Extremes Indices, *J. Clim.*, *28*, 1260–1267, doi:10.1175/JCLI-D-14-00636.1.

Christensen, J. H., and O. B. Christensen (2002), Severe summertime flooding in Europe, *Nature*, *421*(February), 805–806.

Dee, D. P. et al. (2011), The ERA-Interim reanalysis: configuration and performance of the data assimilation system, *Q. J. R. Meteorol. Soc.*, *137*(656), 553–597, doi:10.1002/qj.828.

Deque, M. (2007), Frequency of precipitation and temperature extremes over France in an anthropogenic scenario: Model results and statistical correction according to observed values, *Glob. Planet. Change*, *57*(1–2), 16–26, doi:10.1016/j.gloplacha.2006.11.030.

DOED (2016), Department of Electricity Development, Ministry of Energy, Government of Nepal, Available from: http://www.doed.gov.np/operating_projects_hydro.php (Accessed 29 December 2016)

Droogers, P., R. Butterfield, and J. Dyszynski (2009), *Climate change and hydropower, impact and adaptation costs: case study Kenya*, Wageningen.

Eden, J. M., and M. Widmann (2014), Downscaling of GCM-Simulated Precipitation Using Model Output Statistics, *J. Clim.*, *27*(1), 312–324, doi:10.1175/JCLI-D-13-00063.1.

Eden, J. M., M. Widmann, D. Grawe, and S. Rast (2012), Skill, Correction, and Downscaling of GCM-Simulated Precipitation, *J. Clim.*, *25*(11), 3970–3984, doi:10.1175/JCLI-D-11-00254.1.

Finger, D., G. Heinrich, A. Gobiet, and A. Bauder (2012), Projections of future water resources and their uncertainty in a glacierized catchment in the Swiss Alps and the subsequent effects on hydropower production during the 21st century, *Water Resour. Res.*, *48*(2), 1–20, doi:10.1029/2011WR010733.

Fowler, H. J., S. Blenkinsop, and C. Tebaldi (2007), Linking climate change modelling to impacts studies : recent advances in downscaling techniques for hydrological modelling, *Int. J. Climatol.*, (September), 1547–1578, doi:10.1002/joc.

Frey, H., H. Machguth, M. Huss, C. Huggel, S. Bajracharya, T. Bolch, A. Kulkarni, A. Linsbauer,


N. Salzmann, and M. Stoffel (2014), Estimating the volume of glaciers in the Himalayan-Karakoram region using different methods, *Cryosph.*, *8*(6), 2313–2333, doi:10.5194/tc-8-2313-2014.
Gardelle, J., E. Berthier, Y. Arnaud, and A. Kääb (2013), Region-wide glacier mass balances over the Pamir-Karakoram-Himalaya during 1999–2011, *Cryosph.*, *7*(4), 1263–1286, doi:10.5194/tc-7-1263-2013.
Gurung, D. R., A. V. Kulkarni, A. Giriraj, K. S. Aung, B. Shrestha, and J. Srinivasan (2011), Changes in seasonal snow cover in Hindu Kush-Himalayan region, *Cryosph. Discuss.*, *5*(2), 755–777, doi:10.5194/tcd-5-755-2011.
Hagemann, S., B. Machenhauer, R. Jones, O. B. Christensen, M. Déqué, D. Jacob, and P. L. Vidale (2004), Evaluation of water and energy budgets in regional climate models applied over Europe, *Clim. Dyn.*, *23*(5), 547–567, doi:10.1007/s00382-004-0444-7.
Houle, D., A. Bouffard, L. Duchesne, T. Logan, and R. Harvey (2012), Projections of future soil temperature and water content for three Southern Quebec forested sites, *J. Clim.*, *25*(21), 7690–7701, doi:10.1175/JCLI-D-11-00440.1.
Houska, T., P. Kraft, A. Chamorro-Chavez, and L. Breuer (2015), SPOTting Model Parameters Using a Ready-Made Python Package, edited by D. Hui, *PLoS One*, *10*(12), e0145180, doi:10.1371/journal.pone.0145180.
Immerzeel, W. W., L. P. H. van Beek, and M. F. P. Bierkens (2010), Climate change will affect the Asian water towers., *Science*, *328*(5984), 1382–5, doi:10.1126/science.1183188.
Immerzeel, W. W., F. Pellicciotti, and M. F. P. Bierkens (2013), Rising river flows throughout the twenty-first century in two Himalayan glacierized watersheds, *Nat. Geosci.*, *6*(9), 742–745, doi:10.1038/ngeo1896.
Immerzeel, W. W., N. Wanders, A. F. Lutz, J. M. Shea, and M. F. P. Bierkens (2015), Reconciling high-altitude precipitation in the upper Indus basin with glacier mass balances and runoff, *Hydrol. Earth Syst. Sci.*, *19*(11), 4673–4687, doi:10.5194/hess-19-4673-2015.
IPCC (2007), *Climate change 2007: Synthesis Report. Contribution of Working Groups I, II and III to the Fourth Assessment Report of the Intergovernmental Panel on Climate Change*, edited by R. K. Pachauri and A. Reisinger, Geneva, Switzerland.
IPCC (2013), *Climate Change 2013: The Physical Science Basis. Contribution of Working Group I to the Fifth Assessment Report of the Intergovernmental Panel on Climate Change*, Cambridge, UK.
Jha, R. (2011), Total Run-of-River type Hydropower Potential of Nepal, *Hydro Nepal J. Water, Energy Environ.*, *7*, doi:10.3126/hn.v7i0.4226.
Joetzjer, E., H. Douville, C. Delire, and P. Ciais (2013), Present-day and future Amazonian precipitation in global climate models: CMIP5 versus CMIP3, *Clim. Dyn.*, *41*(11–12), 2921–2936, doi:10.1007/s00382-012-1644-1.
Kääb, A., D. Treichler, C. Nuth, and E. Berthier (2015), Brief Communication: Contending estimates of 2003–2008 glacier mass balance over the Pamir–Karakoram–Himalaya, *Cryosph.*, *9*(2), 557–564, doi:10.5194/tc-9-557-2015.
Karssenberg, D. (2002), The value of environmental modelling languages for building distributed hydrological models, *Hydrol. Process.*, *16*(14), 2751–2766, doi:10.1002/hyp.1068.
Karssenberg, D., P. A. Burrough, R. Sluiter, and K. de Jong (2001), The PCRaster Software and Course Materials for Teaching Numerical Modelling in the Environmental Sciences, *Trans. GIS*, *5*(2), 99–110, doi:10.1111/1467-9671.00070.
Karssenberg, D., O. Schmitz, P. Salamon, K. de Jong, and M. F. P. Bierkens (2010), A software framework for construction of process-based stochastic spatio-temporal models and data assimilation, *Environ. Model. Softw.*, *25*(4), 489–502, doi:10.1016/j.envsoft.2009.10.004.
Kay, A. L., H. N. Davies, V. A. Bell, and R. G. Jones (2008), Comparison of uncertainty sources for climate change impacts: flood frequency in England, *Clim. Change*, *92*, 41–63, doi:10.1007/s10584-008-9471-4.
Khadka, D., M. S. Babel, S. Shrestha, and N. K. Tripathi (2014), Climate change impact on glacier and snow melt and runoff in Tamakoshi basin in the Hindu Kush Himalayan (HKH) region, *J. Hydrol.*, *511*, 49–60, doi:10.1016/j.jhydrol.2014.01.005.
Knutti, R., and J. Sedláček (2012), Robustness and uncertainties in the new CMIP5 climate model projections, *Nat. Clim. Chang.*, *3*, 369–373, doi:10.1038/nclimate1716.
Kotz, S., and S. Nadarajah (2000), *Extreme Value Distributions. Theory and Applications*, Imperial College Press, London.
Leander, R., and T. A. Buishand (2007), Resampling of regional climate model output for the



simulation of extreme river flows, *J. Hydrol.*, *332*, 487–496, doi:10.1016/j.jhydrol.2006.08.006.
Lenderink, G., a. Buishand, and W. van Deursen (2007), Estimates of future discharges of the river Rhine using two scenario methodologies: direct versus delta approach, *Hydrol. Earth Syst. Sci.*, *11*(3), 1145–1159, doi:10.5194/hess-11-1145-2007.
Liang, X., D. P. Lettenmaier, E. F. Wood, and S. J. Burges (1994), A simple hydrologically based model of land surface water and energy fluxes for general circulation models, *J. Geophys. Res.*, *99*(D7), 14415, doi:10.1029/94JD00483.
Liang, X., E. F. Wood, and D. P. Lettenmaier (1996), Surface soil moisture parameterization of the VIC-2L model: Evaluation and modification, *Glob. Planet. Change*, *13*(1–4), 195–206, doi:10.1016/0921-8181(95)00046-1.
Linsbauer, A., H. Frey, W. Haeberli, H. Machguth, M. F. Azam, and S. Allen (2016), Modelling glacier-bed overdeepenings and possible future lakes for the glaciers in the Himalaya—Karakoram region, *Ann. Glaciol.*, *57*(71), 119–130, doi:10.3189/2016AoG71A627.
Lutz, A. F., and W. W. Immerzeel (2013), *Water Availability Analysis for the Upper Indus , Ganges , Brahmaputra , Salween and Mekong River Basins*, Wagenignen.
Lutz, A. F., and W. W. Immerzeel (2015), *HI-AWARE Reference Climate Dataset for the Indus , Ganges and Brahmaputra River Basins. FutureWater report 146*, Wageningen, The Netherlands.
Lutz, A. F., P. Droogers, and W. W. Immerzeel (2012), *Climate Change Impact and Adaptation on the Water Resources in the Amu Darya and Syr Darya River Basins*, Wageningen.
Lutz, A. F., W. W. Immerzeel, A. Gobiet, F. Pellicciotti, and M. F. P. Bierkens (2013), Comparison of climate change signals in CMIP3 and CMIP5 multi-model ensembles and implications for Central Asian glaciers, *Hydrol. Earth Syst. Sci.*, *17*(9), 3661–3677, doi:10.5194/hess-17-3661-2013.
Lutz, A. F., W. W. Immerzeel, A. B. Shrestha, and M. F. P. Bierkens (2014a), Consistent increase in High Asia's runoff due to increasing glacier melt and precipitation, *Nat. Clim. Chang.*, *4*(7), 587–592, doi:10.1038/nclimate2237.
Lutz, A. F., W. W. Immerzeel, A. B. Shrestha, and M. F. P. Bierkens (2014b), Consistent increase in High Asia's runoff due to increasing glacier melt and precipitation, *Nat. Clim. Chang.*, *4*, 587–592, doi:10.1038/NCLIMATE2237.
Lutz, A. F., W. W. Immerzeel, P. D. A. Kraaijenbrink, and A. B. Shrestha (2016a), Climate Change Impacts on the Upper Indus Hydrology: Sources, Shifts and Extremes, *PLoS One*, *11*(11), e0165630, doi:10.1371/journal.pone.0165630.
Lutz, A. F., H. W. ter Maat, H. Biemans, A. B. Shrestha, P. Wester, and W. W. Immerzeel (2016b), Selecting representative climate models for climate change impact studies: an advanced envelope-based selection approach, *Int. J. Climatol.*, *36*, 3988–4005.
Maraun, D. et al. (2010), Precipitation downscaling under climate change: recent developments to bridge the gap between dynamical models and the end user, *Rev. Geophys.*, *48*(RG3003), 1–34.
Maskey, S., S. Uhlenbrook, and S. Ojha (2011), An analysis of snow cover changes in the Himalayan region using MODIS snow products and in-situ temperature data, *Clim. Change*, *108*(1–2), 391–400, doi:10.1007/s10584-011-0181-y.
Maussion, F., D. Scherer, T. Mölg, E. Collier, J. Curio, and R. Finkelnburg (2014), Precipitation Seasonality and Variability over the Tibetan Plateau as Resolved by the High Asia Reanalysis, *J. Clim.*, *27*(5), 1910–1927, doi:10.1175/JCLI-D-13-00282.1.
Meehl, G. A., C. Covey, K. E. Taylor, T. Delworth, R. J. Stouffer, M. Latif, B. McAvaney, and J. F. B. Mitchell (2007), THE WCRP CMIP3 Multimodel Dataset: A New Era in Climate Change Research, *Bull. Am. Meteorol. Soc.*, *88*(9), 1383–1394, doi:10.1175/BAMS-88-9-1383.
Minville, M., F. Brissette, and R. Leconte (2008), Uncertainty of the impact of climate change on the hydrology of a nordic watershed, *J. Hydrol.*, *358*(1–2), 70–83, doi:10.1016/j.jhydrol.2008.05.033.
Moss, R. H. et al. (2010), The next generation of scenarios for climate change research and assessment., *Nature*, *463*(7282), 747–56, doi:10.1038/nature08823.
Nash, J. E., and J. V. Sutcliffe (1970), River flow forecasting through conceptual models part I — A discussion of principles, *J. Hydrol.*, *10*(3), 282–290, doi:10.1016/0022-1694(70)90255-6.
NEA (2015), *Annual Report of Nepal Electricity Authority, Released on 2015*, Kathmandu.
van Pelt, S. C., J. J. Beersma, T. A. Buishand, B. J. J. M. van den Hurk, and P. Kabat (2012),

Future changes in extreme precipitation in the Rhine basin based on global and regional climate model simulations, *Hydrol. Earth Syst. Sci.*, *16*(12), 4517–4530, doi:10.5194/hess-16-4517-2012.
Peterson, T. C. (2005), Climate change indices, *WMO Bull.*, *54*(2), 83–86.
Pfeffer, W. et al. (2014), The Randolph Glacier Inventory: a globally complete inventory of glaciers, *J. Glaciol.*, *60*(221), 537–552, doi:10.3189/2014JoG13J176.
Piani, C., G. P. Weedon, M. Best, S. M. Gomes, P. Viterbo, S. Hagemann, and J. O. Haerter (2010), Statistical bias correction of global simulated daily precipitation and temperature for the application of hydrological models, *J. Hydrol.*, *395*(3–4), 199–215, doi:10.1016/j.jhydrol.2010.10.024.
Pierce, D. W., T. P. Barnett, B. D. Santer, and P. J. Gleckler (2009), Selecting global climate models for regional climate change studies., *Proc. Natl. Acad. Sci. U. S. A.*, *106*(21), 8441–8446, doi:10.1073/pnas.0900094106.
Prudhomme, C., N. Reynard, and S. Crooks (2002), Downscaling of global climate models for flood frequency analysis: where are we now?, *Hydrol. Process.*, *16*(6), 1137–1150, doi:10.1002/hyp.1054.
Rosenberg, J., S. J. Davis, U. Narloch, and S. Hallegatte (2015), Climate constraints on the carbon intensity of economic growth, *Environ. Res. Lett.*, *10*(9), 95006, doi:10.1088/1748-9326/10/9/095006.
Sahukhal, R., and T. R. Bajracharya (2015), Integration of Climate Change Impact Parameters in Hydropower Planning in Nepal: A Case Study of Kaligandaki Gorge HP, in *In Proceedings of IOE Graduate Conference*, pp. 211–2017.
Shrestha, S., A. R. Bajracharya, and M. S. Babel (2016), Assessment of risks due to climate change for the Upper Tamakoshi Hydropower Project in Nepal, *Clim. Risk Manag.*, *14*, 27–41, doi:10.1016/j.crm.2016.08.002.
Sieber, J., and D. Yates (2015), *WEAP User Guide*, Stockholm.
Sorg, A., M. Huss, M. Rohrer, and M. Stoffel (2014), The days of plenty might soon be over in glacierized Central Asian catchments, *Environ. Res. Lett.*, *9*(104018), 8, doi:10.1088/1748-9326/9/10/104018.
Sperber, K. R., H. Annamalai, I. S. Kang, A. Kitoh, A. Moise, A. Turner, B. Wang, and T. Zhou (2013), The Asian summer monsoon: An intercomparison of CMIP5 vs. CMIP3 simulations of the late 20th century, *Clim. Dyn.*, *41*(9–10), 2711–2744, doi:10.1007/s00382-012-1607-6.
Taylor, K. E., R. J. Stouffer, and G. A. Meehl (2012), An Overview of CMIP5 and the Experiment Design, *Bull. Am. Meteorol. Soc.*, *93*(4), 485–498, doi:10.1175/BAMS-D-11-00094.1.
Terink, W., R. T. W. L. Hurkmans, P. J. J. F. Torfs, and R. Uijlenhoet (2010), Evaluation of a bias correction method applied to downscaled precipitation and temperature reanalysis data for the Rhine basin, *Hydrol. Earth Syst. Sci.*, *14*(4), 687–703, doi:10.5194/hess-14-687-2010.
Terink, W., A. F. Lutz, G. W. H. Simons, W. W. Immerzeel, and P. Droogers (2015), SPHY v2.0: Spatial Processes in HYdrology, *Geosci. Model Dev.*, *8*(7), 2009–2034, doi:10.5194/gmd-8-2009-2015.
Themeßl, M. J., A. Gobiet, and A. Leuprecht (2011a), Empirical-statistical downscaling and error correction of daily precipitation from regional climate models, *Int. J. Climatol.*, *31*(10), 1530–1544, doi:10.1002/joc.2168.
Themeßl, M. J., A. Gobiet, and G. Heinrich (2011b), Empirical-statistical downscaling and error correction of regional climate models and its impact on the climate change signal, *Clim. Change*, *112*(2), 449–468, doi:10.1007/s10584-011-0224-4.
van Vuuren, D. P. et al. (2011), The representative concentration pathways: an overview, *Clim. Change*, *109*(1–2), 5–31, doi:10.1007/s10584-011-0148-z.
Warszawski, L., K. Frieler, V. Huber, F. Piontek, O. Serdeczny, and J. Schewe (2014), The Inter-Sectoral Impact Model Intercomparison Project (ISI-MIP): project framework., *Proc. Natl. Acad. Sci. U. S. A.*, *111*(9), 3228–32, doi:10.1073/pnas.1312330110.
WECS (2011), *Water Resources of Nepal in the Context of Climate Change*, Kathmandu.
Widmann, M., and C. S. Bretherton (2003), Statistical Precipitation Downscaling over the Northwestern United States Using Numerically Simulated Precipitation as a Predictor, *J. Clim.*, *16*, 799–816.
Wilby, R. L., and T. M. L. Wigley (1997), Downscaling general circulation model output: a review of methods and limitations, *Prog. Phys. Geogr.*, *21*(4), 530–548, doi:10.1177/030913339702100403.



Wilcke, R., and L. Bärring (2016), Selecting regional climate scenario for impact modelling studies, *Environ. Model. Softw.*, *78*, 191–201, doi:10.1016/j.envsoft.2016.01.002.